NONDESTRUCTIVE EVALUATION
OF A HIGH TEMPERATURE
CERAMIC MATRIX COMPOSITE MATERIAL

by

Barbara Dawn Trandel

Thesis submitted to the Faculty of the

Virginia Polytechnic Institute and State University

in partial fulfillment of the requirements for the degree of

Master of Science

in

Engineering Science and Mechanics

APPROVED:

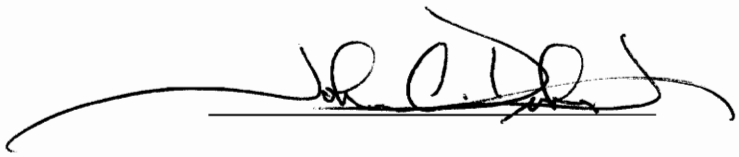

John C. Duke, Jr., Chairman

D. P. H. Hasselman

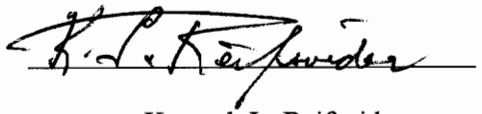

Kenneth L. Reifsnider

February 8, 1995

Blacksburg, Virginia

NONDESTRUCTIVE EVALUATION

OF A HIGH TEMPERATURE

CERAMIC MATRIX COMPOSITE MATERIAL

by
B. Dawn Trandel
John C. Duke, Jr., Chairman
Engineering Science and Mechanics

(ABSTRACT)

The purpose of this investigation was to nondestructively characterize a 2-D Nicalon-reinforced, CVI-SiC matrix composite before and after exposure to 1000, 1200, and 1400 °C in oxidizing atmospheres of air. Concurrently, the nondestructive testing methods used to detect thermally induced changes in the SiC/SiC composite were evaluated.

All of the NDT techniques, except film X-ray radiography, were sensitive to changes in the ceramic matrix composite (CMC) caused by thermal ageing. Surface and sub-surface scanning acoustic microscope (SAM) micrographs indicated that the CMC specimens were experiencing surface changes. The increase in surface reflectivity of the specimens after heat treatment was attributed to density and elastic property changes related to oxidation of the matrix, formation of silica on the fibers, and increased crystallinity of the Nicalon fibers. Acousto-ultrasonic results indicated that thermal exposure altered the ability of the CMC specimens to transmit ultrasonic energy. The ability to transmit energy was degraded or enhanced depending on ageing temperature and the presence or absence of a refractory coating. C-scans indicated that the heat-treated specimens attenuated/scattered more energy than the as-fabricated specimens. Through-transmission scans indicated that, after thermal exposure, the specimens that had received a refractory coating showed a greater increase in attenuation than the uncoated specimens.

Tensile tests performed at room temperature provided strength data and a means for monitoring acoustic emission. Optical micrographs showed void and silica formation around fibers and the development of microcracks within the matrix. Electron microprobe analysis verified that carbon and silicon were being lost and oxygen was being gained within the fiber-matrix interphase.

ABSTRACT

ACKNOWLEDGEMENTS

The author would like to thank the following people for their help and guidance throughout the course of this research project:

- Dr. John C. Duke, Jr. for providing me with the opportunity to work on this project, and for offering guidance and technical assistance during my graduate career.
- Dr. John C. Duke, Jr., Dr. D. P. H. Hasselman, and Dr. Kenneth L. Reifsnider for graciously serving on my advisory committee.
- Dr. Thomas Dunyak and NASA Lewis for providing financial support for this project.
- Michael Horne and Elahi Mehran for their technical assistance.
- Mac McCord for operating the scanning acoustic microscope and assisting me with the SAM investigation of CMC specimens.
- Miguel Sisson for helping me setup and perform acoustic emission monitoring of CMC specimens.
- Todd Solberg for operating the electron microprobe and assisting me with the EM analysis of CMC specimens.
- My parents and my sister for their love, support, and encouragement throughout my academic career.

TABLE OF CONTENTS

LIST OF FIGURES

LIST OF TABLES

1. INTRODUCTION

A new generation of materials known as ceramic matrix composites (CMC's) has emerged to meet the demands of advancing technologies. Traditional engineering materials, particularly steel, aluminum, and other metal alloys do not possess the high strength-to-weight ratios, oxidation resistance, or high-temperature stability that are needed for new engineering applications. Superconductors for high-speed signal transmission; high-efficiency, low-emission automotive heat engines; and hypersonic aerospace propulsion systems are examples of technologies which have outgrown current engineering materials, including superalloys. Ceramic matrix composites have the potential to meet the demands of these developing technologies. However, the success of these emerging composite systems is contingent on improved raw materials, processing, and quality control. A more thorough understanding of the physical properties, damage mechanisms, and life-cycle of CMC's is also necessary for the general acceptance of these advanced structural materials.

As technology continues to drive the development of ceramic matrix composities, standardization of these new material systems is becoming a national and an international concern. New standards for evaluating the properties and behavior of advanced composite materials are being prepared by US organizations such as ASTM (in conjunction with SACMA), DOD, NASA, ANSI, ASNT, SAE, etc. [1]. Concurrently, several international initiatives associated with the measurement and testing of advanced materials are being organized. The report entitled *A Vision for the Future: Standards Needs for Emerging Technologies*, prepared by the International Organization for Standardization (ISO), the European Community's launching of the European Organization for Testing and Certification (EOTC), and the Versailles Agreement on Advanced Materials and Standards: Proposal for Multilateral Collaborative Research (VAMAS) attest to the emphasis

which is being placed on developing standards for advanced materials [2].

This global interest in the standardization of advanced materials is acting as an impetus for the growth and development of nondestructive testing (NDT) technology. New and improved nondestructive testing equipment and techniques are being developed to assess advanced engineering materials such as CMC's. New methods, such as analytical ultrasonics, computed tomography, and environmental scanning electron microscopy are emerging to meet some of the challenges presented by composite material systems. Concurrently, new standards for the nondestructive (and destructive) testing of advanced composite systems are being established; however, the standardization of CMC's is progressing slowly. The variety of compatible matrix and reinforcement materials, the variations in raw materials and fabrication methods, and the complex behavior of composite systems are complicating this standardization process.

Numerous difficulties arise when NDT methods are used to characterize ceramic matrix composites. First, NDT methods cannot reliably detect the presence of residual stresses or identify phase composition differences. In addition, at the sub-surface level, NDT methods cannot reliably determine the degree of matrix densification, the fiber distribution, or the character of the fiber/matrix interphase. The inhomogeneous, anisotropic nature of most CMC's challenge even the most sophisticated NDT techniques, yielding NDT results which are difficult to intrepret.

The frequent need for nondestructive evaluation of CMC's at elevated temperatures (> 800° C) further complicates this already difficult area of research. Most nondestructive evaluation (NDE) equipment is not capable of operating at temperatures much beyond room temperature (RT). Contact transducers for performing acoustic-emission and acousto-ultrasound tests at temperatures

beyond 600° C are not commercially available. The need for high-temperature, contact transducers may be eliminated by using waveguides to transmit ultrasonic signals from a furnace-enclosed specimen to an external transducer. However, effectively coupling the specimen-waveguide system so that signal transmission is not compromised by thermal expansion differences or impedance mismatch also poses a difficult task. Thermographic techniques which rely on subtle temperature changes within a mechanically-cycled specimen are also ineffectual at high temperatures. The subtle, mechanically-induced temperature changes are overwhelmed by the severe environmental temperatures. Other problems encountered with nondestructive testing at extreme temperatures include generation of noise by thermal expansion and contraction of furnaces, accelerated oxidation and mechanical degradation of probes/transducers, and the high costs associated with state-of-the-art, high-temperature NDT equipment.

Both nondestructive and destructive tests are needed to characterize the chemical, mechanical, and thermal properties of CMC's. Nondestructive tests provide information about the condition of CMC's in their as-fabricated form. They provide a reference state against which the results of destructive and later nondestructive tests may be compared. Destructive tests are necessary to quantitatively determine chemical, mechanical, and thermal properties. The results from destructive tests are also used to validate the results and conclusions obtained from nondestructive tests.

The purpose of this investigation was to nondestructively characterize a high temperature CMC before and after thermal exposure at 1000, 1200, and 1400 °C. Concurrently, the specific NDT methods used to detect and track damage, or undesirable changes in material properties, were evaluated. NDT methods including acoustic microscopy, acousto-ultrasonics, immersion scan (C-

scan) ultrasonics, film X-ray radiography, optical microscopy, and scanning electron microscopy were used to monitor damage accumulation. The electron microprobe was used to characterize stability; tensile tests performed at RT provided strength data and a means for monitoring acoustic emission.

The current state-of-development of high-temperature CMC's is reviewed. Common matrix and reinforcement materials, fiber architecture, and fabrication techniques associated with high-temperature ceramic composites are included in this review. Improvements in nondestructive and destructive test equipment and techniques are discussed and summarized. This overview will provide background information necessary for the discussion of NDT results and conclusions, and the suggestions for future work.

A continuous fiber-reinforced ceramic composite (CFCC) was the material chosen for this investigation. The material was manufactured by Amercom (an Atlantic Research Corporation company, Chatsworth, CA) using a chemical vapor infiltration process which deposited a silicon carbide (SiC) matrix within a regular eight harness satin weave (8 HSW) reinforcement. The SiC fibers were Nicalon™ fibers manufactured by Nippon Carbon Company of Japan. The fibers were coated with pyrolytic carbon to improve the fiber-matrix interfacial properties of the ceramic matrix composite.

2. LITERATURE REVIEW

Advanced structural materials which can withstand temperatures in excess of 1000°C for prolonged exposures are needed for engineering programs of the 21st Century. The applications for such high-temperature structural materials are numerous, with applications to energy-conversion systems, nuclear containment, chemical processing, and aerospace vehicles being among the most promising. In past years, superalloys, metal matrix composites, and carbon/carbon composites have dominated high-temperature materials research and development programs. However, problems with these materials and improvements in ceramic fiber technology have redirected attention to ceramic matrix composites.

Much of the literature pertaining to CMC's for high-temperature structural applications is related to government-sponsored research and is proprietary in nature; the literature which is available provides general information about the chemistry, fabrication, and processing techniques of fibers, matrices, and final CMC's. The following literature review is divided into four sections: (1) high-temperature ceramic matrix composites, (2) nondestructive testing of high-temperature CMC's, (3) additional techniques for characterizing CMC's, and (4) new equipment for high-temperature, destructive testing of CMC's. The first section includes an overview of high-temperature CMC's and information on the fiber, fiber architecture, fabrication process, and fiber-matrix system pertinent to this investigation. The NDT section is subdivided into the four main NDT methods used in this investigation: acoustic microscopy, acousto-ultrasonics, film X-ray radiography, and immersion scan ultrasonics. Additional testing methods used in this investigation are discussed in the third section; they include optical microscopy, electron microprobe analysis with SEM, and acoustic emission monitoring. Finally, because nondestructive and destructive testing are

complementary methods for materials characterization, new developments in destructive testing are briefly reviewed in the last section.

2-1. High-Temperature Ceramic Matrix Composites

As defined by R. M. Jones [3], a composite consists of two or more materials combined on a macroscopic level - a matrix material and a reinforcement material. Composites consisting of two or more matrix materials or reinforcements are known as hybrid composites. A composite exhibits the best (and worst) physical properties of each of its constituent materials, in addition to properties unique to itself. This is because its constituent materials are combined on a macroscopic level, as opposed to a microscopic level. Accordingly, composites may be tailored to exhibit chemical, thermal, and mechanical characteristics that are defined by a desired final product.

Ceramic matrix composites offer higher strength, improved fracture toughness, and better thermal stability than do their monolithic counterparts. A ceramic matrix composite refers to a composite system in which the matrix is a glass, glass-ceramic, polycrystalline-ceramic, carbide, nitride, boride, or oxide. The reinforcements used in a ceramic matrix are generally made of metal or ceramic, and take many shapes and sizes. High-temperature structural applications generally require continuous-fiber, chopped-fiber, or whisker reinforcements made of ceramic. **Table 1** provides a list of the matrix materials and fibers most commonly cited in the literature with reference to high temperature applications [4, 5, 6, 7]; carbon and graphite materials are not included in this list.

TABLE 1: Matrix and fiber materials for high-temperature applications.

Matrix Materials:	Fibers:
Non-Oxides	Non-Oxides
Silicon Carbide (SiC)	HPZ (Dow Corning Corporation)
Silicon Nitride (Si_3N_4)	precursor: *h*ydrido*p*olysila*z*ane
Titanium diboride (TiB_2)	MPDZ (DARPA)
	precursor: *m*ethyl*p*oly*d*isila*z*ane
Oxides	MPS (DARPA)
Alumina (Al_2O_3)	precursor: *m*ethyl*p*oly*s*ilane
Zirconia (ZrO_2)	Nicalon (Nippon Carbon Co., Ltd., Japan)
	precursor: polycarbosilane
Glass-Ceramics	SCS-6 (Avco Specialty Materials/Textron)
Barium aluminosilicate, BAS	produced by CVD; monofilament
Barium magnesium aluminosilicate, BMAS	Sigma (Berghof, Tubingen, FRG)
Barium osumilite	TNSN (Toa Nenvvo Kogyo K.K., Japan)
Calcium aluminosilicate, CAS (I and II)	Tyranno (Ube Industries Ltd., Japan)
Lithium aluminosilicate, LAS (I and II)	precursor: polytitanocarbosilane
	VLS (Los Alamos National Laboratory)
Glasses	SiC whisker
Alkali borosilicate, ABS	
Alkaline earth aluminosilicate, AEAS	Oxide
Borosilicate	Nextel 312, 440, 480 (3M Company)
	produced by sol-gel method
	Sumitomo

Extensive testing has been performed on many of these matrix materials, fibers, and matrix-fiber systems to characterize them in ambient conditions. However, few investigations have been performed to determine how they will perform at elevated temperatures. Detailed information about CMC's is provided in several recently published books: *Fiber and Whisker Reinforced Ceramics for Structural Applications* by David Belitskus (1993)[4], *Fiber Reinforced Ceramic Composites* by K. S. Mazidiyasni (1990)[8], and *Advanced Fibers and Composites* by Francis S. Galasso (1989)[9]. A literature review of CMC's written by L. J. Schioler *et al* [7], and an article prepared by Frances I. Hurwitz [5] offer overviews of the state of development of CMC's and their matrix and fiber constituents.

As previously stated, investigations pertaining to the high-temperature performance of CMC's are scarce. The problems associated with such investigations are aptly summarized by A. W. Searcy's three laws of high-temperature chemistry [10]: (1) everything reacts with everything at high temperatures, (2) everything reacts faster at high temperatures, and (3) the products may be anything. Hillig [10] examines several of the characteristics which may be used to rank or select high-temperature structural materials: melting temperature, stability with respect to volatilization, internal chemical reactivity, and temperature dependence of mechanical properties. Wiedemeier and Singh [11] assess the high-temperature stability of group IV, V, and VI transition metal borides, carbides, nitrides, and oxides using the results of computational thermodynamic analysis. A report by Mah *et al* [12] provides a review of technical issues, such as ceramic fiber development and mechanical and oxidative behavior, facing high-temperature applications of ceramic composites.

Nicalon Fibers

Nicalon fibers, which are the focus of this investigation, are among the oldest and consequently most rigorously tested fibers listed in **Table 1**. Clark *et al* [13] have evaluated the performance of standard (NLP 101) and ceramic grade (NLM 202) Nicalon fibers in oxidizing (wet air) and non-oxidizing (argon) atmospheres at 1000, 1200, and 1400 °C. Both fiber types gained weight after being heat-treated in wet air; this weight gain was attributed to surface oxidation and the formation of a silica film on the surface of the fibers. Elemental analyses confirmed that the fibers were gaining oxygen and losing carbon as the stoichiometry of the fibers approached a balance of silicon and carbon. When heat-treated in argon, both fiber types lost weight; the ceramic grade lost 13% while the standard grade lost 33%. After exposure to 1000 °C in an oxidizing atmosphere, the ceramic grade fibers maintained twice the tensile strength of the standard grade fibers, ≈1725 MPa

versus ≈863 MPa. At higher temperatures, the difference in tensile strengths between the two fiber types was much less, although the ceramic-grade-fiber strength remained slightly higher. The tensile strengths of the two fiber grades after argon heat treatments were generally higher then the strengths after wet-air heat treatments. Based on tensile strength, elastic modulus, structural analysis (SEM and X-ray diffraction), and elemental analysis, ceramic grade Nicalon proved to be more stable at high temperatures in both oxidizing and non-oxidizing atmospheres.

Pysher *et al* [14] have measured the tensile strength and Young's modulus of ceramic grade Nicalon fibers as well as Tyranno, Fiber FP, PRD-166, and Nextel 480 at RT, 800, 1000, 1100, 1200, 1300, and 1400 °C. (Fiber FP and PRD-166 are no longer being manufactured.) The SiC-based fibers, Nicalon and Tyranno, proved to be stronger than the oxide fibers at RT and elevated temperatures; they were stronger despite their tendency to oxidize and form voids. Nicalon fibers maintained nearly constant strength between RT and 800 °C; they maintained ≈ 70% of their original strength from 1000 to 1200 °C; at 1300 and 1400 °C, large voids formed on the fibers' surface and the strength dropped drastically. Unlike the oxide fibers, Nicalon and Tyranno were found to be thermodynamically unstable because of the presence of free carbon and silicon.

Kim and Moorhead [15] have investigated the microstructure and mechanical properties of Nicalon fibers exposed to elevated temperatures in reducing and oxidizing atmospheres. The Nicalon fibers were subjected to the following environmental exposures: (1) H_2 with various partial pressures of H_2O for 10 hours at 1000 °C and 1200 °C, and (2) air for 2-100 hours at 800, 1000, 1200, 1400 °C. All of the fibers that were heat treated in air showed a rapid decrease in tensile strength during the first five hours. Between 5 and 100 hours, these same fibers exposed at 800, 1000, and 1200 °C experienced an initial period of strength recovery followed by a gradual

strength loss. Fibers exposed at 1000 °C experienced the greatest recovery, while those exposed at 1400 °C were very fragile and were not tested. They found that for short oxidation periods in air, a thin layer of silica (SiO_2) formed on the fibers and protected the fibers from degradation and rapid loss of strength and toughness. However, the thick layer of silica which formed during long oxidation periods made the fibers brittle. Fiber brittleness was also attributed to an increase in the average grain size of the fibers which accompanied thermal exposure.

Huger *et al* [16] have performed a thermogravimetric analysis of Nicalon (NLM 202) fibers after 100 hours of ageing in air at atmospheric pressure and 700, 800, 900, 1000, 1100, and 1200 °C. Between 250-500 °C, approximately 1-3% of the mass of the Nicalon fibers was lost as the fiber sizing (polyvinyl acetate) was pyrolyzed. Because the mechanisms of oxidation, and not pyrolysis, were of interest, the mass of the fibers at 600 °C was used as the mass reference. After thermal ageing, all of the fibers experienced a mass gain; this was attributed to the passive oxidation of SiC in the fiber and resulting formation of a silica ring (≈ 0.1 μm thick) around the fibers. Logarithmic plots of $\Delta m/m_o$ vs. time indicated that the oxidation kinetics for ageing above 900 °C or for periods longer than 10 hours were diffusion controlled.

Singh and Singh [17] have compared the strength distribution of as-fabricated Nicalon fibers with the strength distribution of Nicalon fibers in a CVI silicon carbide matrix composite, before and after the composite was exposed to 1300 °C for 15 minutes. Using the fiber bundle test and a standard gage length of 10 mm, they found that as-fabricated Nicalon fibers had an average Weibull modulus of 7.1 and a scale parameter of 3.45 GPa. The strength parameters for fibers incorporated in the as-fabricated and heat-treated composites were determined from the mirror radii (mirror is the smooth region where a crack initiates) on the surface of fractured fibers. The

Weibull modulus and scale parameter of a Nicalon fiber in an as-fabricated composite were 6.0 and 1.31 GPa, respectively; in a heat-treated composite these values were 7.8 and 1.24 GPa, respectively. Fibers in the as-fabricated composite experienced a 62% decrease in average strength, while fibers in the heat-treated composite experienced a 64% decrease. The Weibull modulus of the fibers remained approximately constant.

Fiber Architecture

Advanced fibers are one of several reinforcement geometries that are used to toughen ceramic matrix composites. The hierachy of these reinforcements, based on size and complexity, is as follows: (1) particles, (2) short fibers (whiskers) → continuous fibers, (3) flakes → sheets, (4) woven fiber mats (2-D architecture) → continuous fiber weaves (3-D architecture) [18]. According to the theoretical predictions of K. T. Faber [19], the fracture toughness of a ceramic composite depends on the shape of the reinforcement. The relative rankings of particulate reinforcements according to their ability to improve fracture toughness are rods > discs > spheres. Belitskus states that fracture toughness also depends on the size of the reinforcement, noting that toughness increases with rod aspect ratio (length/diameter). Thus, continuous-fiber reinforcements are more effective toughening agents than short fibers or whiskers [5]. Continuous fibers employ several mechanisms for toughening a matrix including matrix microcracking, fiber-matrix debonding, crack bridging, fiber pull-out, and crack deflection. Even greater toughness can be achieved with woven reinforcements in the form of 2-D woven laminate composites or 3-D braided composites; however, these styles of reinforcement pose problems for matrix densification.

Fiber architecture has become a popular subject for investigation as new strides have been made in the production of high-performance, continuous fibers and the fabrication of composite materials.

Unidirectional and bidirectional reinforcements; 2-D woven fabric reinforcements, particularly plain weave (PW), and five and eight harness satin weaves (5HSW and 8HSW); and 3-D braided reinforcements are the main fiber structures being investigated for use in advanced structural ceramics. However, according to Crawford [20], ceramic fabric is often made in satin weaves because satin weaves have more "drape" then plain weaves and are easier to form into complex shapes. In addition to the advantages and disadvantages of particular fabric designs, Crawford's article also contains detailed information about the weaving process. Additional information also can be found in The *Handbook of Composite Reinforcements* [21] which summarizes the current status of ceramic fibers and fiber architecture.

K. W. Buesking [22] and J. M. Neumeister *et al* [23] have studied the effects of weave geometry on the properties and performance of Nicalon/SiC and C/C composites, respectively. According to Buesking's theoretical model, Nicalon/SiC are predicted to be insensitive to fiber geometry. Buesking offers two reasons to support this prediction: (1) the properties of the fibers and matrix are almost identical, and (2) Nicalon fibers are isotropic. Contrary to Buesking's prediction, Neumeister's experimental results from tests performed on C/C composites suggest that weaving can improve the performance of a composite by reducing the composite's flaw sensitivity. The composite's ability to resist flaws appears to improve despite problems associated with fiber waviness and poor fiber alignment, characteristics that are intrinsic to weaves.

Researchers at Amercom, Inc. and the University of California [24] have found that fiber architecture both directly and indirectly affects the properties of advanced composites. Their work with CVI 2-D plain weave $[0/30/60/90]_{2S}$ and 3-D braided Nicalon/SiC composites has shown that fiber architecture influences how efficiently matrix material is distributed thoughout a preform

structure. The 2-D composite investigated had a density of 2.3 g/cm^3, a fiber-volume fraction of 35%, a residual porosity of 15%; the corresponding values for the 3-D composite were 2.6g/cm^3, 32%, and 11%, respectively. Optical micrographs showed that the matrix had uniformly infiltrated the Nicalon fibers in both performs, but had not uniformly infiltrated the preforms themselves. Large voids were found between fabric layers in the 2-D composite and small voids were found at bundle intersections. The tightly spaced, pore network in the 3-D braided composite was found to minimize voids in the matrix, although some large voids were also found at bundle intersections. The average flexural strengths of the as-received 2-D ($\perp$ to fabric layers) and 3-D ($\perp$ to braiding direction) composites were 326 MPa and 692MPa, respectively. After being heat-treated at 1200 °C for 100 hours, the strengths of both composite systems dropped by $\approx$50 %. Fracture toughness values followed this same trend; *i.e.*, dropping by $\approx$50 % after the composites were heat-treated. These results combined with examinations of fractured surfaces (optical microscopy and SEM) and crystal-phase analysis (X-ray diffraction) proved that 3-D architecture out-performs 2-D architecture. The results also proved that the failure behavior and toughening mechanisms of composites are influenced by fiber architecture and the degree of matrix densification.

Chemical Vapor Infiltration

Chemical vapor infiltration (CVI) is a method of fabricating a composite by condensing matrix material from a gas phase on to a hot fiber preform [25]. A carrier gas or volatized liquid/solid, driven by a pressure differential, is passed through a fiber preform. Methyltrichlorosilane (CH_3SiCl_3) and hydrogen mixtures are often used as the gaseous reagents for producing a SiC matrix. The matrix material condenses on the fibers from the gas phase as the carrier gas moves through the fibrous preform. When CVI is used to form a SiC matrix, the deposit is usually crystalline β-SiC which has a cubic crystal structure. Typical processing parameters for the

chemical vapor infiltration of a SiC/SiC composite are a 50 cm^3/min. flow rate of CH_3SiCl_3 (gas), a 10:1 mixture of H_2 to CH_3SiCl_3, and a pressure of 0.2 MPa [26].

There are five classifications of CVI which are based on how the preform is heated and the method used to introduce the gaseous reagents into the preform [25]: (1) isothermal - uniformly heated preform and diffusion-controlled flow of reagents, (2) thermal gradient - thermal gradient through preform thickness and diffusion controlled flow of reagents from cold to hot side of preform, (3) isothermal forced flow - uniformly heated preform and forced flow of reagents, (4) thermal gradient forced flow - thermal gradient through preform thickness and forced flow of reagents from cold to hot side of preform, and (5) pulsed flow - reagents are cyclically forced into and out of the preform. CVI is an attractive fabrication process for fiber-reinforced ceramic matrix composites because the process uses relatively low stresses and temperatures which reduce damage to fibrous preforms. CVI also produces matrices with refined microstructure and high purity, and a final composite structure with dimensions close to the dimensions of the original preform. These processing advantages yield fiber-reinforced ceramic matrix composites which have very good fracture toughness and potential for near-net-shape manufacturing. An added benefit is that CVI equipment also can be used to apply coatings to fibers to enhance the fibers' toughness and oxidation resistance, and reduce chemical interactions between the fibers and the matrix.

There are also several problems associated with this fabrication process [9]: (1) reactant and product gases etch the fibers, (2) voids form when gaseous products are entrapped in the matrix, (3) the thickness of the matrix deposit varies as the reactant in the carrier gas is depleted, and (4) matrix densification is not uniform because different conditions (fiber density, pressure, temperature, etc.) exist throughout the preform. Some of these problems can be solved by rotating

the preform, changing the flow direction of the carrier gas, stirring the carrier gas, or creating a temperature gradient to direct infiltration.

Stinton *et al* [26] have studied SiC/SiC composites which were fabricated using thermal-gradient forced-flow CVI. Using this fabrication process with layered cloth preforms, the researchers produced composites with maximum densities of 85-90% of theoretical density. However, large voids were present between the fiber tows and appeared to be aligned within the composite. SiC fibers were heat-treated at 1200 °C in H_2-10% HCl to simulate CVI processing conditions; the fibers were then tensile tested to determine the effects of the CVI process. After being heat-treated at 1200 °C for one hour, the strength of the fibers dropped by 58%. Fibers heated-treated for one hour in the same atmosphere at 1100 and 1000 °C showed a strength decrease of 42% and 8.2%, respectively. These results suggest that the properties of CVI SiC/SiC composites may be improved by reducing processing temperatures.

Nicalon/SiC Composite Systems

SiC/SiC composites made with Nicalon fibers have received increased attention in the past decade. Improvements made to the fibers and to composite processing have yielded tougher SiC/SiC CMC's with enhanced mechanical and thermal characteristics. Lamicq *et al* from SEP (Societe Europeenne de Propulsion, Bordeaux, France) have fabricated and tested 2-D CVI Nicalon/SiC (CERASEP™) composites [27]. The investigators determined the mechanical and thermal properties, and studied the fracture behavior of the materials between RT and 2200 °C. They found that the bend strength of SiC/SiC gradually increased between RT and 1300 °C to ≈ 400 MPa and then progressively decreased to below 50 MPa at 2000 °C. The material experienced no loss in bend strength after being exposed to 1100 °C in air for 500 hours and after being cycled

100 times between 100-700 °C. These results indicate good oxidation resistance and thermal fatigue characteristics, respectively. The material also showed good thermal shock characteristics - an approximate 50 MPa decrease in bend strength was reported after the material had been heated to 1200 °C and quenched in water.

In cooperation with SNECMA, SEP has also undertaken investigations of SiC/SiC (CERASEP) and C/SiC (SEPCARBINOX) for use in turbine engines [28]. The two research groups performed a series of cross-investigations to determine how these CMC's would behave in a turbine engine environment. According to Gauthier *et al* from SNECMA, ceramic matrix composites for long-term use in oxidizing atmospheres may be ranked as follows:

(1) SiC/Borosilicate (400-600 °C)
(2) SiC/Glass-Ceramic (up to 1000 °C)
(3) SiC/SiC (1200 °C with coatings)
(4) C/SiC (1500 °C with coatings; short-term exposure)
(5) C/C (up to 2000 °C with coatings; short-term exposure)

After extensive mechanical testing, the researchers established the mechanical properties of 2-D plain weave SiC/SiC and 2-D 5 HSW C/SiC flat-plate coupons. However, they also found that the misalignment of fibers in the complex shapes of engine parts can lead to as much as a 50% decrease in the mechanical properties predicted from the simple coupons. Studies of the oxidation phenomena in SiC/SiC showed that, in non-stressed specimens, oxygen enters the composite at cut ends or around surface fibers and moves along the fibers into the interior of the specimen. This phenomenon is called "pipeline" oxidation. In stressed specimens, oxygen also enters through microcracks in the matrix. The oxygen reacts with the thin carbon coating on the fibers to form CO and CO_2; it also reacts with silicon in the fibers to form SiO_2. Thus, as the carbon coating

evolves into a gas, a thin silica scale takes its place. This change in interfacial chemistry leads to the brittle behavior of oxidized SiC/SiC.

2-2. Nondestructive Testing of High-Temperature CMC's

The inhomogeneous, anisotropic nature of most ceramic matrix composites are challenging NDE techniques. Established NDT methods are being adapted and new methods are being created to investigate these complex material structures. According to Alex Vary of NASA, these changes are part of "analytical NDE" development [29]. As defined by Vary, "analytical NDE refers to an emerging body of technology dedicated to assessing flaw, damage, and degradation states in structural materials". The general classification of NDT methods which are best suited for the investigation of CMC's include the following: visual-optical examination, liquid penetrant inspection, radiography, and ultrasonics [30].

Sheppard has reviewed some of the most recent developments in nondestructive characterization of advanced ceramic materials [31]. In his review, Sheppard briefly describes the numerous projects being undertaken to optimize the life-cycle of CMC's by designing-for-NDE and developing NDE methodology for life-prediction. The review also includes new developments affecting the following NDT techniques: (1) radiography, (2) ultrasonics, (3) acoustic emission, (4) computed tomography, and (5) magnetic resonance imaging. Ellingson *et al* have prepared a similar report on the current status of NDE for structural ceramics [32]. Reports by Marshall [33], McCauley [34], Proulx *et al* [35], and Vary and Klima [36] are among the many other general reviews.

The need to evaluate CMC's at high temperatures in oxidizing atmospheres is placing additional demands on NDE techniques. The ability to monitor changes within a material while the material is exposed to a long-term, high-temperature environment is important to accurately characterizing materials for high-temperature applications. However, equipment limitations make nondestructive evaluation in such environments extremely difficult. Today, most NDE work must be performed at or near RT, after a CMC specimen has been heat treated. However, progress is being made toward increasing this temperature limit [31, 37].

Crostack and Steffens [37] have investigated developments in ultrasonic testing, acoustic emission, optical holography, and eddy current testing as they apply to high-temperature materials. In their report they describe high-temperature piezoelectric transducers which can be used up to ≈550 °C for brief periods of time. They discuss the advantages of non-contact ultrasound generation by lasers which makes it possible to perform long-term ultrasonic testing at elevated temperatures. Crostack and Steffens also emphasize the problems associated with in-situ high-temperature NDE. For example, changes in the acoustical properties of materials at extreme temperatures are not well understood and hinder the interpretation of NDE results. Similarly, noise from the formation of oxides and spalling scale complicate the identification of acoustic events when acoustic emission monitoring is performed at high temperatures [37].

The nondestructive testing techniques used in this investigation to characterize a Nicalon/SiC composite before and after thermal exposure are reviewed in the following sections. Additional supporting techniques are reviewed in the following chapter.

Scanning Acoustic Microscopy

Three kinds of acoustic microscopes exist for performing NDE investigations, these include the following: the scanning electron acoustic microscope (SEAM), the scanning laser acoustic microscope (SLAM), and the scanning acoustic microscope (SAM). Unlike optical microscopes which use light for imaging, acoustic microscopes use ultrasonic waves. According to Andrew Briggs [38], the advantages to using acoustic waves for imaging are twofold. First, materials which are opaque to light such as alloys and ceramics are not opaque to ultrasonic waves; consequently, ultrasonic waves can be used to create surface and subsurface images of these materials. The second advantage is that ultrasonic waves are scattered by elastic property variations within materials. This scattering of waves makes it possible to image voids, inclusions, and other internal defects.

In the past decade, acoustic microscopy has been used to investigate the internal organization and structure of biological and man-made materials. Human bones and teeth, printed circuit boards and semiconductor packaging, and cermets and composites are a few examples of the materials which acoustic microscopy has helped characterize. In this investigation of a 2-D Nicalon/SiC composite, the scanning acoustic microscope was used to image sub-surface features in as-fabricated and heat-treated composite coupons. One of the main reasons for using SAM to study composites is its sensitivity to fiber-matrix interfaces where there is a mismatch of elastic properties [39]. In these regions, acoustic waves (particularly Rayleigh waves) are strongly reflected and provide good contrast within scanning acoustic micrographs.

Several researchers have investigated SAM's application to ceramics and fiber-reinforced ceramic composites. Atalar has studied the scanning acoustic microscope's sensitivity to anisotropic

materials and has proposed a new lens design to enhance this sensitivity [40, 41]. NASA researchers, Vary and Klima, have investigated the ability of SAM to detect flaws in advanced structural ceramics [42]. Several other researchers have employed SAM to characterize ceramics and fiber-reinforced CMC's.

Lawrence *et al* [43] have used SAM to detect cracks in hot-pressed Si_3N_4. They found that the cracks were visible for negative defocus and conditions which optimized interference between incident and reflected Rayleigh waves. They also noted that to image sub-surface cracks, the ultrasonic wavelength used to inspect the ceramic had to be approximately equal to, or a large fraction of, the depth of the crack.

Fatkin *et al* [39] have reported similar findings in their SAM investigation of engineering ceramics and fiber-reinforced ceramic composites. They too found that the greatest contrast in SAM images was obtained in negative defocus, and that cracks were made visible by fringe patterns created by Rayleigh wave interference. Fatkin *et al* also found that SAM could be used to image variations in porosity among different monolithic ceramics, and to calculate fracture toughness (K_{Ic}) more accurately. Fatkin *et al* were able to more accurately calculate fracture toughness by using SAM to measure the lengths of radial cracks created with a Vickers indentor.

In addition to these investigations of monolithic ceramics, Fatkin *et al* [39] have attempted to use SAM to evaluate the condition of interfacial bonds in ceramics reinforced with SiC fibers and whiskers. In SiC fiber-reinforced pyrex (Pysic), they found that discontinuities appearing at fiber-matrix boundaries in SAM images may suggest disbond regions. Their studies of single fiber Pysic specimens also indicated that there may be a correlation between the degree of contrast at the fiber-

matrix interface in SAM images and the interfacial shear strength. Contrary to the researchers expectations, the specimens which exhibited short fiber pull-out lengths in flexural tests, indicative of greater bond strength, had high contrast at the fiber-matrix interface. The specimens with large pull-out lengths had low contrast at the fiber-matrix interface. The researchers attributed their findings to the thermoelastic stresses that develop between pyrex glass and silicon carbide because of thermal expansion differences. They concluded that the stronger interfaces would inhibit stress relief on cooling and, consequently, would create residual strain fields around the fibers.

In a similar SAM investigation of SiC fibers (Textron SCS-6) in reaction bonded Si_3N_4, Sathish *et al* [44] have correlated the clarity of fringe patterns and line scans in acoustic micrographs with interfacial shear strength. Sathish *et al* found that Rayleigh waves were generated on the SiC surface of the fibers. These waves propagated toward the fiber-matrix interface where they were either reflected or transmitted, depending on the impedance mismatch between the fiber and the matrix. If there was good fiber-matrix contact, corresponding to high interfacial shear strength, most of the energy was transmitted into the matrix. Only a small amount of energy ($\approx$10%) was reflected at the interface. This small amount of reflected energy appeared as a low amplitude standing wave and was seen in the SAM image as blurred fringe patterns and line scans. If the fiber-matrix contact was poor and the interfacial shear strength was weak, most of the energy was reflected at the interface. Consequently, the resulting standing wave had a high amplitude, and the fringe patterns and line scans were very pronounced in the SAM image.

In another investigation, Sathish *et al* [45] used SAM to evaluate the elastic properties of a SCS-6 fiber-reinforced titanium matrix at the microstructural level. They found that the contrast in SAM images could be correlated with microstructure and chemical analysis. According to high

resolution electron microscopy and electron diffraction analysis, the SCS-6 fibers consisted of a carbon core (randomly oriented crystals), four layers of SiC, and a carbonaceous coating (radially aligned crystals). In the SAM images, the outer carbon layer was more reflective than the inner carbon core, and the SiC regions were generally more reflective than the carbon regions; however, there were no observable changes in contrast among the four SiC layers.

Acousto-Ultrasonics

Acousto-ultrasonics (AU) is a relatively new NDT technique combining characteristics of both acoustic emission and ultrasonics, hence the name acousto-ultrasonics. This low-frequency (< 30 MHz) ultrasonic technique was initially developed to nondestructively evaluate the strength of laminar boundaries found in fiber/polymer composites [46]; however, its application has since been expanded to ceramic composites. In general, an AU system consists of an excitation source, a detector, and a method for analyzing data. Piezoelectric transducers, electromagnetic acoustic transducers (EMAT's), and lasers are commonly used as sources and detectors; methods of data analysis include analog and digital data acquisition, and spectral analysis [47, 48]. The constraints imposed by the material properties, size, shape, and location of a particular test material govern the choice of source, detector, and data analysis system.

In this study, the porosity of the Nicalon/SiC specimens influenced the choice of dry-coupled transducers for transmitting and receiving ultrasonic energy. As explained by Bhardwaj [49], porous materials such as ceramic matrix composites absorb the liquid couplants which must be used with most contact-transducers. The results obtained by using liquid-coupled transducers are not reproducible because the thickness of the couplant layer between the transducers and the porous material decreases with time. Dry-coupled transducers are an alternative to liquid-coupled

transducers, although the rough textured surfaces of CMC's also pose problems for dry-coupling techniques.

In this investigation, two dry-coupled piezoelectric transducers, one a source and one a detector, were used to ultrasonically test as-fabricated and heat-treated SiC/SiC specimens. The specimens were tested in their as-received form with no surface preparation. The two dry-coupled transducers were placed on the same surface of the specimen. One transducer transmitted ultrasonic energy into the specimen, simulating the stress waves produced by mechanical loading; the other transducer received this energy in the form of surface displacements. As the stress waves propagated through the specimen, structural and material variations altered these waves. The condition of the material between the two transducers was then correlated with the energy that was detected by the receiver.

The purpose of AU is to evaluate material property variations or distributed damage within a test object as a collective whole [47]. More appropriate NDT techniques such as radiography, ultrasonic C-scans, and computed tomography may be used to identify and locate individual flaws. AU is best suited for evaluating the collective condition of a test object because of the way associated stress waves propagate. In an anisotropic material, such as a fiber-reinforced ceramic matrix composite, the modes of wave propagation are not pure [50, 51] . Each wave mode has components which are parallel and perpendicular to the wave normal. These waves are denoted by their dominant component: quasi-longitudinal waves have large parallel components, and quasi-shear waves have large perpendicular components. Accordingly, the ultrasonic signal does not trace a single path through a CMC; instead, the signal follows many paths associated with different modes of stress wave propagation [47]. The resulting surface displacement is a function of these

combined modes of stress wave propagation, representing a collective rather than a local material condition.

Several investigations have been undertaken to characterize structural ceramics and ceramic composites using ultrasonic methods. Green [50] has studied ultrasonic wave propagation in solids, comparing isotropic to anisotropic, and linear-elastic to non-linear elastic materials. Klima and Baaklini [52] have correlated variations in ultrasonic velocity with changes in bulk density, and variations in ultrasonic attenuation with changes in grain size and porosity. The results from their investigation of monolithic silicon nitride and silicon carbide showed that ultrasonic velocity increased with bulk density, and ultrasonic attenuation increased with grain size and porosity. Hemann and Baaklini [53] have reported on a similar investigation of a graphite-epoxy fiber-reinforced composite in which ultrasonic attenuation and wave speed were measured as a function of tensile stress. They found a strong correlation between ultrasonic attenuation and applied stress, and a weak correlation between wave speed and applied stress. They also noted that both attenuation and wave speed were frequency dependent.

The following researchers have done extensive work in ultrasonics and acousto-ultrasonics: M. C. Bhardwaj, George Y. Baaklini, Edward R. Generazio, Harold E. Kautz, and Alex Vary (all except Bhardwaj are affiliated with the NASA Lewis Research Center). Their papers may be referenced for additional information on ultrasonics and AU.

Film X-Ray Radiography

Radiography is an NDT method in which X-rays or gamma rays pass through a test object and onto a film. A 2-D photographic record of the 3-D object, known as a radiograph, is produced.

Variations in the density or thickness of an object or the presence of voids and inclusions appear in the radiograph as different gray levels. Thus, radiography can be used to produce a map of a test object's internal structure.

X-ray radiography is a technique for internally examining an object which is opaque to visible light. Radiation in the form of X-rays ($\lambda = 10^{-7} - 10^{-13}$ μm) interacts with a material; the X-rays which are transmitted and attenuated by the material are recorded on film. The film image is a two-dimensional representation of the internal and external characteristics of the object. Regions of a material which do not attenuate or absorb X-rays appear as black or dark gray regions on the film negative (white or light gray in the developed print). Conversely, regions which attenuate X-rays appear as white or light gray regions on the film negative (black or dark gray in the developed print). X-ray absorption increases with increasing material density, material thickness, and atomic number of a material's elemental constituents. Film X-ray radiography can identify voids, inclusions, and other flaws. However, flaws such as small cracks which run perpendicular to the plane of the film will not appear in the film image.

Although not the sole focus of most composite material investigations, X-ray radiography is commonly used along with other NDE techniques to qualitatively verify results. A thorough discussion of X-ray radiography may be found in *Nondestructive Testing Handbook, Vol. 3: Radiography and Radiation Testing* [54] published by the American Society for Nondestructive Testing. Several researchers have also investigated X-ray radiography's application to ceramics and fiber-reinforced composites. Amin *et al* [55] have investigated the ability of microfocus radiography to detect seeded defects in HIP'ed silicon nitride. Notea *et al* [56] have attempted to correlate film density variations in X-ray radiographs with measured hardness variations in

SYALON. Jamison has addressed some of the issues involved with using radiography to inspect composites and has explained the use of stereo X-ray radiography [57].

Immersion Scan Ultrasonics

Ultrasonic testing of materials is a popular and expanding area in nondestructive testing. Ultrasonic waves can be used to spatially locate and image external and internal defects and quantify material properties in a variety of materials [58]. Ultrasonic waves are high-frequency vibrational waves which propagate within a medium. In general, the frequency range of ultrasonic waves used for NDT is 200 kHz-20 MHz.

There are three main types of ultrasonic waves [58]: (1) longitudinal (compression or pressure) waves - waves which propagate in the direction of particle motion, (2) shear (shear vertical or shear horizontal) waves - waves which propagate perpendicular to the direction of particle motion, and (3) surface (Rayleigh) waves - waves which have an elliptical particle motion perpendicular to the plane of an interacting surface. Among these three wave modes, longitudinal waves are the most commonly used for NDT because they can propagate in solids as well as liquids and gases.

There are several ways in which to generate ultrasonic waves in a test material. In this investigation, ultrasonic waves were generated in the Nicalon/SiC specimens by a piezoelectric transducer. The electronically pulsed transducer applied small, rapid displacements to the surface of the material via the water coupling. These small displacements then propagated to successive interior elements of the material until they reached another exterior surface. At the exterior surface, another piezoelectric transducer converted the received, periodic displacements to electronic pulses which were then analyzed.

In addition to the numerous ways in which to generate ultrasonic waves, there are also numerous pulser-receiver configurations which can be used to characterize different types of materials and investigate complex test-object geometries [58]. The immersion through-transmission technique was used in this investigation because it is one of the preferred methods for investigating highly attenuative materials such as ceramic matrix composites. This technique requires that the test specimen be submerged in water; the pulser is positioned on one side of the specimen while the receiver is placed on the opposite side of the specimen in perfect alignment with the pulser. Using this configuration the ultrasonic waves must make only one trip through the material, as opposed to a round trip for the immersion pulse-echo technique.

Ultrasonic testing involves monitoring designated peak-amplitudes (marked by adjustable time gates) of an induced waveform. The collected data is then displayed in one of the following formats: (1) a line scan in which signal amplitude and temporal position correspond to flaw size and location, respectively (A-scan), (2) a cross-sectional image showing the depth and size of flaws (B-scan), and (3) a planar image showing the X-Y location of flaws (C-scan). More complex analysis procedures may be used to characterize a material by correlating a waveform parameter (from the gated region of the waveform), such as amplitude or arrival-time, with a material property. However, the most complex analysis procedures are associated with quantitative ultrasonic measurements.

Ultrasonic processing systems based on the principles of neural networks are being taught to predict wavefield quantities and source features using auto-associative algorithms [59]. Very complex analytical methods, such as the *semi-inverse methods*, rely on using the solutions for elastodynamic problems to correlate material properties with ultrasonic parameters. The *inverse*

problem is another complex analytical approach which involves recovering material characteristics from ultrasonic waveform data by deconvolving the data.

Despite the problems associated with immersion scan ultrasonics, several investigators have chosen to use the technique to characterize ceramic matrix composites. Walter *et al* [60] have used two immersion through-transmission methods to study porosity levels in a CVI SiC/SiC composite. One method involved laser-generated ultrasound; the other method used a signal averaging technique known as time delay spectrometry. Both techniques were chosen for their potential to improve ultrasonic sensitivity. The resulting ultrasonic maps (C-scans) revealed large variations in porosity within the composite. Correlating these results with X-ray radiographs, Walter *et al* found that regions of low porosity (high density) transmitted more energy and had higher velocities than regions of high porosity (low density). Attenuation spectra also showed that ultrasonic attenuation increased as material porosity increased and as the test frequency was increased.

Mahmoud [61] has investigated the applicability of high frequency ultrasonics (25, 50, and 100 MHz) to flaw detection in isopressed SiC, injection molded SiC, and Si_3N_4. He used the immersion pulse-echo technique with transducer configurations for direct incidence and leaky Rayleigh waves. Mahmoud found that sharper surface images could be obtained using higher testing frequencies. He also found that better resolution could be obtained for a given frequency by using a transducer with a shorter focal length. Mahmoud also concluded that the leaky surface wave method was superior to the direct incidence method for imaging internal defects and that internal imaging could be enhanced by polishing the surface.

2-3. Additional Techniques for Characterizing CMC's

Optical and Scanning Electron Microscopy

Optical and scanning electron microscopy are usually not the focus of composite materials investigations. However, these methods often provide definitive results which make it easier to interpret the less "user-friendly" results generated by NDE techniques. Information on optical techniques may be found in the Proceedings of the SEM Fall Conference on Experimental Mechanics, 1986 entitled *Optical Methods in Composites* [62]. In addition, Bender *et al* [63] and Maniette *et al* [64] have written reports that address the use of electron microscopy for characterizing ceramic matrix composites and ceramic reinforcements, respectively.

Electron Microprobe Analysis

An electron microprobe analyzer (EMA or EPMA for electron probe microanalyzer) combines electron microscopy with X-ray microanalysis, making it possible to determine the qualitative and quantitive elemental constituents of an unknown material. EMA's are routinely used by the medical profession to perform histological examinations. However, they are equally effective in analyzing non-biological materials such as minerals and man-made materials.

An EMA uses a heated tungsten filament (or similar electron source) to produce an electron beam, or probe [65]. The probe size generally ranges from 0.1-1.0 μm, and its energy ranges from 5-30 keV. The electron beam is focused on a small area of a specimen. As the beam strikes the atoms of the specimen, inner-shell electrons are ejected from the atoms. Characteristic X-rays are then emitted as outer-shell electrons fill the vacancies left behind by ejected electrons. Those characteristic X-rays with the greatest intensity are used to characterize the atoms. An analyzing

crystal (chosen for its lattice spacing, d) is used to reflect a fraction of the emitted X-rays to a wavelength-dispersive spectrometer; the analyzing crystal is rotated through an angular range. Only those X-rays which satisfy Bragg's law reach the detector to be analyzed. Bragg's law may be expressed as follows:

$$n\lambda = 2d \sin\theta$$

where n is an integer, λ is the wavelength of the diffracted X-rays, d is the crystal lattice spacing, and θ is the angle at which the X-rays strike the crystal.

The results from an electron microprobe analysis are often presented in the form of a spectra. The spectral lines comprising this spectra represent different wavelengths. The three main spectral lines in order of decreasing X-ray intensity are: K lines (E_l-E_k transition), L lines (E_m-E_l transition), and M lines (E_n-E_m transition) [66]. These lines are further classified according to electron jumps within shells; e.g., $K_{\alpha 1}$, $K_{\alpha 2}$, $K_{\beta 2}$, $K_{\beta 2}$, etc. The elemental composition of the specimen may be calculated using the wavelengths appearing in the spectra and Moseley's Law, expressed as follows [65]:

$$1/\lambda = k\,(Z-\sigma)^{1/2}$$

where λ is the X-ray wavelength, k is a spectral-line series constant, Z is the atomic number of the element from which the X-ray originates, and σ is a constant related to atomic screening effects. Three correction factors also must be used in the microanalysis of bulk specimens to account for the effects of X-ray fluorescence (F), X-ray absorption (A), and atomic number (Z) - the

correction procedure is known as FAZ or ZAF [66]. If not corrected, these effects will artificially increase or decrease the concentration of elements within a sample.

In addition to the references cited above, there are two recently published texts which explain the latest developments in X-microanalysis, specimen preparation, and data analysis. These texts are: *Scanning Electron Microscopy and X-Ray Microanalysis: A Text for Biologists, Materials Scientists, and Geologists* written by Goldstein *et al* (1992) [67], and *Electron Beam X-Ray Microanalysis* by Heinrich (1981) [68].

The electron microprobe has not been extensively used in the characterization of ceramic matrix composites. However, at least two investigations of ceramic composites which have involved EMA have been identified. Frety and Boussuge used X-ray scanning pictures (elemental maps) from an electron microprobe analysis to prove that thermal ageing increases the oxygen content of Nicalon fibers [69]. EMA also has been used by Lee to characterize oxidation gradients within heat-treated Nicalon reinforced CAS-II [70].

Acoustic Emission Monitoring

Acoustic emission monitoring was not emphasized in this investigation; however, several sources are provided in the listing of references. Among these sources, Chapter 12 in *Nondestructive Testing Techniques* [71] entitled "Acoustic Emission Technology" provides detailed information on the following AE topics: basic concepts, techniques and practices, instrumentation systems, and applications. Arrington [72] has written an overview of the changes occurring in AE technology, particularly in materials characterization, equipment and techniques, and applications. A few papers focusing on the application of AE to composite materials are also included. R. Pyrz [73]

and J. Block [74] have addressed the use of AE inelastic-modeling of composite materials and AE real-time inspection of composite structures under thermal and mechanical loads, respectively. Finally, J. G. Bakuckas, Jr. *et al* [75] have used AE to study damage growth in titanium matrix composites

2-4. High-Temperature, Destructive Testing of CMC's

Like NDT techniques, destructive testing methods are also undergoing a transformation with respect to advanced materials. Advanced materials, such as fiber-reinforced ceramic matrix composites, are structures rather than materials. Accordingly, the methods for testing these advanced materials should reflect this fact [76]. Several papers have assessed the latest equipment and procedures used to destructively test ceramic matrix composites in ambient conditions and harsh high-temperature environments.

Mecholsky [76] has described specimen configurations, test fixtures, and testing methods used to determine the following mechanical properties of CMC's: (1) strength - tensile, flexural, compressive, and shear; (2) elastic moduli - Young's modulus, Poisson's ratio, shear moduli, and dilational (bulk) moduli; (3) toughness/work of fracture; and (4) interfacial bond strength. Although Mecholsky's review is mainly limited to room-temperature testing, it does offer a test configuration for high-temperature tensile testing.

Since one of the main purposes of advanced materials is to withstand severe operating conditions, new test methods and equipment for simulating these same severe conditions continue to be

developed. Special high-temperature furnaces, grips for tensile testing, and contact and noncontact extensometers are currently available for use at temperatures in excess of 2000°C. Baxter [77] has identified the following high-temperature furnaces:

(1) Model 657.03 split-shell furnace by MTS - interfaces with MTS's water-cooled axial extensometer, can be equipped with optical extensometry ports, and has a temperature limit of 1600 °C;
(2) the Short Furnace by Instron Corp. - stands 290 mm high, uses standard out-of-furnace grips, supports mechanical and optical extensometry, and has a temperature limit of 1600 °C;
(3) the split-shell furnace by Zwick of America, Inc. - stands 620 mm high with a 460 mm diameter, can be used with most universal testing machines, and operates within the temperature range, 800-1600 °C;
(4) TTI300 split-tube furnace by Satech Systems, Inc. - can be equipped with windows or ports for optical extensometry and has a temperature limit of 1650 °C;
(5) Model 1800 by Astro Industries, Inc. - can maintain a maximum temperature of 2500°C and a vacuum of 0.13 μPa, and has equipment for monitoring (during testing) changes in the specimen's dimensions and weight, and the atmosphere's composition.

In addition to these furnaces, Baxter [77] has described several new high-temperature extensometers and specimen grips. MTS has designed a water-cooled axial extensometer which can be used at temperatures up to 2000 °C; the extensometer includes alumina, silicon carbide, or carbon/carbon composite extension rods. MTS also has developed water-cooled grips for high-temperature tensile-testing of flat specimens. In cooperation with Oak Ridge National Laboratory (ORNL), Instron has developed the self-aligning Super Grip which provides pure uniaxial loading (35 kN max.) at temperatures up to 1600 °C. Finally, Zygo Corporation offers a laser extensometry system which can be used at temperatures up to 2500 °C.

Another example of high-temperature testing equipment is the physical simulation system known as the Gleeble 2000 (Duffers Scientific, Inc.) [78]. The Gleeble 2000 can reproduce, on a smaller scale, the harsh environments in which a material is fabricated or must operate. This system is

currently being used by researchers from China's Harbin Institute of Technology to investigate the high temperature (1600 to 3000°C) tensile properties of a three-dimensional, fabric carbon/carbon composite. The most attractive feature of this system is its method of heating specimens. The system uses rapid resistive self-heating which involves applying an electrical current to the specimen. The electrical resistance of the material causes the temperature of the specimen to rise in response to the electrical current. This resistance-heating method makes it possible to establish isothermal planes, perpendicular to the applied tensile force. This, in turn, improves the reliability of the results by eliminating the complications caused by radial thermal gradients.

Bartlett *et al* [79] have reported on the work being done at the Southwest Research Institute (SwRI) to characterize monolithic materials and composites at temperatures approaching 2200 °C. SwRI currently has the capability to perform uniaxial monotonic or cyclic loading tests at 1500 °C and biaxial (tension or compression with torsion) static or cyclic loading tests at 1200 °C. SwRI also has equipment for performing creep tests up to 2300 °C in a vacuum or up to 2000 °C in inert gas, and friction and wear tests up to 1000 °C. The research group also boasts two new test systems: an SEM equipped with a high-temperature (850 °C) loading stage, and the DISMAP system (measurement of micro *dis*placements by *ma*chine vision *p*hotogrammetry) for recording deformation and fracture during mechanical and thermal loading.

3. TESTING STRATEGY

3-1. Specimen History

A 2-D fabric-reinforced Nicalon/SiC composite fabricated by the chemical vapor infiltration process (CVI) was used in this investigation. The Nicalon fiber reinforcements were coated with a thin layer of pyrolytic carbon. Nicalon fibers have the following properties [5, 12, 16]:

Composition (wt %): 59 Si, 31 C, 10 C
Diameter (μm): 10-20
Density, *nominal* (Mg/m^3): 2.55
Tensile Strength (MPa): 2520-3290
Young's Modulus (GPa): 182-210

The fabric layers were woven in an 8 HSW pattern (**Figure 1**). Amercom manufactured the composite panels from which the coupons were cut.

Ten specimens were obtained for this investigation. Nine of the received specimens were tapered coupons (**Figure 2a**): AM-7-2, AM-7-3, AM-7-4, AM-7-5, AM-7-6, AM-1-5, AM-1-6, AM-1-7, and AM-2-1. The tenth specimen, AM-8-1, was straight-sided with a centered hole (**Figure 2b**). Specimens AM-7-2, AM-7-3, AM-7-4, AM-7-5, AM-7-6, and AM-8-1 were coated with a CVD SiC coating to delay oxidative degeneration which occurs with high-temperature testing in air. The specimens which received this coating were visibly different. Those specimens which were coated had a rough, dull-grey surface finish, in contrast to the smooth, reflective-black surface finish of the uncoated specimens (**Figures 3a and 3b**).

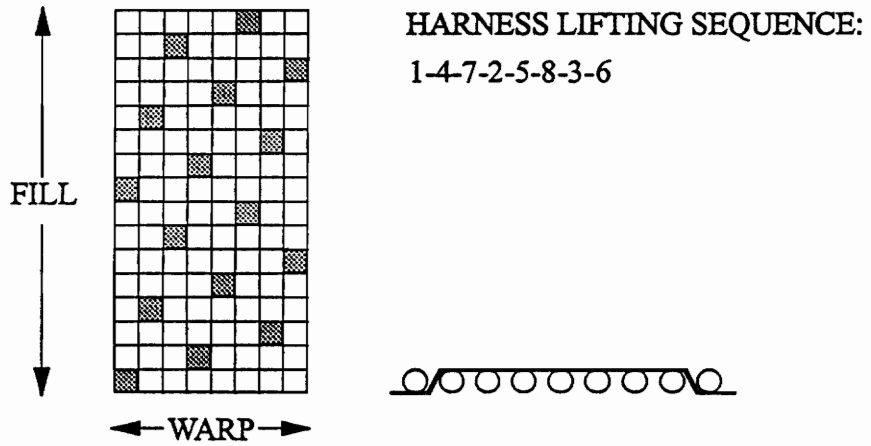

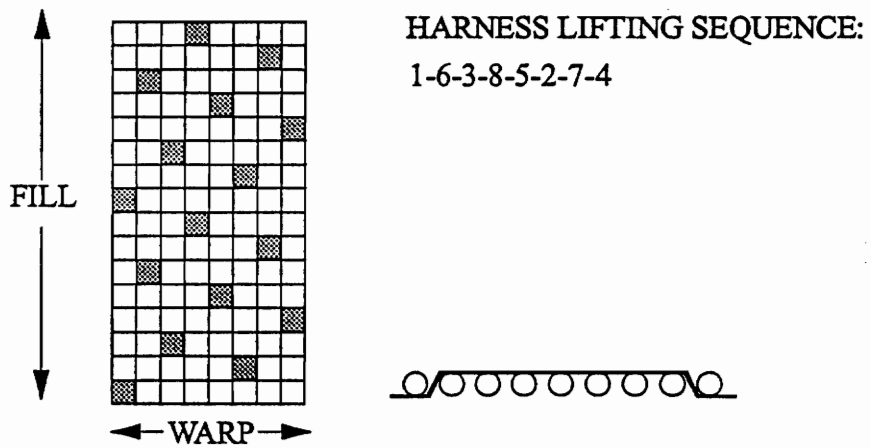

FIGURE 1: Regular eight-harness satin patterns.

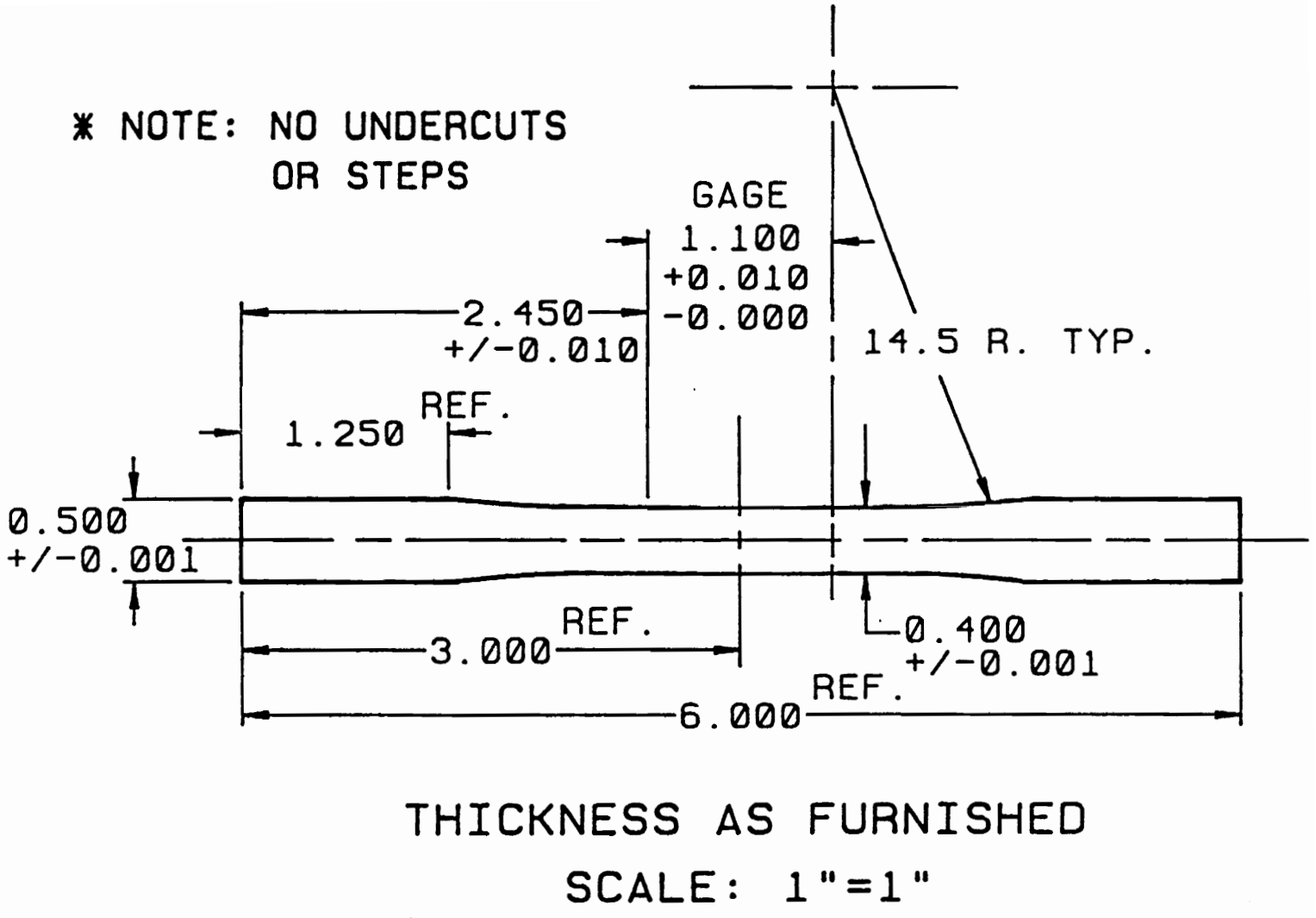

FIGURE 2a: Tapered coupon geometry.

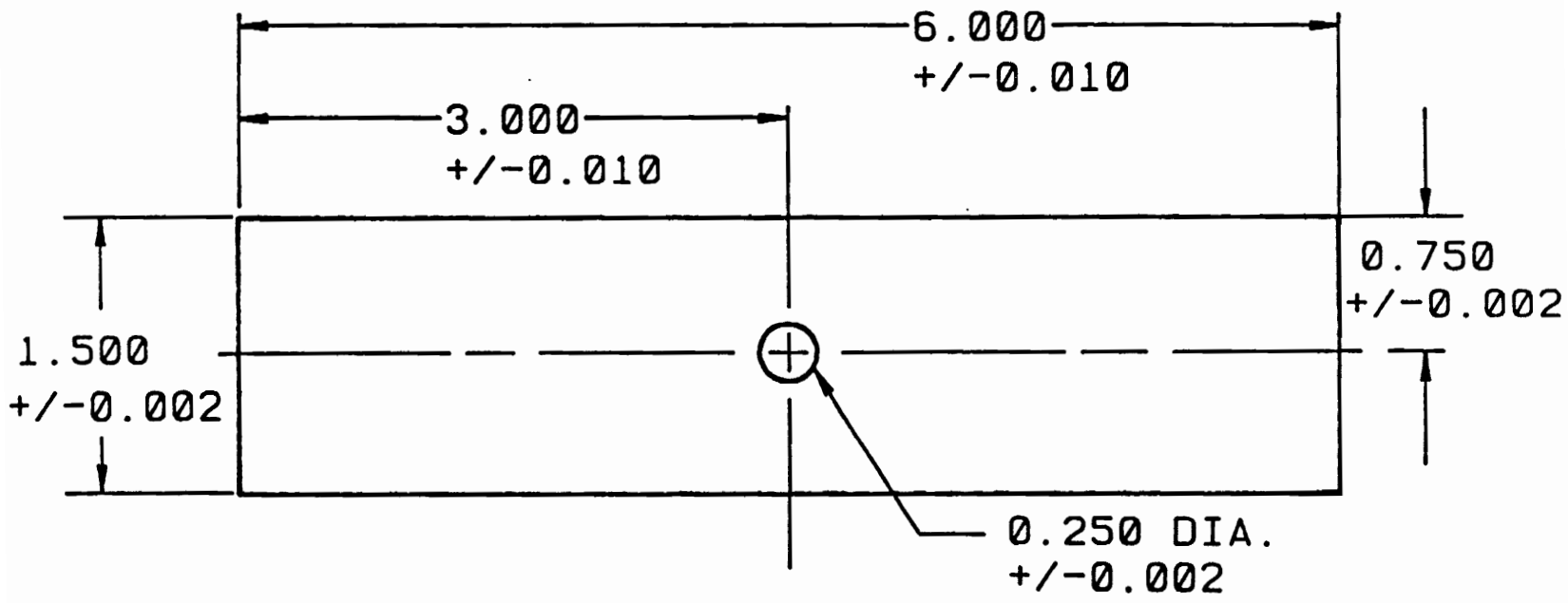

FIGURE 2b: Open-holed coupon geometry.

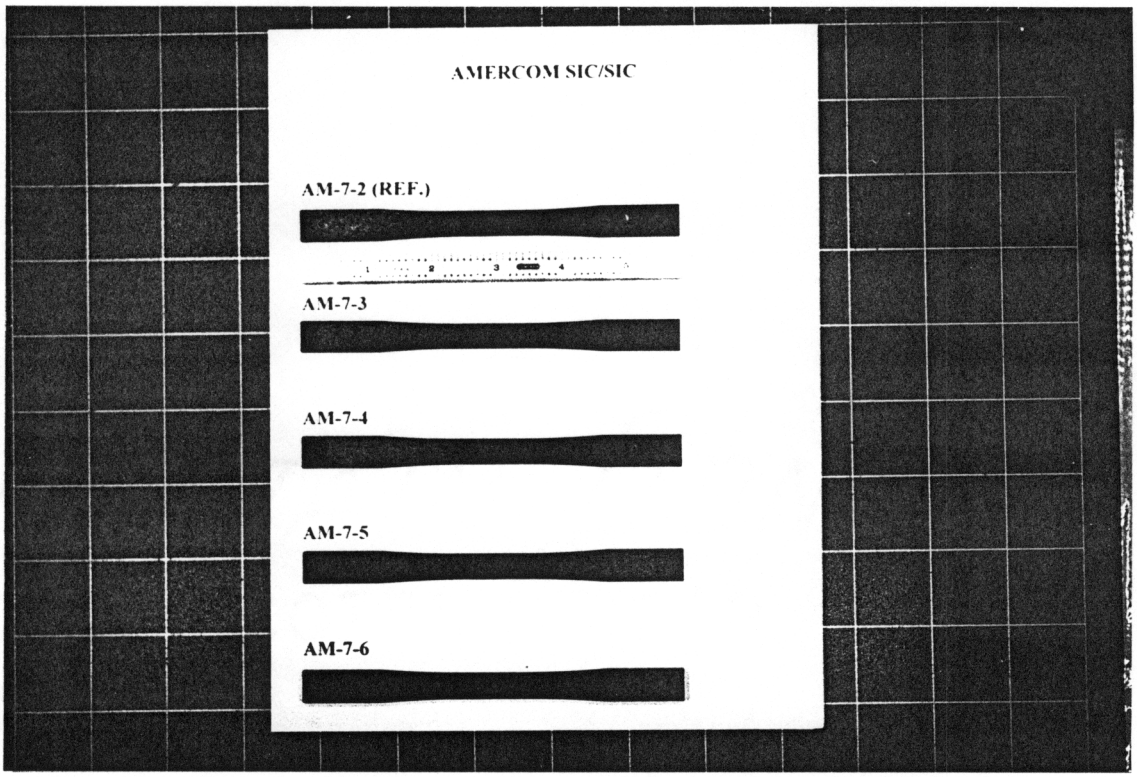

FIGURE 3a: Surface appearance of coated specimens AM-7-2, AM-7-3, AM-7-4, AM-7-5, and AM-7-6. (Coated specimens are not reflective.)

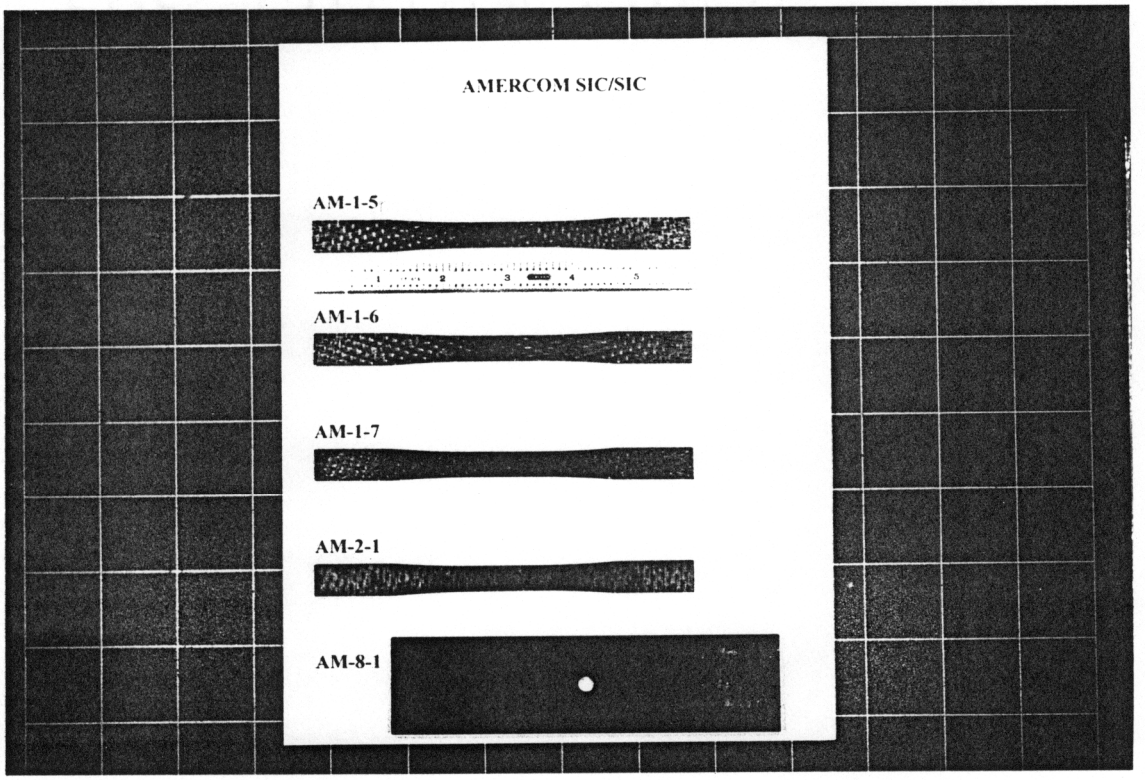

FIGURE 3b: Surface appearance of uncoated specimens AM-1-5, AM-1-6, AM-1-7, AM-2-1, and coated specimen AM-8-1. (Uncoated specimens are reflective.)

Prior to testing, each Amercom specimen was weighed and its dimensions were measured. After heat treatment, the specimens were again weighed and measured. These results are provided in **Table 2a, 2b and 2c**.

3-2. Heat Treatment

Based on the findings of past high-temperature investigations of Nicalon/SiC composites and the limitations of available ceramic furnaces, three temperatures were chosen for this study: 1000 (1832), 1200 (2192), and 1400 °C (2552 °F). Accordingly, the specimens were divided into three groups of three, with at least one coated and uncoated specimen included in each group. The groups are as follows: (1) 1000 °C - AM-1-7, AM-2-1, and AM-8-1, (2) 1200 °C - AM-1-6, AM-7-5, AM-7-6, (3) 1400 °C - AM-1-7, AM-7-3, and AM-7-4. Specimen AM-7-2 was chosen to be the "reference" specimen and was kept in its as-fabricated state; AM-7-2 is to be used as a standard for comparing NDE results.

A Deltech box-furnace with an 818 Eurotherm Controller was used to heat treat the Nicalon/SiC coupons. The coupons were placed on two alumina spacers (in the same horizontal plane) so that they would not contact the bottom of the furnace. The furnace was programmed to perform three functions: (1) increase its temperature during a 16-hour period until the assigned maximum temperature was reached and temperature stability was achieved, (2) maintain the maximum temperature for 100 hours, and (3) decrease its temperature during a 16-hour period until ambient temperature was reached. All of the specimens were heat treated in an ambient atmosphere.

TABLE 2a: Thermogravimetric analysis of specimens.

SPECIMEN	AM-7-2	AM-7-3		AM-7-4		AM-7-5		AM-7-6	
	REF.	RT	1200 C	RT	1200 C	RT	1400 C	RT	1400 C
MASS, g	13.611	13.455	13.525	13.388	13.455	13.455	13.538	13.458	13.546
LENGTH, in.	5.847	5.797	5.796	5.804	5.805	5.847	5.845	5.842	5.842
WIDTH, in.									
top	0.503	0.503	0.503	0.503	0.503	0.503	0.503	0.503	0.502
transition	0.422	0.421	0.422	0.422	0.420	0.422	0.420	0.421	0.421
center	0.406	0.407	0.404	0.405	0.405	0.405	0.405	0.403	0.403
transition	0.422	0.419	0.417	0.420	0.423	0.422	0.417	0.419	0.419
bottom	0.504	0.503	0.503	0.503	0.502	0.504	0.503	0.503	0.502
THICKNESS, in.									
top	0.135	0.133	0.133	0.132	0.132	0.134	0.133	0.134	0.134
transition	0.133	0.132	0.130	0.131	0.131	0.131	0.130	0.132	0.132
center	0.133	0.131	0.130	0.130	0.129	0.132	0.131	0.132	0.131
transition	0.133	0.131	0.131	0.130	0.130	0.131	0.130	0.131	0.130
bottom	0.133	0.130	0.130	0.129	0.129	0.130	0.129	0.132	0.133

TABLE 2b: Thermogravimetric analysis of specimens.

SPECIMEN	AM-1-5		AM-1-6		AM-1-7		AM-2-1	
	RT	1400 C	RT	1200 C	RT	1000 C	RT	1000 C
MASS, g	12.390	12.460	12.412	12.433	12.507	12.496	13.433	13.380
LENGTH, in.	5.844	5.840	5.842	5.837	5.792	5.791	5.748	5.743
WIDTH, in.								
top	0.500	0.499	0.500	0.500	0.500	0.500	0.500	0.500
transition	0.421	0.415	0.417	0.418	0.419	0.421	0.420	0.424
center	0.400	0.400	0.400	0.400	0.400	0.400	0.400	0.400
transition	0.420	0.419	0.421	0.418	0.418	0.415	0.417	0.414
bottom	0.500	0.500	0.500	0.499	0.500	0.500	0.499	0.500
THICKNESS, in.								
top	0.127	0.126	0.124	0.123	0.126	0.127	0.134	0.135
transition	0.125	0.124	0.123	0.123	0.126	0.126	0.133	0.134
center	0.124	0.124	0.124	0.123	0.125	0.125	0.133	0.133
transition	0.125	0.123	0.125	0.123	0.128	0.128	0.132	0.132
bottom	0.125	0.124	0.127	0.127	0.128	0.129	0.132	0.133

TABLE 2c: Thermogravimetric analysis of specimen.

SPECIMEN AM-8-1	RT	1000 C
MASS, g	45.467	45.676
LENGTH, in.	5.977	5.972
WIDTH, in.		
top	1.506	1.505
1" from center	1.507	1.505
center	1.508	1.505
1" from center	1.506	1.505
bottom	1.504	1.504
THICKNESS, in.		
top	0.140	0.139
1" from center	0.138	0.138
center	0.135	0.135
1" from center	0.134	0.134
bottom	0.135	0.137

SPECIMEN AM-8-1	RT	1000 C
HOLE DIA., in.	0.247	0.246
HOLE EDGE TO TOP, in.	2.870	2.868
HOLE EDGE TO BOTTOM, in.	2.870	2.867
HOLE EDGE TO LEFT, in.	0.634	0.632
HOLE EDGE TO RIGHT, in.	0.633	0.631

3-3. Test Matrix

A test matrix was created to maximize the information that could be obtained from the limited number of CMC specimens. The matrix summarizes the nondestructive tests performed on the specimens before and after they were heat treated. The test matrix is included in **Table 3**.

TABLE 3: Test Matrix

SPECIMEN ID.	REF. SPECIMEN AM-7-2	AM-1-7 AM-2-1 AM-8-1	AM-1-6 AM-7-3 AM-7-4	AM-1-5 AM-7-5 AM-7-6
Acoustic Microscopy	RT	RT	RT	RT
		1000 C	1200 C	1400 C
Acousto-Ultrasound	RT	RT	RT	RT
		1000 C	1200 C	1400 C
Electron Microprobe		RT		RT
		1000 C		1400 C
Film Radiography	RT	RT	RT	RT
		1000 C	1200 C	1400 C
Optical Microscopy	RT	RT	RT	RT
		1000 C	1200 C	1400 C
SEM		RT		RT
		1000 C		1400 C
Ultrasonic C-scan	RT	RT	RT	RT
		1000 C	1200 C	1400 C
Tensile Test w/ Acoustic Emission Monitoring		1000 C	1200 C	1400 C

Note: RT identifies test performed before exposure to elevated temperatures; specified temperature identifies test performed after 100 hrs. exposure to temperature.

4. NONDESTRUCTIVE TESTING TECHNIQUES

4-1. Scanning Acoustic Microscopy (SAM)

Equipment and Setup

The UH-3 Scanning Acoustic Microscope which was used in this investigation (**Figure 4**) is a reflection instrument that relies on a self-aligning or confocal lens to transmit and receive pulsed acoustic signals (gated continuous waves). The operating frequency range of this microscope is 30 MHz - 1 GHz. Using water as the lens-to-specimen coupling fluid, the acoustic microscope was used to perform room-temperature surface and sub-surface examinations of the as-fabricated and heat-treated CMC specimens. A surface examination was performed by focusing the acoustic microscope on the surface of the specimen ($z = 0$); similarly, a sub-surface examination was performed by moving the specimen closer to the lens (-z or defocus) so that the focal plane would lie inside the specimen. After signal processing, the information collected from the scans was then formatted as C-scan images of amplitude vs. position. (A C-scan is an image of an object's surface or of a plane internal to the object and parallel to the scanning plane.) The C-scan images (SAM micrographs) provided defect maps of the surface and sub-surface planes of the CMC specimens.

Procedure

Before proceeding with the analysis, the specimens were submerged in distilled water at room temperature in the acoustic microscope's scanning tank. Testing did not begin until bubbles, caused by out-gassing, stopped appearing on the specimens' surfaces. Trial investigations of the CMC specimens were performed using 30, 50, and 100 MHz lenses; the 30 MHz lens yielded poor

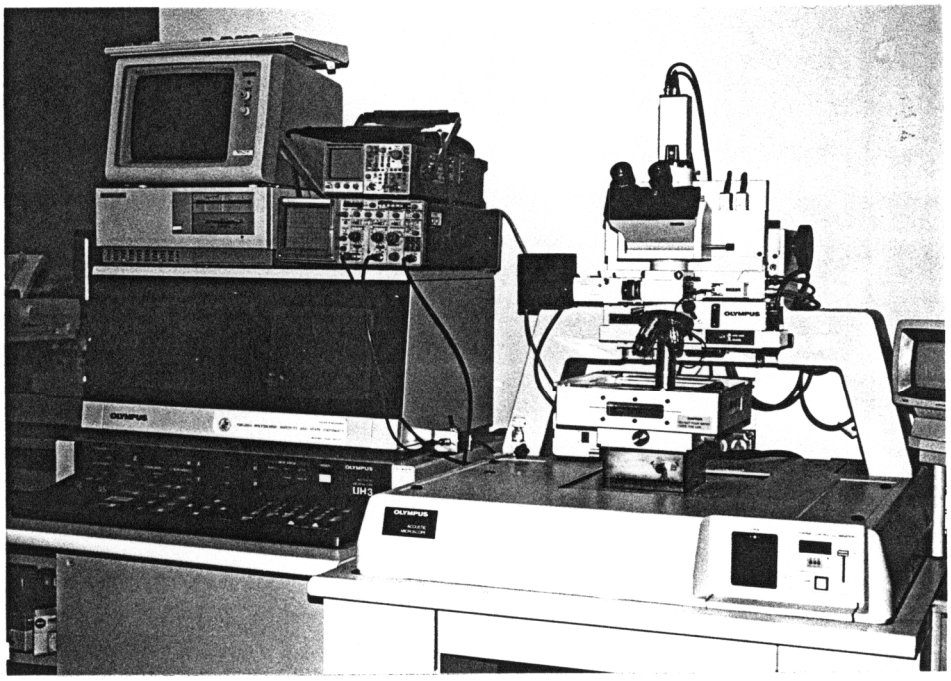

FIGURE 4: The scanning acoustic microscope used in this investigation.

resolution and 100 MHz did not provide sufficient penetration depth. Based on these trials, the 50 MHz lens was chosen for this study (**Appendix B**).

The lens frequency is one of five significant parameters defining an SAM investigation. These parameters are identified with their abbreviated forms as follows: (1) lens frequency - **F**{Hz}; (2) relative position of the lens and the surface of the specimen; the position of the lens is defined as z = 0 when the lens is focused on the surface of the specimen - **z**{mm}; (3) electrical attenuation required to keep the received signal within the operating range of the equipment - **A**{dB}; (4) two-way travel time of the gated amplitude peak used to create the image - **T**{μs}; and (5) scan width of specimen - **x**{mm}. In this investigation the following range of SAM parameters were used: (1) F = 50 MHz, (2) z = -4.02 to 0 mm, (3) A = 0 to 36 dB, and (4) T = 0 to 0.5 μs.

4-2. Acousto-Ultrasonics (AU)

Equipment and Setup

The acousto-ultrasonic system that was used in this investigation is shown in **Figure 5**. The system consists of the following: (1) a Panametrics 5055PR pulser/receiver, (2) an IBM compatible PC based data acquisition system with a Sonotek STR*825 A/D (25 MHz maximum sampling frequency), and (3) two Harisonic dry-coupled contact transducers (type HDC-8702-1.25 MHz) shown in **Figure 6a** which were held in a Harisonic fixture as shown in **Figure 6b**. The pulser/receiver generated a broad-band electrical pulse; it also was used to adjust (amplify or attenuate) the received signal before storage. The two 1.25 MHz piezoelectric transducers, with 5mm diameter polymeric tips, were dry-coupled to the test specimen to transmit and receive

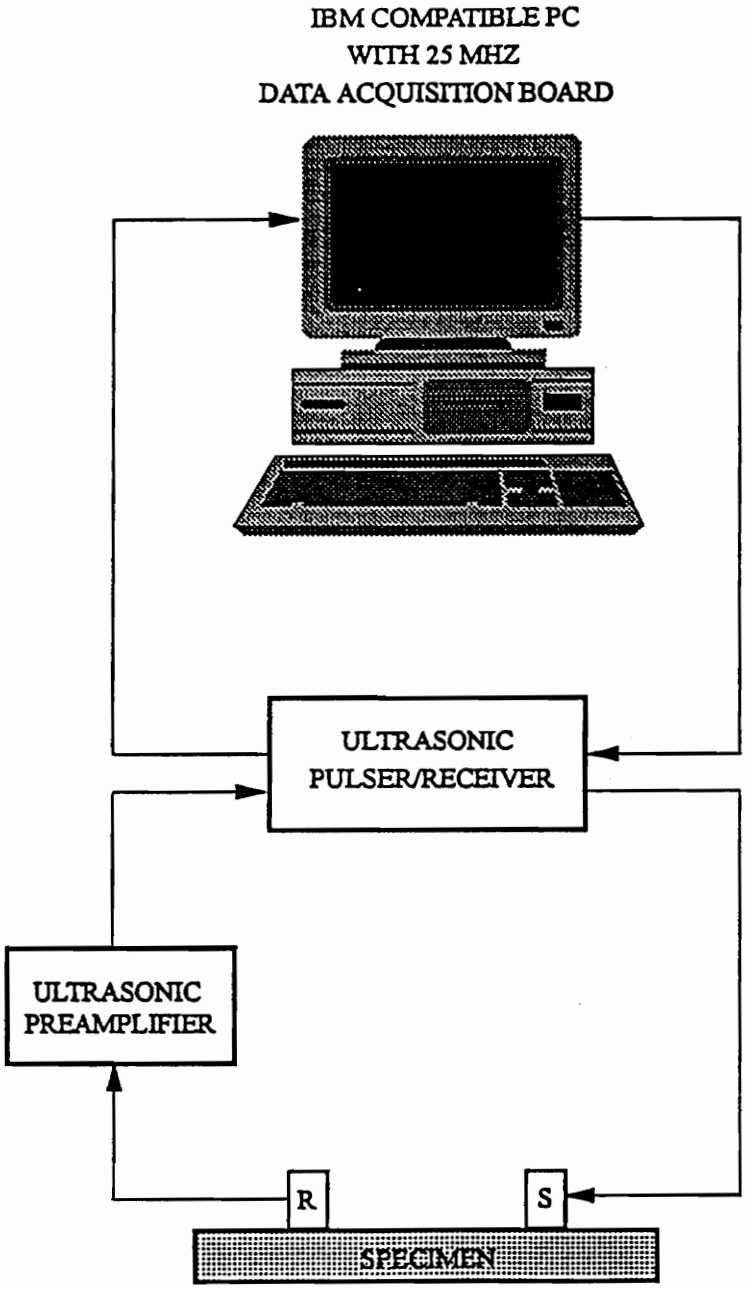

FIGURE 5: Acousto-ultrasonics system.

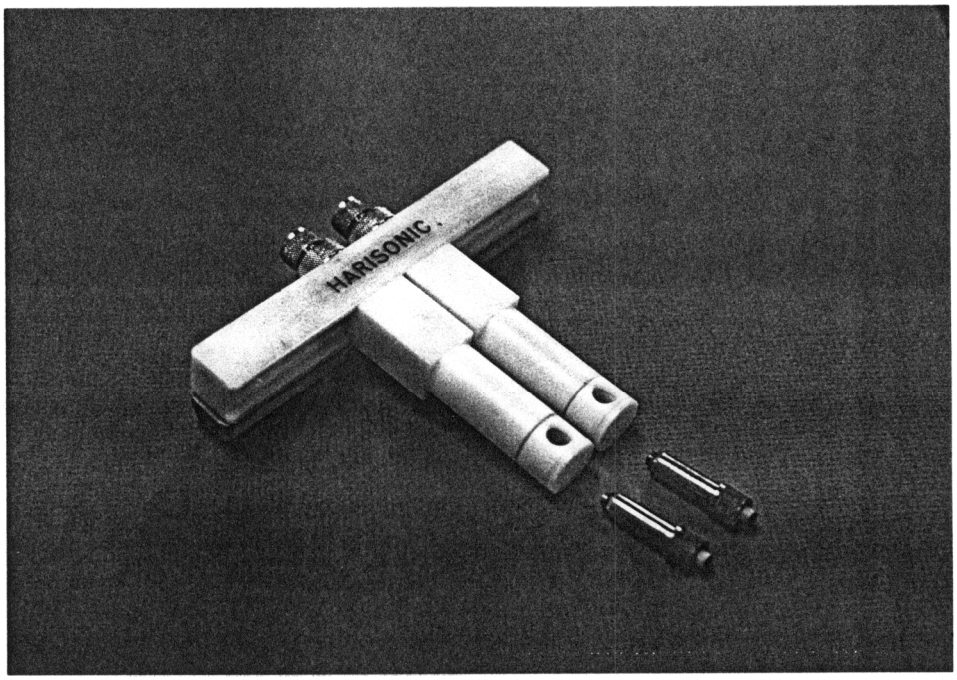

FIGURE 6a: The Harisonic fixture and dry-coupled transducers.

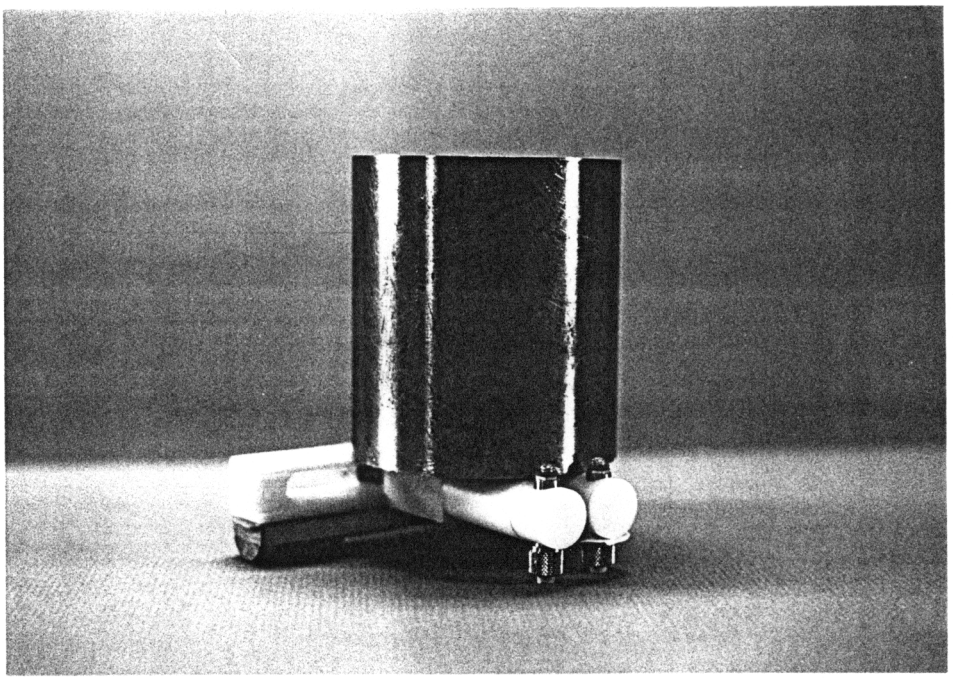

FIGURE 6b: The Harisonic fixture-transducer assembly shown with the 4.65 kg mass.

ultrasonic energy. The source transducer converted the electrical signals from the pulser/receiver to mechanical vibrations which were introduced to the test specimen via the transducer's dry-coupled polymeric tip. The sensor-transducer then received associated stress waves and converted them to electrical signals.

The data acquisition system consists of the DigiScope-25 (DS25) Digital Oscilloscope Program that, together with the analog-to-digital converter board, allows the received signal to be viewed in real-time. The data acquisition system, operating at a 25 MHz sampling frequency, captured and stored the electrical signals so that they could be analyzed and used to interpret the condition of the test object.

Two dry-coupled contact transducers were chosen to eliminate the problems caused by using a liquid couplant with an absorbent, porous material. The sampling frequency was chosen based on the Nyquist Theorem. According to the Nyquist Theorem, the sampling frequency should be at least twice that of the highest frequency in the analyzed signal. The Nyquist Theorem may be mathematically formulated as follows:

$$f_h \leq \tfrac{1}{2}\Delta$$

where f_h is the highest frequency in the analyzed signal, and Δ is the sampling frequency. Accordingly, the maximum frequency, $f_m = \tfrac{1}{2}\Delta$, is defined as the Nyquist frequency.

Procedure

Before AU testing, several preparations were made. The CMC specimens were placed in

cardboard templates. These templates acted as guides for positioning the transducers on the specimen. A scale divided into inches was drawn on the templates along the edge of the specimen-contour so that the transducers could be placed in 1" increments down the center of each specimen. A graphite center-line was also drawn on the specimens to help properly locate the transducers. The transducers were placed in a Harisonic fixture and leveled in a common horizontal plane. A 4.65 kg mass was then placed on the fixture to enhance contact between the polymeric tips of the transducers and the rough surface of the specimens.

Ten trial measurements were made at position 3 (the center of the specimen) on specimen AM-7-2 prior to all AU tests. These trial measurements were made at the beginning of each series of tests to ensure that the equipment was properly setup and to "exercise" the transducers' polymeric tips (**Appendix C**). The polymeric tips were "exercised" because initial tests showed that the SWF parameter, M_0 (area under the power spectral density curve), changed as the elastic deformation of the polymeric tips changed (**Figure 7**). The ten trial measurements were made as follows: the transducers were positioned on the specimen and loaded for one minute; at the end of one minute, a measurement was taken; the transducers were then unloaded and allowed to relax one minute. This same procedure, involving timed loading and unloading, was used to test all of the specimens. Variations in the AU results, caused by elastic deformation of the polymeric tips, were minimized by following this procedure. Other variables affecting the AU measurements, such as the ambient conditions, were minimized by using the trial measurements to normalize the data.

Four AU readings were taken at each of the 5 positions on the tapered coupons. The first and third readings were taken with the transmitter nearest the end of the specimen when the tranducers were in position 1; the second and fourth readings were taken with the receiver nearest the end.

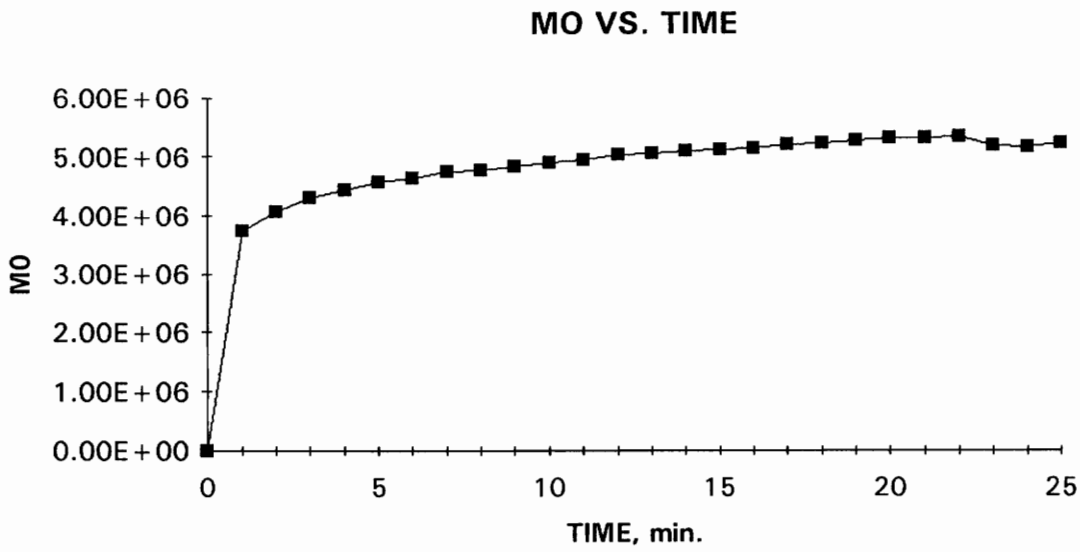

FIGURE 7: The variation in M_0 with respect to time as a constant load is applied to the transducers.

The four sets of readings were taken to study the effects of coupon geometry and material asymmetry. Two AU readings were taken at each of the 16 positions on the "open-holed" or "notched" coupon. Only two readings were taken because of the lack of similarly shaped specimens with which to compare the results. Only the changes caused by thermal exposure were of interest in the "notched" specimen's case.

4-3. Film X-Ray Radiography

Equipment, Setup, and Procedure

The X-ray cabinet that was used in this investigation is an HP Faxitron Series, 43805 X-ray System (**Figure 8**). The lowest shelf setting in the upper compartment of the cabinet was chosen so that the distance between the source and target would be maximized. Kodak Industrex M film, M5 100 - 13x18 cm was used in this investigation because it provided good definition and contrast. Several trial radiographs were taken to determine the kilovoltage and exposure-time settings which produced the optimal radiographs. The trial radiographs taken of the Amercom specimens indicated that for a composite thickness of $\approx$0.125", optimal definition and contrast could be obtained with a kilovoltage setting of 45 kV and a 2-minute exposure time. These settings were used to make all of the radiographs in this investigation.

The specimens were radiographed as-received, with no surface preparation. The specimens were placed on a sheet of film and oriented so that their identification marks were visible and corresponded to the top of the specimens' film image. (A method of orienting the specimens was needed to facilitate later comparisons among radiographs.) Reference specimen AM-7-2 was

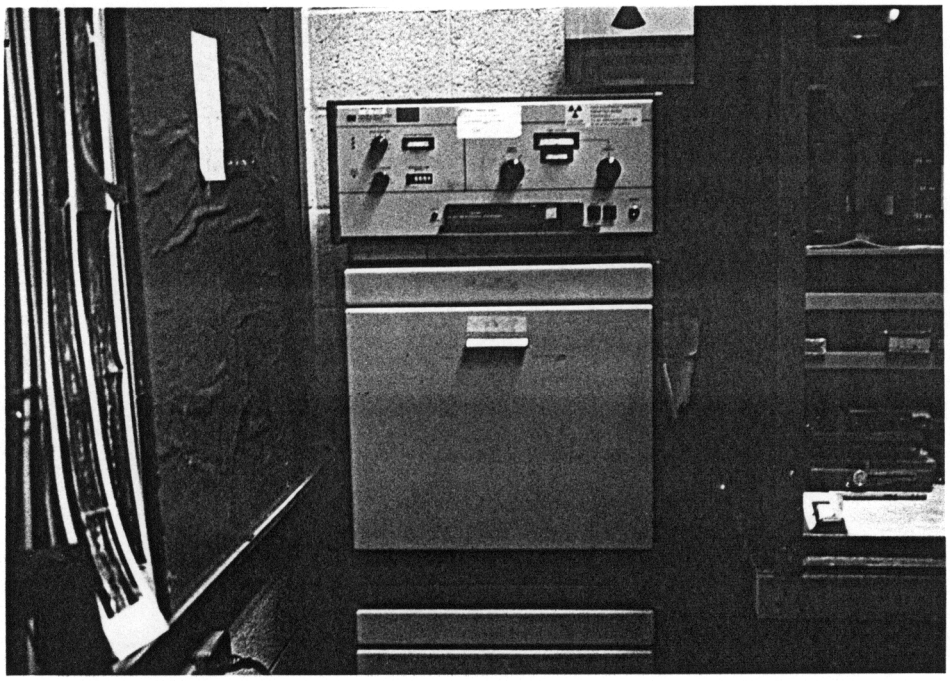

FIGURE 8: The X-ray cabinet used in this investigation.

included in each radiograph so that it could be used as a "reference standard". Once the specimens were positioned on the film and identified by lead numbers/letters, the assemblage was centered over the X-ray target in the X-ray cabinet and a radiograph was made. The film was then developed as follows: (1) 5 minutes in developer, (2) 1 minute in rinse, (3) 5 minutes in fixer, and (4) 10-15 minutes in running-water rinse. Positive prints were then made from these film negatives.

4-4. Immersion Scan Ultrasonics

Equipment and Setup

The Sonotek (Sonix) C-Scan System that was used in this investigation is shown in **Figure 9**. The system consists of the following: (1) an Ultrasonic Analyzer, Model 50520, (2) an IBM compatible PC based data acquisition system with a Sonotek STR*8100, 100 MHz A/D converter board, (3) a three axis (X-Y-Z), stepper-motor controlled, precision scanning bridge with +/- 0.001" positional accuracy, (4) a Sonotek MC-33 stepper-motor controller, (5) a 5 MHz, 0.5" diameter, 3.0" focal length, Ultran transducer; a 25 MHz, 0.25" diameter, 0.5" focal length, Harisonic transducer; and a Valpey Fisher pinducer, (6) a transducer fixture for through-transmission mode scanning, and (7) an immersion tank filled with water. The Ultrasonic Analyzer was used to amplify or attenuate the received signal before the signal was stored. The 5 MHz and 25 MHz piezoelectric, immersion transducers were used to transmit ultrasonic energy; the pinducer was used with either transmitter to receive the energy after it had interacted with the specimen. The water-coupled transmitter and receiver were axially aligned in the fixture so that the transmitted and received ultrasonic pulses would interact with the specimen at normal incidence.

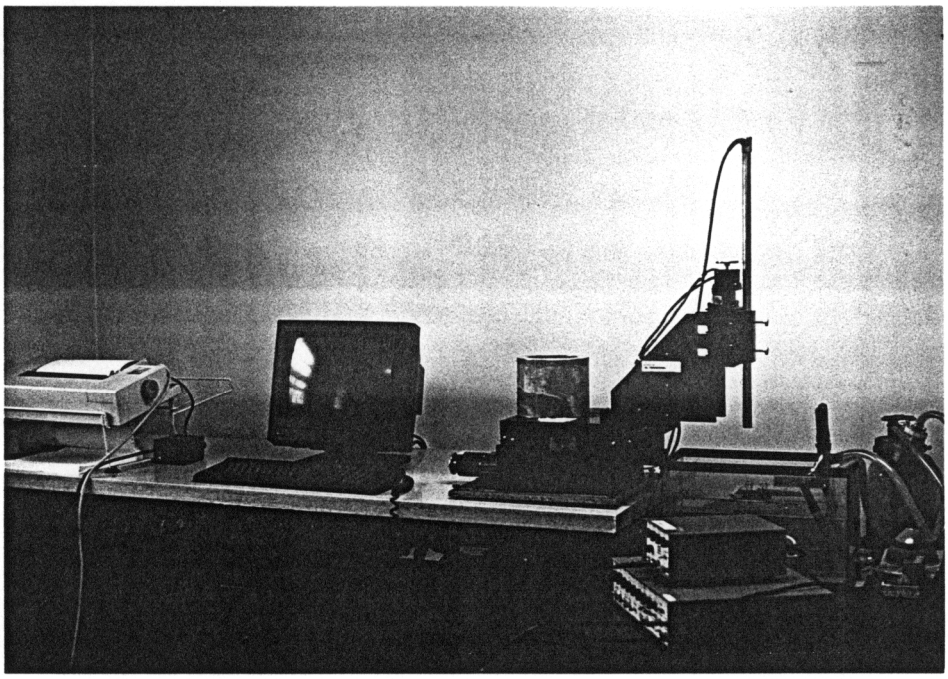

FIGURE 9: The C-scan system used in this investigation.

The data acquisition system uses a 100 MHz digitzer board to capture and store the signals received by the pinducer so that they may be analyzed in an A-, B-, or C-scan or time-of-flight format. The data acquisition system also consists of the Sonix-Ultrasonic C-Scan Program (v. 3.1) and the C-VUE Image Processing and Enhancement Program (v. 3.1). These programs, together with the A/D converter board, make it possible to view the color-enhanced ultrasonic data on the monitor in real-time.

Procedure

The Amercom specimens were immersed in water for several minutes to ensure that bubbles from out-gassing would not interfere with ultrasonic testing. While the specimens were soaking, the scanning bridge and immersion tank were horizontally leveled using a 360-degree bubble level. A Plexiglas platform was placed in the immersion tank and also horizontally leveled. The transducer-fixture was attached to the arm of the scanning bridge, and the sending and receiving transducers were horizontally aligned in the fixture. This was done by using the through-transmission mode to maximize the amplitude of the signal as seen in real-time in the oscilloscope trace. Similarly, the transmitting transducer was focused on the front surface of a specimen lying on the Plexiglas platform. Focusing was accomplished by using the pulse/echo mode to maximize the amplitude of the front-surface echo as seen in real-time in the oscilloscope trace.

The Ultrasonic Analyzer was used to adjust the output signal. The test parameters used were as follows: (1) trigger mode - internal trigger, (2) high pass filter - out, (3) damping - 0, (4) attenuation - 18 dB, (4) energy - 4, and (4) gain - 60 dB. The distance between the transmitter and the specimens and the separation between transmitting and receiving transducers were maintained so that the results would be comparable. The specimens were ultrasonically scanned in through-

transmission mode with reference specimen AM-7-2 occupying the left-most position in each scan. A color-enhanced C-scan image was created on the monitor during the scanning process. The image processing program arbitrarily assigned each color-band to represent a range of signal amplitudes; these color-bands were adjusted after scanning. C-scans made before and after thermal exposure were color adjusted so that reference specimen AM-7-2 would appear the same in each scan and, thus, facilitate comparison.

5. ADDITIONAL TECHNIQUES FOR CHARACTERIZING CMC'S

5-1. Optical Microscopy

Equipment, Setup, and Procedure

Prior to optical examination and electron microprobe analysis, samples were cut from as-fabricated and heat-treated specimens using a slow annular diamond wheel (100-125 rpm) lubricated by a continuous stream of water. The samples were cut from the end of the specimens (opposite the I.D. number); care was taken to keep the samples small so that their removal would not interfere with later tensile tests. These specimens were mounted in cold-cure epoxy. The mounted specimens were then polished using a series of SiC papers and diamond paste, cleaned in an ultrasonic bath, and rinsed with distilled water and isopropyl alcohol (**Appendix D**).

A Nikon Epiphot Inverted Microscope, equipped with a 35 mm Nikon camera (FX-35WA) and a Polariod camera, was used to make optical micrographs of polished specimens. Optical micrographs were made before the electron microprobe analysis (discussed in the following section) so that the gold sputtering would not interfere with the specimens' surface appearance.

5-2. Electron Microprobe Analysis (EMA)

Equipment and Setup

A Cameca SX50, fully automated electron microprobe analyzer was used in this investigation. The Cameca system includes a Sun 3160 computer with PAP software for data reduction, and four

wavelength dispersive spectrometers. Three different man-made analyzing crystals were used for X-ray analysis: (1) pseudo-crystal 1 (PC1), 2d = 61.4 A, (2) lead stearate film (ODPB), 2d = 100.7 A, and (3) thalium acid phthalate (TAP), 2d = 25.7 A. The TAP crystal was used for Si Kα diffraction; the PC1 crystal which does not diffract well-ordered radiation was used for analysis purposes. The spot-size of the electron beam used to perform the analysis was approximately 1μm in diameter.

Procedure

In this investigation the EMA was used to characterize the changes which took place in the fiber-matrix interphase after the CMC had been exposed to 1400 °C. Samples from as-fabricated specimens, AM-7-2 and AM-1-7, and from specimens heat treated at 1400 °C, AM-7-6 and AM-1-5, were chosen for analysis. These specimens were chosen because they represented the coated and uncoated specimens at the two temperature extremes. In preparation for analysis, small letters were stamped on the epoxy surrounding the samples, and the samples were gold-sputtered so that they would be electrically conductive. These samples were then placed in the EMA chamber and kept in a vacuum for approximately 24 hours before beginning the analysis.

A fiber from the as-fabricated sample AM-1-7 was scanned and the elemental composition of Nicalon (59 wt% Si, 31 wt% C, and 10% O) was used as the scan standard - this was used in the absence of a more accurate standard. Silicon, carbon, and oxygen maps were prepared to illustrate elemental gradients and help visualize the chemical composition of the fiber. Trace/line scans were prepared for each of the four specimens to provide a more detailed explanation of the chemical changes taking place in the fiber and the fiber-matrix interphase. In addition, backscatter electron (BSE) images of the four specimens also were made using the SEM capabilities of the EMA.

5-3. Acoustic Emission (AE) Monitoring and Tensile Testing

Equipment, Setup, and Procedure

A Spartan AT System with an IBM compatible 386 based data acquisition system was used to monitor the acoustic emission of the heat treated coupons, as well as load and strain, during tensile testing. A software package written by Physical Acoustics Corporation (PAC) , SA-LOC (v. 1.1), was used to set system parameters and analyze data. A single (5/16" dia.) resonant sensor, with peak frequencies at 30 kHz and 500 kHz, was used to receive the stress waves and convert them to electrical signals.

In preparation for testing, the sensor was clamped on the side of the specimen opposite the extensometer near the bottom of the gage section. The total system gain was set at 50 dB and the threshold was set at 40 dB. Vacuum grease was used as the couplant between the transducer and specimen. AE monitoring was initiated when the tensile test began and proceeded until the specimen had failed.

A Material Test System (MTS) 880 was used to perform monotonic tensile tests on the CMC specimens. The 22-kip servo-hydraulic testing system was equipped with diamond-face hydraulic wedge-grips; an MTS 4% extensometer with a 1" gage length was used to measure strain. The extensometer was attached to the specimen with rubber bands. Metal tabs affixed to the specimen with Silicone adhesive were used to position the extensometer so that it was centered on the specimen.

6. RESULTS AND DISCUSSION

Visual Examination

All of the specimens exhibited surface changes after thermal exposure. The surfaces of the coated specimens exposed to 1400 °C and 1200 °C were smoother and darker gray than the specimens' original surfaces. The spaces between fibers were more apparent and, accordingly, the weave pattern was more defined in the heat-treated specimens. These observed changes are attributed to the oxidation of the CVD SiC seal-coat. The surfaces of the uncoated specimens that were heat treated at these same temperatures exhibited less change, although they did become a duller gray. The appearance of the three specimens heat treated at 1000 °C was more noteworthy. Both the coated and uncoated specimens had a pink iridescent surface finish. This iridescence is attributed to the refraction of light by a thin layer of silica covering the uncut surfaces of the specimens.

Thermogravimetric Analysis

In **Tables 2a**, **2b**, and **2c** the dimensions and mass of each specimen before and after heat treatment are reported. The dimensions of all of the specimens remained approximately constant. (Note: The lengths of the as-fabricated specimens are different because small samples were cut from the specimens for optical examination and electron microprobe analysis.) Differences in the dimensions before and after heat-treatment may be attributed to measurement error rather than to thermal exposure. However, in sharp contrast to their dimensional stability, the specimens did exhibit significant mass instability.

The specimens heat treated at 1400 °C experienced the greatest change in mass. The mass of the two coated specimens, AM-7-5 and AM-7-6, increased by 0.62% and 0.65%, respectively; the

mass of uncoated specimen AM-1-5 increased by 0.57%. The discrepancy between the mass change of coated and uncoated specimens was more pronounced in the specimens heat treated at 1200 °C. Coated specimens AM-7-3 and AM-7-4 experienced a mass increase of 0.52% and 0.50%, respectively, as opposed to the 0.17% increase for uncoated specimen AM-1-6. Even more striking are the mass changes associated with the 1000 °C heat treatment. Coated specimen AM-8-1 increased by 0.46% while the masses of uncoated specimens AM-1-7 and AM-2-1 decreased by 0.09% and 0.39%, respectively.

The findings of weight gain parallel the findings of Huger *et al* [16]. Huger *et al* performed a thermogravimetric analysis of Nicalon (NLM 202) fibers after 100 hours of ageing in air at atmospheric pressure and 700, 800, 900, 1000, 1100, and 1200 °C. After thermal ageing, all of the fibers experienced a mass gain; this was attributed to passive oxidation of SiC in the fiber and resulting formation of a silica ring around the fibers. Unlike the investigation undertaken by Huger *et al*, this investigation involved Nicalon fibers embedded in a SiC matrix. However, despite this difference, the same oxidation phenomenon reported by Huger *et al* is believed to be the cause of the specimens' weight gain.

Pluvinage *et al* [80] have offered an even more detailed explanation of this oxidation process. Based on the results of high-temperature ageing of a unidirectional Nicalon/SiC composite, Pluvinage *et al* proposed the following series of phenomena: (1) the interfacial carbon-coating oxidizes leaving interstitial cavities in the fiber-matrix interphase, (2) oxygen diffuses into these cavities and oxidizes the matrix and fibers to form silica layers, and (3) oxygen diffusion slows down as more of the matrix and fibers are oxidized and the cavities are sealed by silica.

The weight loss of the two uncoated specimens, AM-1-7 and AM-2-1, heat treated at 1000 °C may be attributed to the pyrolysis of the fiber sizing. The differences in weight gain between the heat-treated coated and uncoated specimens are also attributed to this pyrolysis phenomenon. Huger *et al* [16] reported that after thermally ageing Nicalon fibers at temperatures between 250 and 500 °C for 100 hours, approximately 1-3% of the mass of the fibers was lost as the fiber sizing (polyvinyl acetate) was pyrolyzed. (Pyrolysis is the chemical change of a substance by means of heat alone. Thermal rearrangements into isomers, thermal polymerizations, and thermal decompositions are also included in the term pyrolysis, but it does not include thermal changes that require catalysts or changes that are initiated by other forms of energy [81]. Normally, the term "pyrolysis" is restricted to heat-induced chemical changes that occur in a vacuum.) Because a SiC matrix surrounded the Nicalon fibers in this investigation, it is possible that the pyrolysis of the fiber sizing was postponed until temperatures closer to 1000 °C were reached. In the case of specimen AM-8-1, the SiC seal-coat may have inhibited the pyrolysis of the fiber sizing. As previously reported, the mass of AM-8-1 increased by 0.46%.

SAM Analysis

The results of the SAM analysis of several specimens before and after heat treatment are shown in **Figures 10-19**. SAM micrographs of coated specimens AM-7-5 (heat treated at 1400 °C) and AM-7-3 (heat treated at 1200 °C) are shown because the before-and-after micrographs were taken at almost the same location on the specimens, using the same SAM parameters, and can be easily compared. SAM micrographs of specimen AM-1-5 and AM-1-6 are included because they represent the uncoated specimens that were heat treated at 1400 °C and 1200 °C, respectively.

Few differences were observed between the surface images of the as-fabricated and heat-treated specimens. Referring to **Figures 10** and **11**, the surface of specimen AM-7-5 before and after heat treatment at 1400 °C is virtually unchanged. However, there is a dark band extending across the width of specimen AM-7-5 which is present after heat treament **(Figure 11)** but not present before heat treatment **(Figure 10)**. This dark band is the only apparent difference in the as-fabricated and heat-treated surface images of specimen AM-7-5. The cause of the band is unknown.

The sub-surface (z = -2.24 mm) images of specimen AM-7-5 before and after heat treatment are shown in **Figures 12** and **13**. Several observations may be made about these sub-surface images. The regions which are highly reflective before heat treatment **(Figure 12)** are also highly reflective after thermal exposure **(Figure 13)**; they appear as white regions in the two images. This suggests two explanations: (1) the elastic properties of the regions were not affected by heat treatment, or (2) the sensitivity of the SAM was not sufficient to distinguish the differences. The dark band which appears in the surface image of heat-treated AM-7-5 **(Figure 11)** does not appear in the sub-surface image of heat-treated AM-7-5 **(Figure 13)**. The band's shadow is obscured by the poor image contrast, but was visible for settings of z, A, and T which enhanced the contrast. The most significant observation is the difference in image contrast between the sub-surface images taken before and after heat treatment.

The sub-surface image of the as-fabricated specimen shown in **Figure 12** has better contrast than the image of the heat-treated specimen shown in **Figure 13**; *i.e.*, the sub-surface of the as-fabricated specimen appears to reflect more of the transmitted acoustic signals. However, as suggested by the amplitude of the signals reflected from the surface, more of the acoustic waves

are reflected at the surface of the heat-treated specimen. Consequently, less acoustic energy is transmitted to the sub-surface, and less is available for reflection from the sub-surface.

The increase in surface reflectivity is related to the oxidation of the SiC seal-coat and the oxidation of the matrix and fibers. Oxidation is accompanied by the formation of silica and the increase in crystallinity of the Nicalon fibers. These changes which also affect the elastic properties of the composite are believed to be responsible for the increase in surface reflectivity of the specimens after heat treatment.

Referring to **Figures 14** and **15**, the surface of specimen AM-7-3 before and after heat treatment at 1200 °C appears to be unchanged. However, the sub-surface ($z = -2.48$) images before and after heat treatment are different; this change parallels the change seen in the sub-surface images of AM-7-5. The sub-surface image of the as-fabricated specimen shown in **Figure 16** has good contrast, while the image of the heat-treated specimen shown in **Figure 17** has poor contrast. As previously explained, the surface of the heat treated specimen reflects more acoustic energy than the surface of the as-fabricated specimen; thus, less energy is transmitted to the bulk of the specimen.

Figures 18 and **19** are surface images of uncoated specimens AM-1-5 and AM-1-6 after heat treatment. Specimen AM-1-5 was heat treated at 1400 °C, and specimen AM-1-6 was heat treated at 1200 °C. The same observations that were made about the SAM images of the coated specimens are also valid for the SAM images of these uncoated specimens. The surface images of the two uncoated specimens are shown in **Figures 18** and **19** to illustrate the differences in texture and weave appearance between the coated and uncoated specimens.

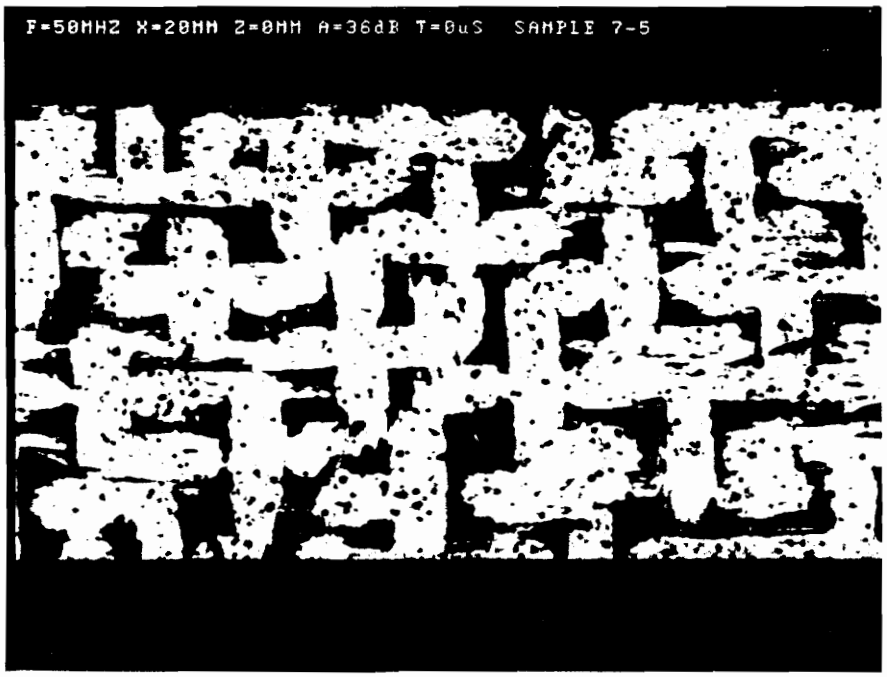

FIGURE 10: Acoustic micrograph of AM-7-5 before heat treatment. (z = 0 mm, A = 36 dB, T = 0 μs)

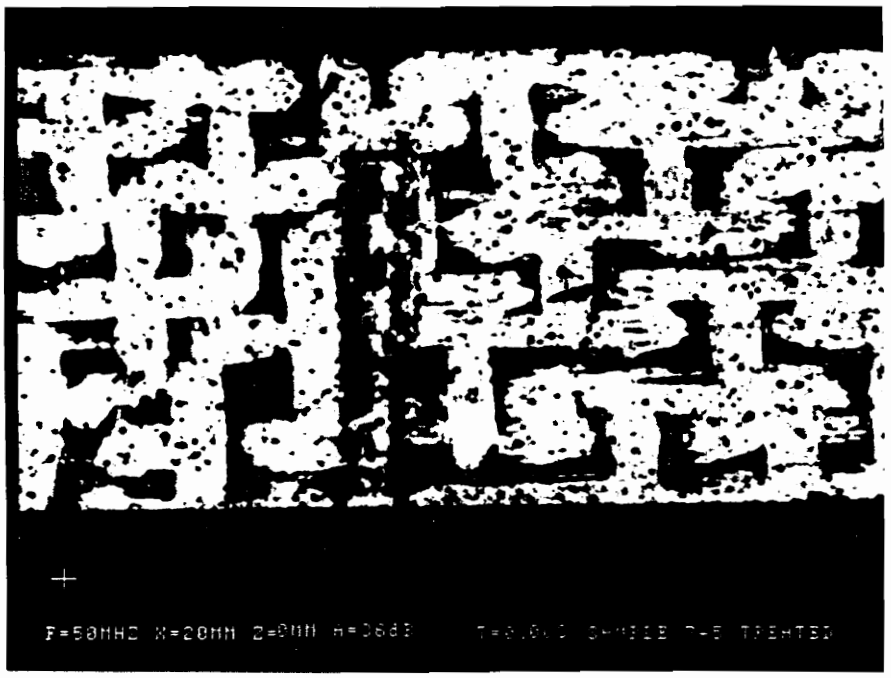

FIGURE 11: Acoustic micrograph of AM-7-5 after 100 hrs. of thermal ageing at 1400 °C. (z = 0 mm, A = 36 dB, T = 0 μs)

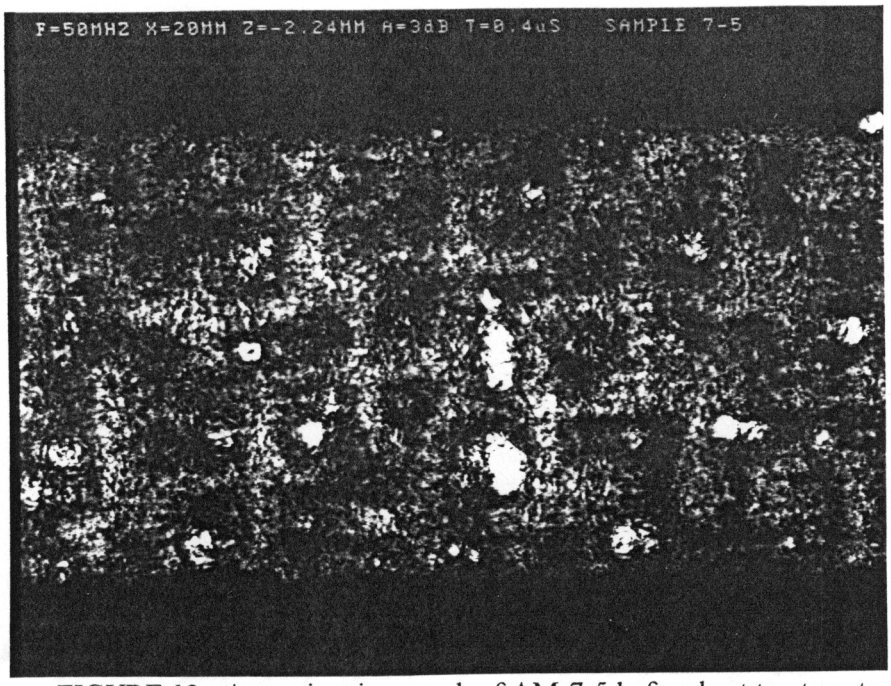

FIGURE 12: Acoustic micrograph of AM-7-5 before heat treatment. (z = -2.24 mm, A = 3 dB, T = 0.4 μs)

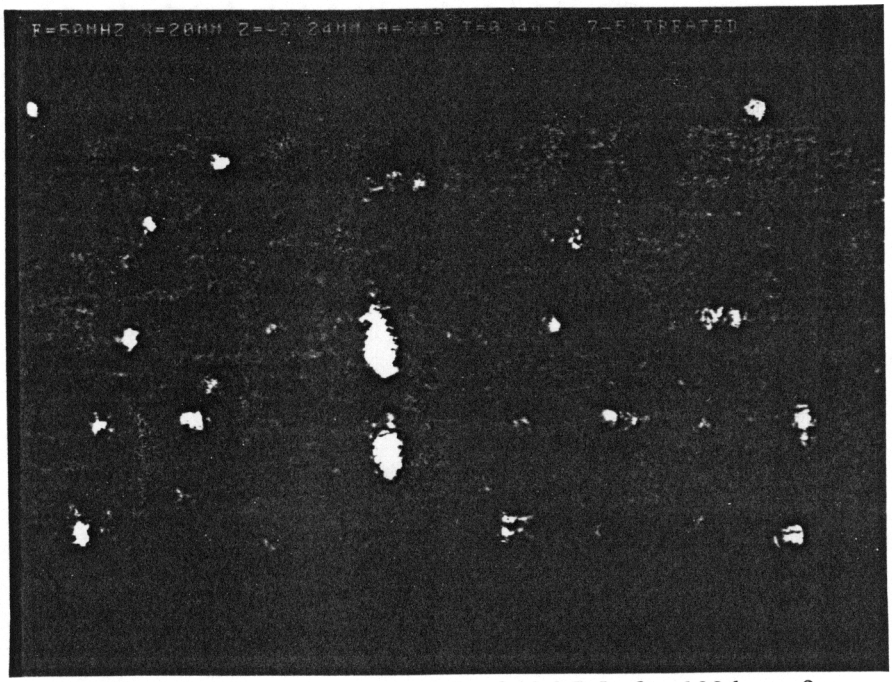

FIGURE 13: Acoustic micrograph of AM-7-5 after 100 hrs. of thermal ageing at 1400 °C. (z = 0 mm, A = 3 dB, T = 0.4 μs)

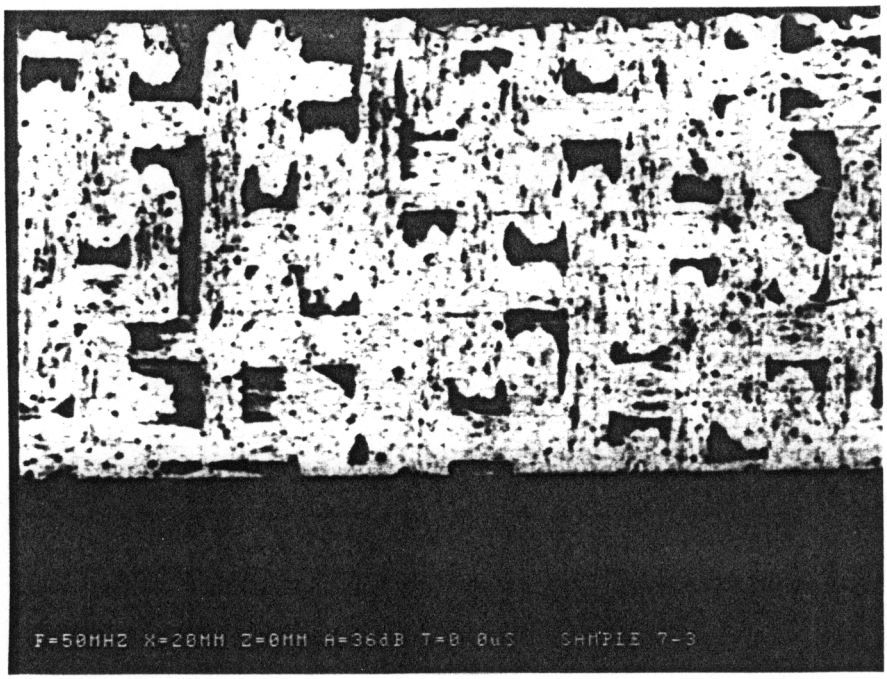

FIGURE 14: Acoustic micrograph of AM-7-3 before heat treatment. (z = 0 mm, A = 36 dB, T = 0 μs)

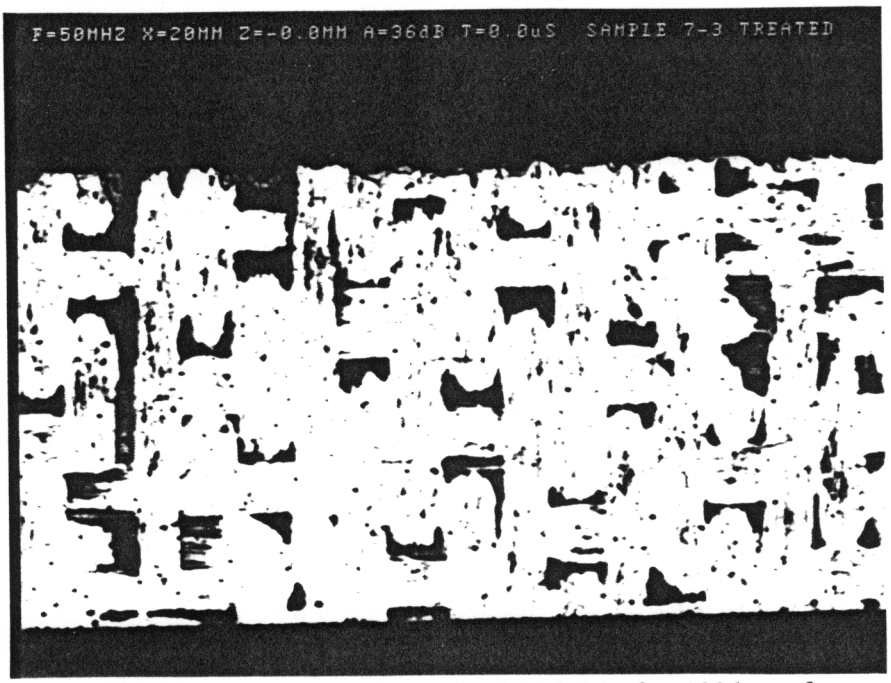

FIGURE 15: Acoustic micrograph of AM-7-3 after 100 hrs. of thermal ageing at 1200 °C. (z = 0 mm, A = 36 dB, T = 0 μs)

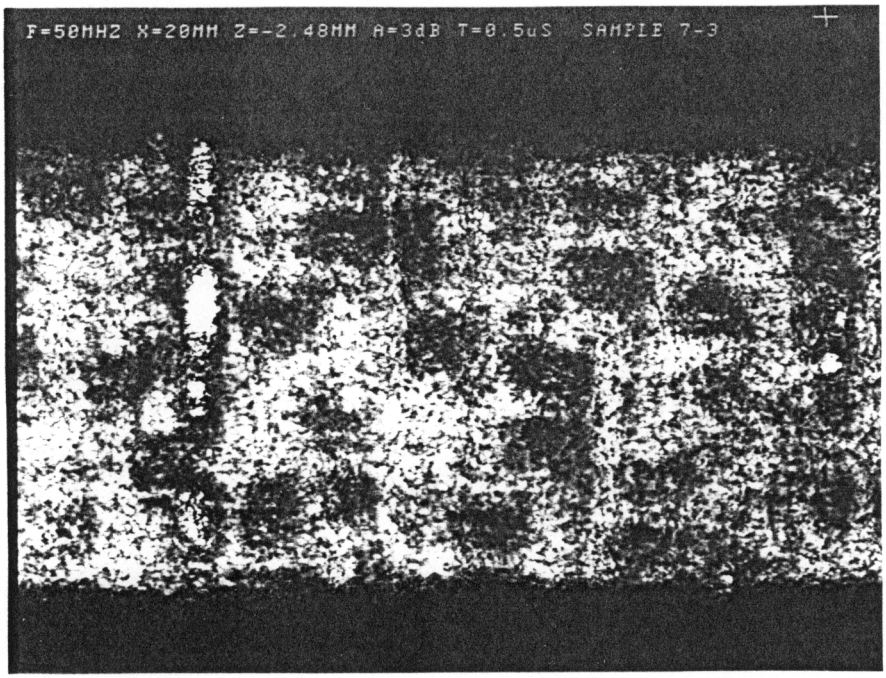

FIGURE 16: Acoustic micrograph of AM-7-3 before heat treatment. (z = -2.48 mm, A = 3 dB, T = 0.5 μs)

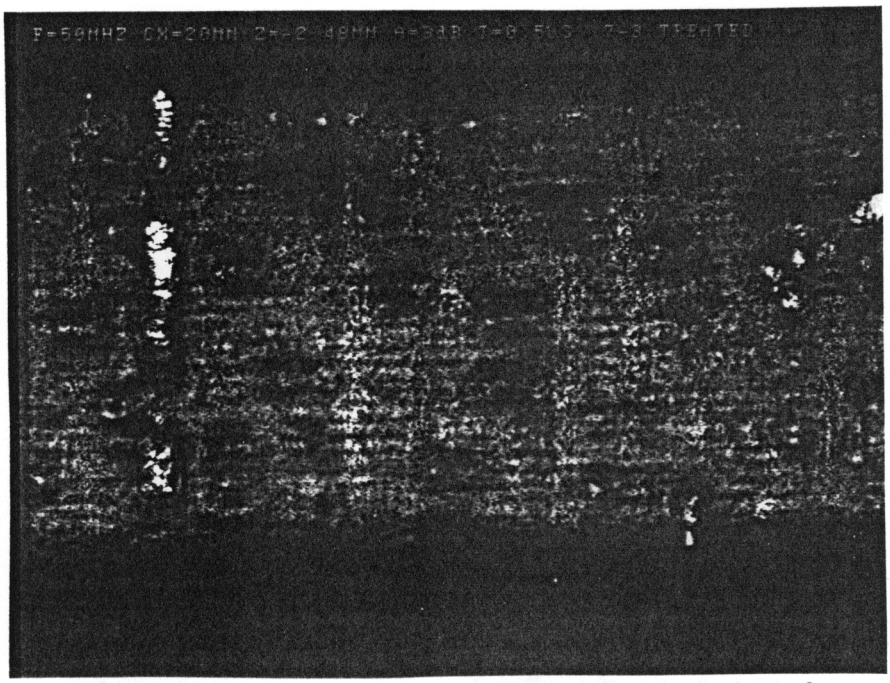

FIGURE 17: Acoustic micrograph of AM-7-3 after 100 hrs. of thermal ageing at 1200 °C. (z = -2.48 mm, A = 3 dB, T = 0.5 μs)

FIGURE 18: Acoustic micrograph of AM-1-5 after 100 hrs. of thermal ageing at 1400 °C (z = 0 mm, A = 36 dB, T = 0 μs)

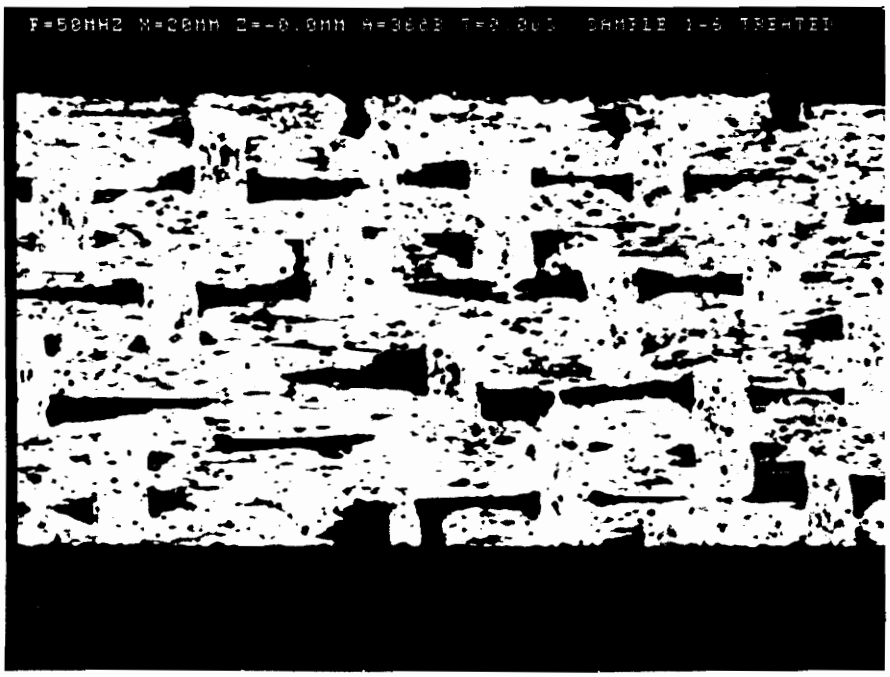

FIGURE 19: Acoustic micrograph of AM-1-6 after 100 hrs. of thermal ageing at 1200 °C. (z = 0 mm, A = 36 dB, T = 0 μs)

AU Results

The raw data from the acousto-ultrasonic analysis are provided in **Appendix C**, along with the results from the statistical analysis (paired difference-in-means test). The AU parameter used in this investigation is one of three parameters which can be used to describe a distribution function [82]. The three parameters describe location, size, and shape. The size parameter M_0 (zeroth moment), the area under the power spectral density curve, was the focus of this investigation. The paired difference-in-means test was used to eliminate random variation across specimen positions in order to determine if the results from as-fabricated and heat-treated specimens were statistically different.

The results from the AU analysis are shown in **Figures 20-29**. (Note: The plotted values of M_0 were normalized by substracting the average of ten trial measurements made at position 3 on reference AM-7-2. The ten trial measurements are provided in **Appendix C**.) The results from the specimens that were heat-treated at 1000 °C are shown in **Figures 20-23**. As seen in **Figures 20** and **21**, the coated specimen AM-8-1 attenuates acoustic signals more strongly after it has been heat treated. In contrast, the uncoated specimens AM-1-7 **(Figure 22)** and AM-2-1 **(Figure 23)** do not attenuate the acoustic signals as well after they have been heat treated. However, the ends of specimens AM-1-7 and AM-2-1 are exceptions; the AU signals measured at the ends of the specimens (represented by positions 1 and 5) are weaker. These low amplitude signals may be caused by the close proximity of material boundaries or by material-property gradients existing between the external surfaces and bulk of the heat-treated specimens.

According to the results of the paired difference-in-means test, the trends observed in the graphs of the AU results from specimens AM-8-1, AM-1-7, and AM-2-1 are due to heat treatment rather

than random variation. The test results proved that there is a statistical difference between the mean M_0 of the as-fabricated specimens and the mean M_0 of the specimens heat-treated at 1000 °C.

There appears to be a correlation between the AU results and the findings of the thermogravimetric analysis. Referring to the thermogravimetric results, AM-8-1 gained mass after being heat treated, while AM-1-7 and AM-2-1 lost mass. The discrepancy between the AU results for the coated and uncoated specimens are attributed to the same chemical changes that were responsible for the mass discrepancies.

The exact nature of the chemical changes occurring in the two uncoated specimens, AM-1-7 and AM-2-1, were not studied in this investigation and can only be theorized at this time. Several chemical reactions including pyrolysis, oxidation, and reduction may occur simultaneously during heat treatment. However, for a given temperature and thermal exposure time, one reaction may be dominant. Because mass loss was reported only for the two uncoated specimens heat treated at 1000 °C, pyrolysis of the fiber sizing is believed to be the dominant reaction. The chemical changes occurring as a function of this pyrolysis are believed to be responsible for the increased amplitude of the acoustic signals.

The AU results from AM-8-1 correspond to the results of the specimens heat treated at 1200 °C seen in **Figures 24-26**. According to the graphs, coated specimens AM-7-3 **(Figure 24)** and AM-7-4 **(Figure 25)** and uncoated specimen AM-1-6 **(Figure 26)** attenuate acoustic signals more strongly after they have been heat treated at 1200 °C. This observed increase in attenuation may be attributed to microstructural changes occurring in the matrix, interfacial region, and fibers. As

the matrix and fibers are oxidized, silica rings form around the fibers and CO and SiO are lost; thermal exposure causes the nearly amorphous fibers to become more crystalline and promotes grain growth. These microstructural changes increase the composite's ability to scatter ultrasonic energy. Thus, the increased ultrasonic attenuation of the CMC may be attributed to a combination of Rayleigh ($\lambda >>$ size of critical element), stochastic ($\lambda \approx$ size of critical element), and diffusive scattering ($\lambda <<$ size of critical element), rather than a single dominant scattering mechanism [83].

According to the results of the paired difference-in-means test, the trends observed in the graphs of the AU results from specimens AM-7-3, AM-7-4, and AM-1-6 are due to heat treatment rather than random variation. The test results proved that there is a statistical difference between the mean M_0 of the as-fabricated specimens and the mean M_0 of the specimens heat-treated at 1200 °C.

The AU results from the specimens heat treated at 1400 °C are shown in **Figures 27-29**. Contrary to expectation, the AU results from these specimens do not follow the same trend observed in the results from specimens heat treated at 1200 °C. In fact, the AU results from coated specimens AM-7-5 and AM-7-6 and uncoated specimen AM-1-5 do not appear to follow a trend. According to the results of the paired difference-in-means test, there is no statistical difference between the mean M_0 of the as-fabricated specimens and the mean M_0 of the heat-treated specimens.

IMPORTANT NOTE: Although the aforementioned AU results appear to follow statistically supported trends and correlate well with the other test results, there is also reason to believe that the experimental method may have yielded erroneous data. Referring to the trial measurements made at position 3 on reference specimen AM-7-2 which appear in **APPENDIX C**, there is some

variation among the measurements made during a single day (setup); however, there is excessive variation among the measurements made on different days. The measurements made during the summer months are quite different from the measurements made during the late fall and winter months. Since AM-7-2 was a "reference" or "control" specimen, these measurements should be relatively close. Because the same equipment and procedures were used to perform the AU tests and the same person made the AU measurements, the only apparent variable is the ambient conditions. Perhaps differences in the moisture content of the specimens, caused by relative humidity differences, are responsible for these measurement variations. Additional work is needed to understand these results.

At least two additional investigations will be needed to determine the cause of the drastic variations. One investigation must be directed at the effects of ambient temperature, and humidity. Another investigation must be directed at the ability of the polymeric material to effectively couple the transducers and rough ceramic matrix composite.

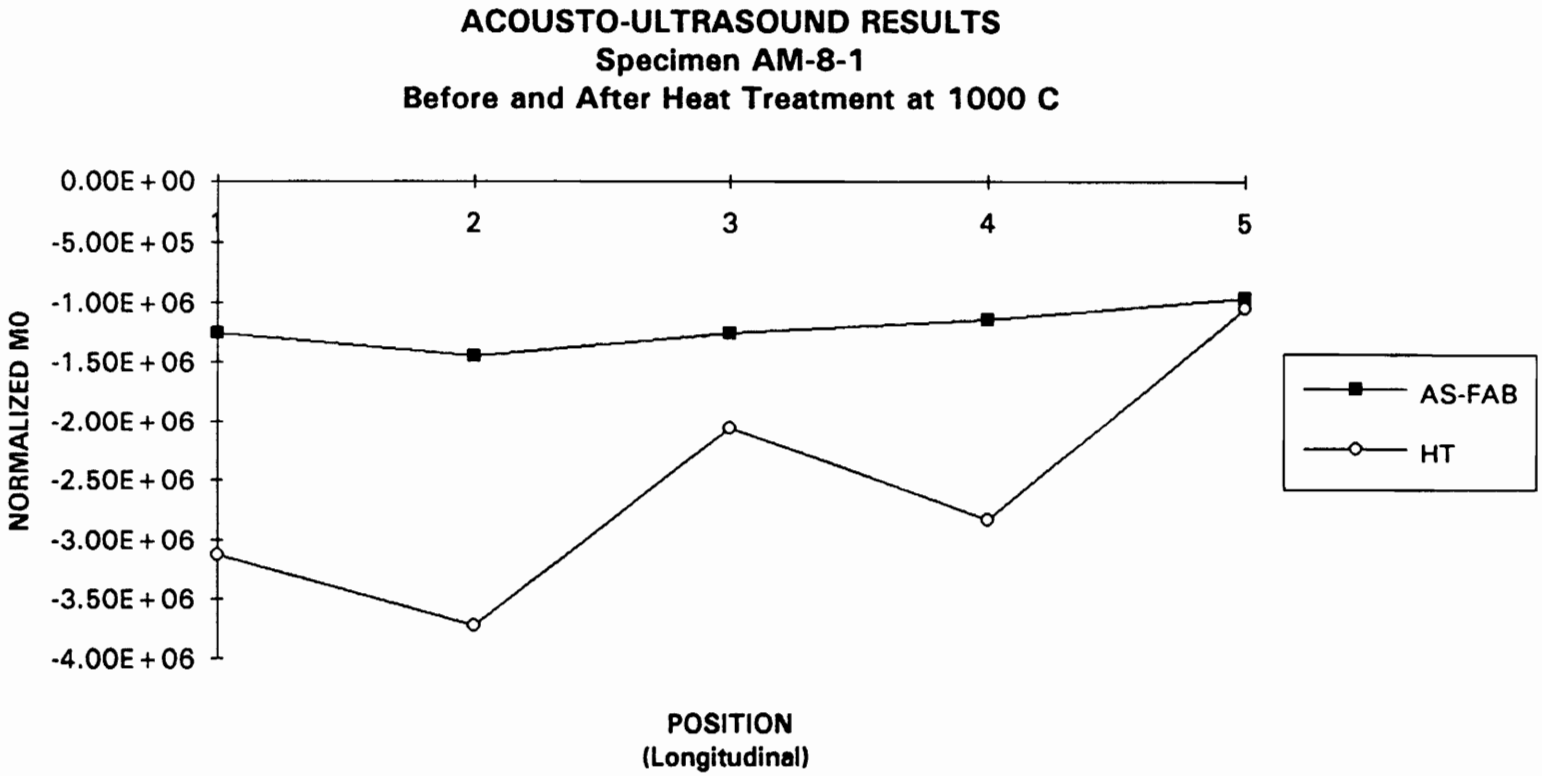

FIGURE 20: Normalized AU parameter M_0 vs. Longitudinal Position, specimen AM-8-1 before and after heat treatment at 1000 °C.

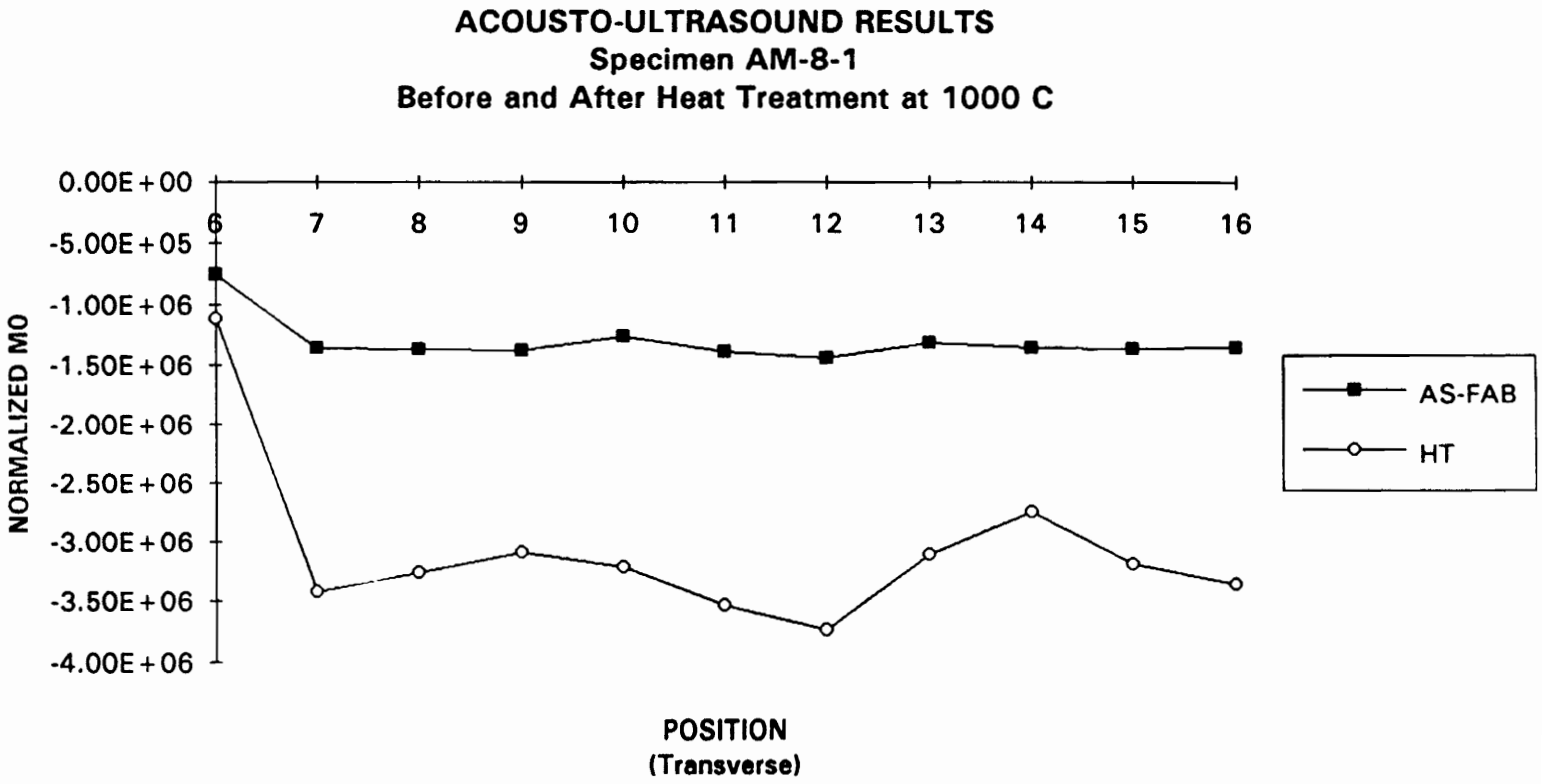

FIGURE 21: Normalized AU parameter M_0 vs. Transverse Position, specimen AM-8-1 before and after heat treatment at 1000 °C.

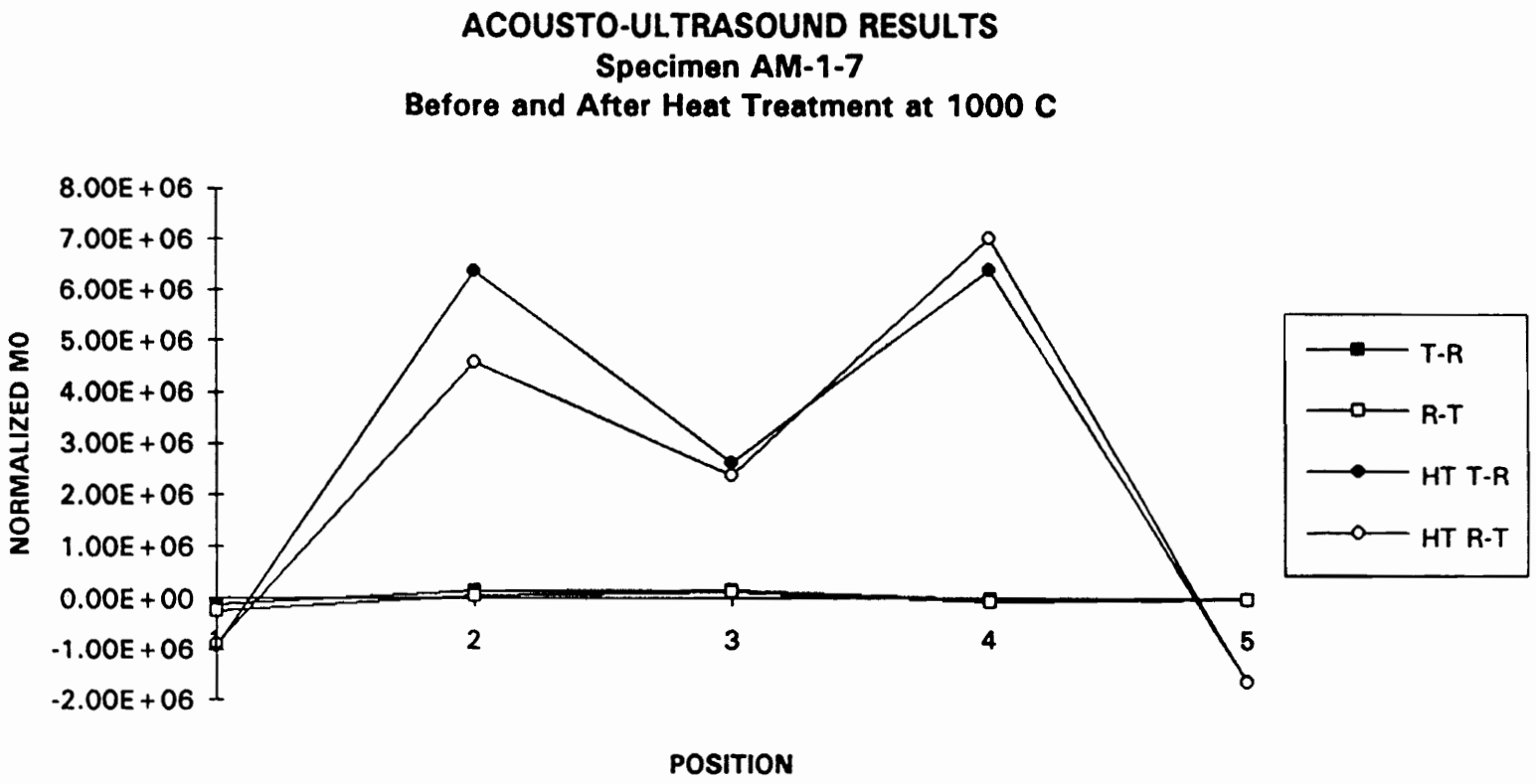

FIGURE 22: Normalized AU parameter M_0 vs. Longitudinal Position, specimen AM-1-7 before and after heat treatment at 1000 °C.

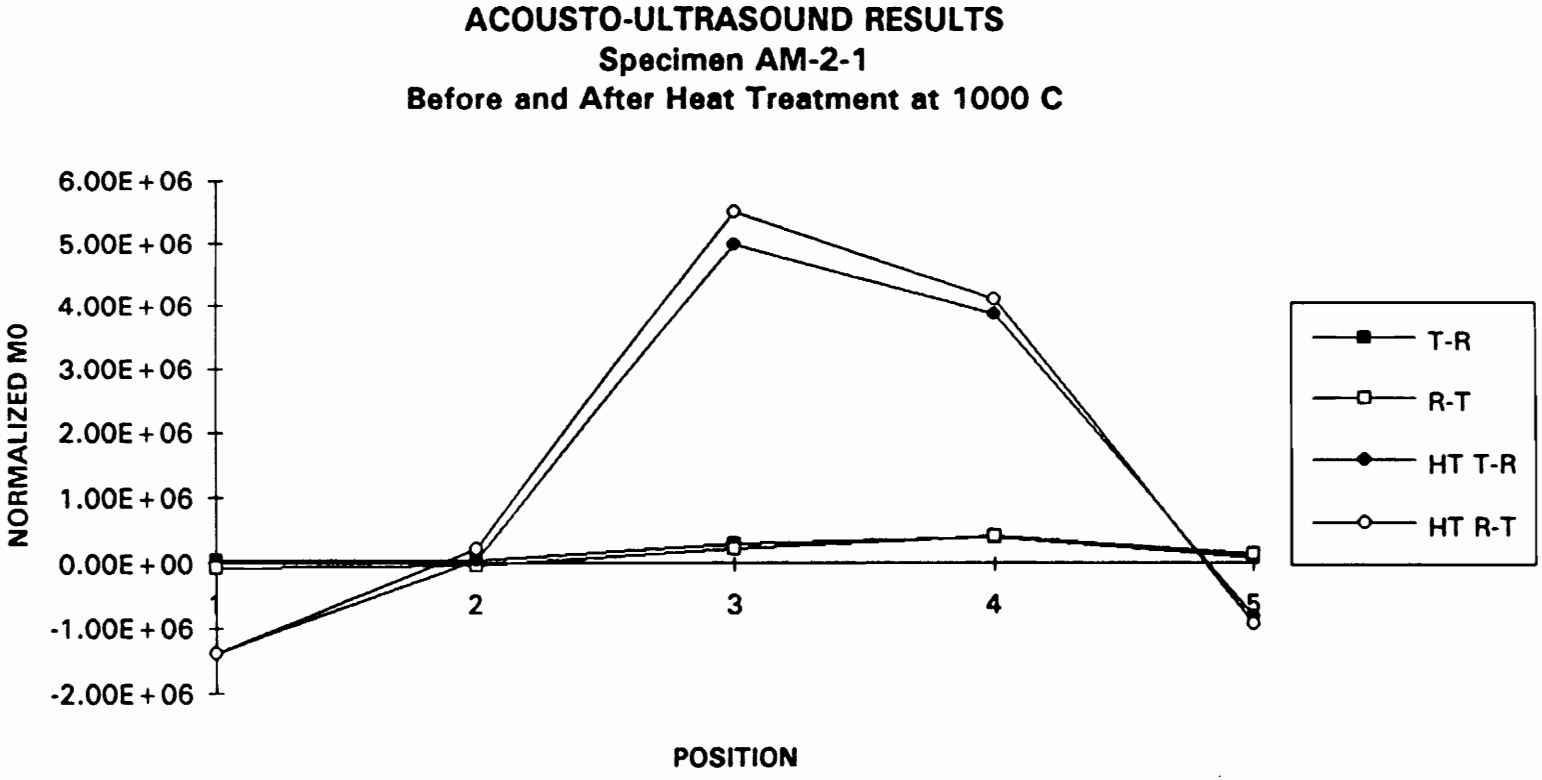

FIGURE 23: Normalized AU parameter M_0 vs. Longitudinal Position, specimen AM-2-1 before and after heat treatment at 1000 °C.

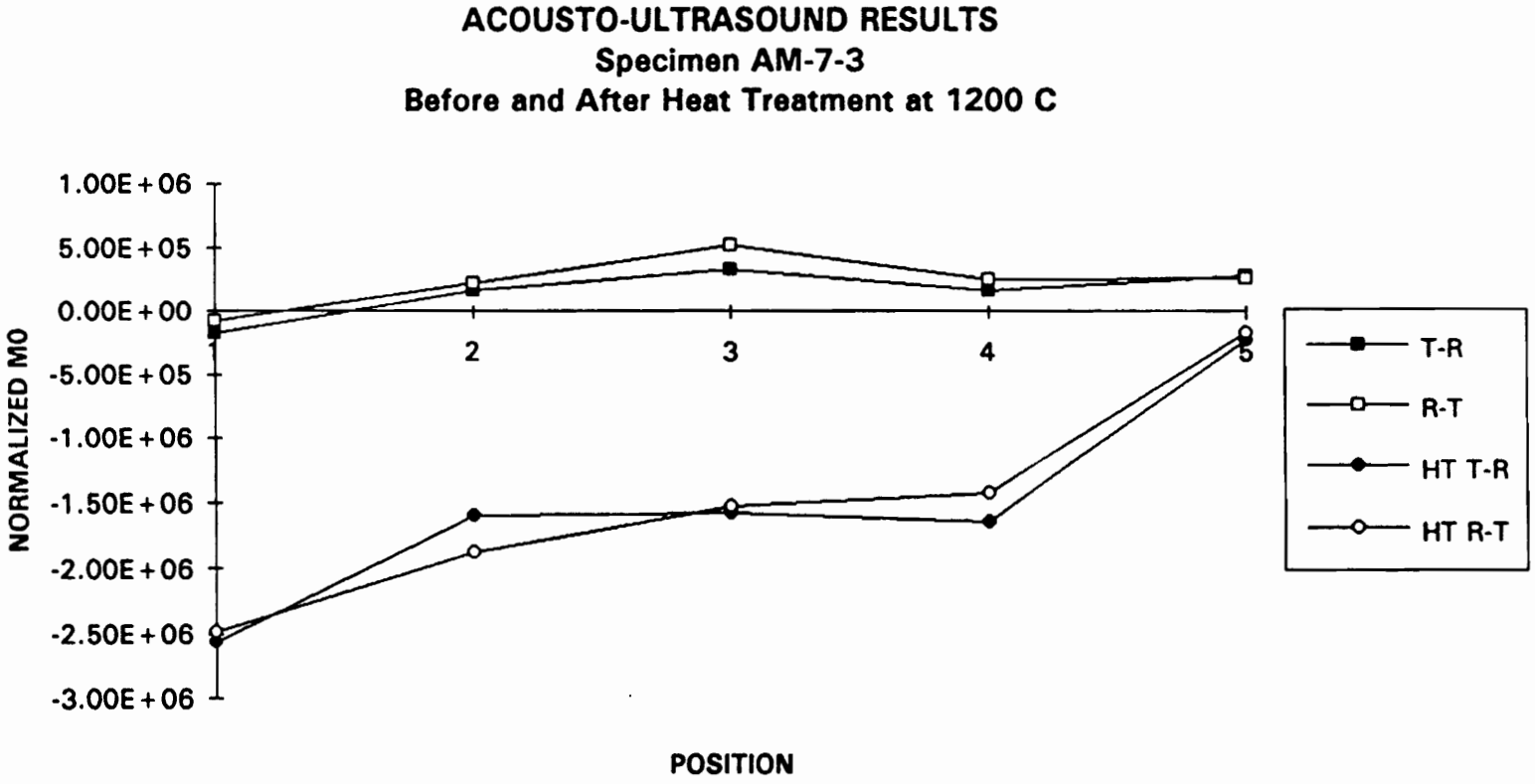

FIGURE 24: Normalized AU parameter M_0 vs. Longitudinal Position, specimen AM-7-3 before and after heat treatment at 1200 °C.

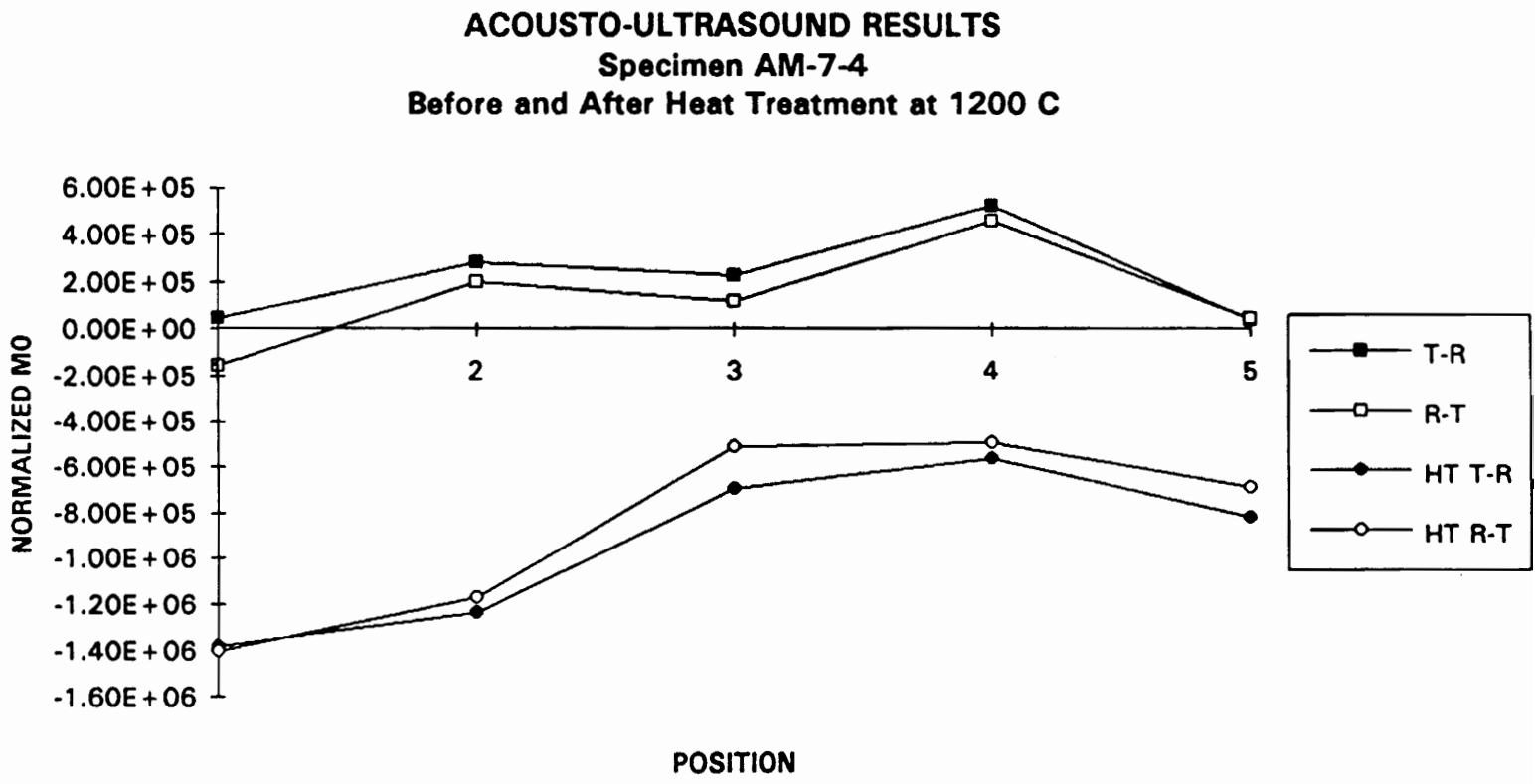

FIGURE 25: Normalized AU parameter M_0 vs. Longitudinal Position, specimen AM-7-4 before and after heat treatment at 1200 °C.

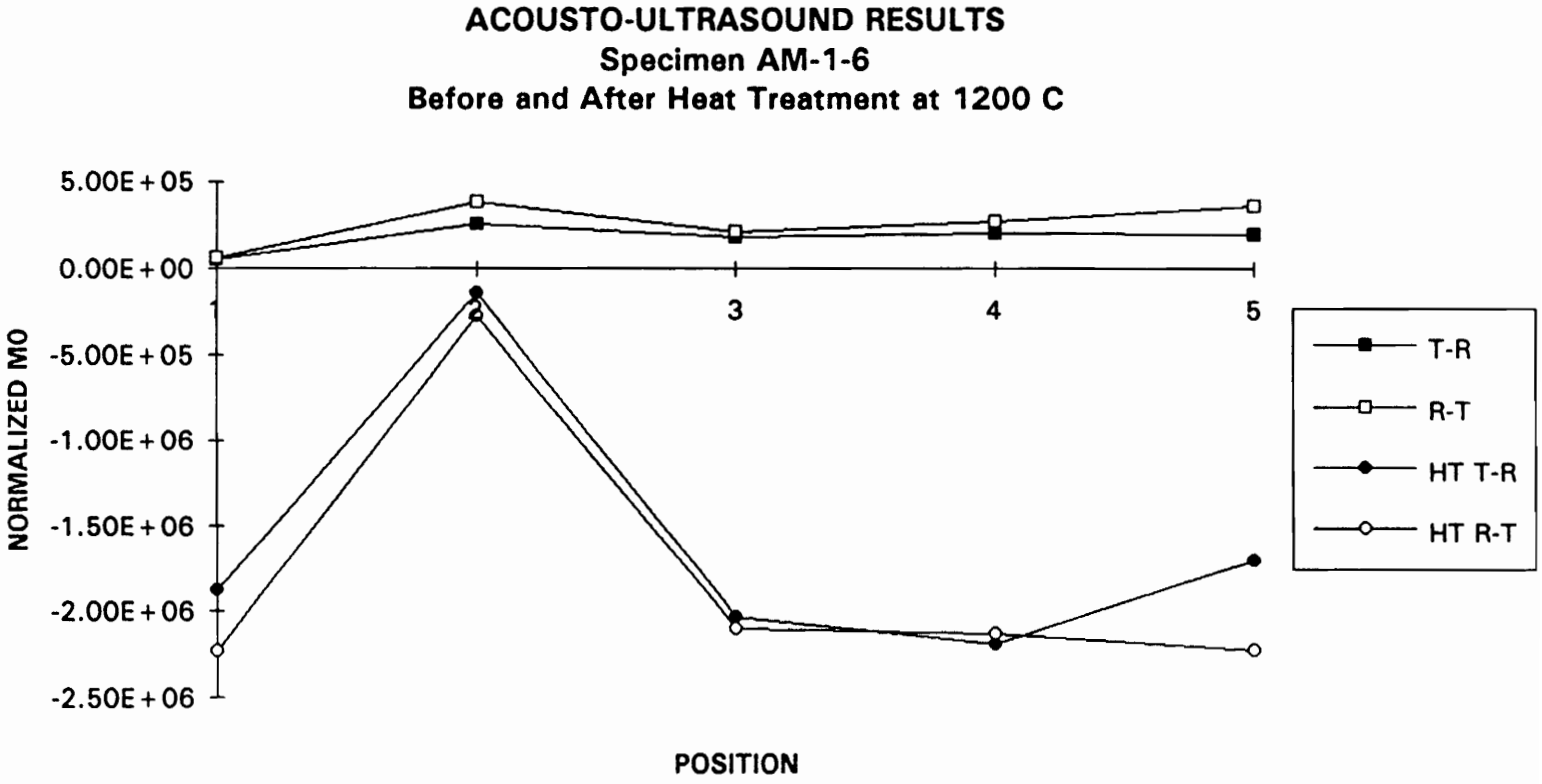

FIGURE 26: Normalized AU parameter M_0 vs. Longitudinal Position, specimen AM-1-6 before and after heat treatment at 1200 °C.

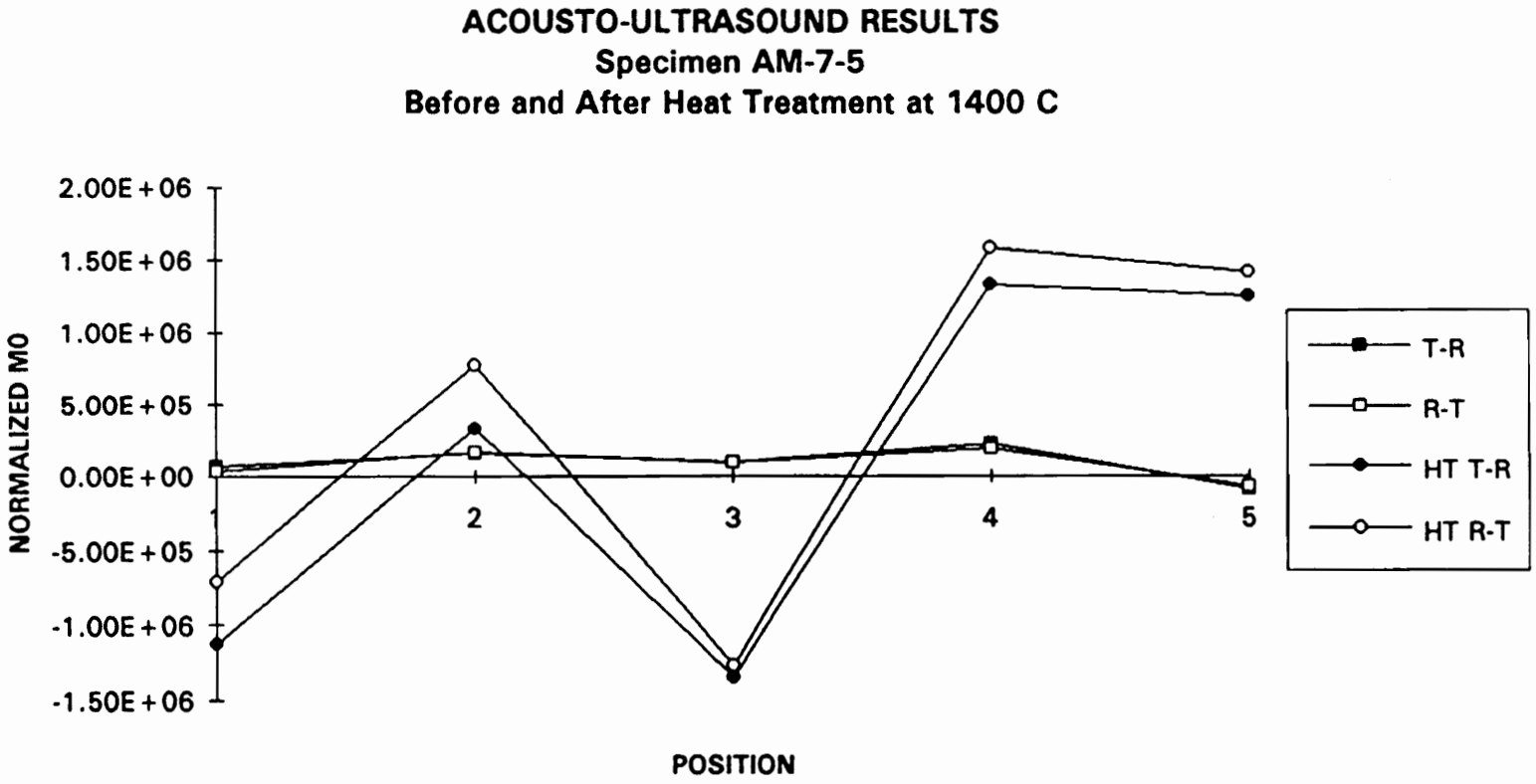

FIGURE 27: Normalized AU parameter M_0 vs. Longitudinal Position, specimen AM-7-5 before and after heat treatment at 1400 °C.

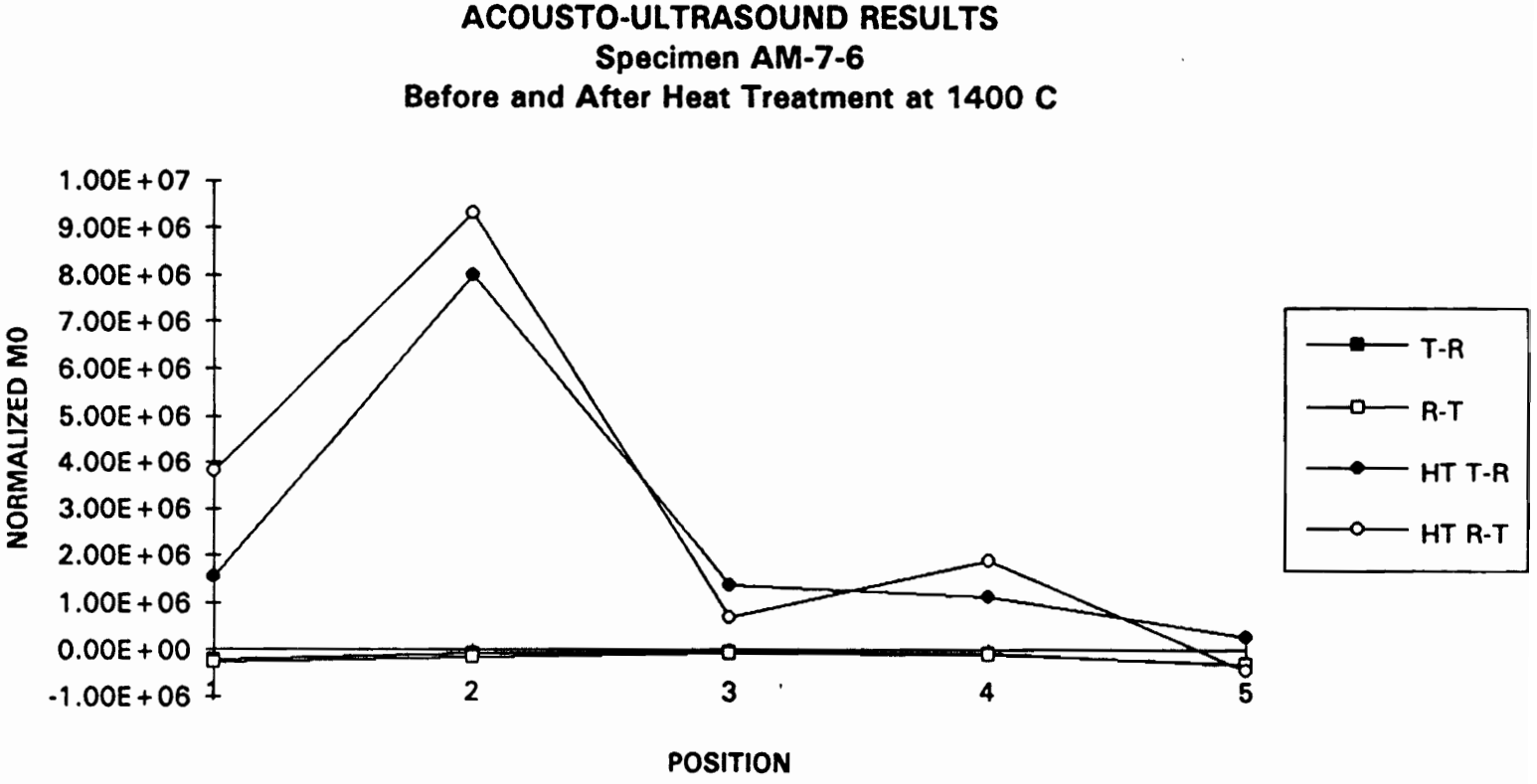

FIGURE 28: Normalized AU parameter M_0 vs. Longitudinal Position, specimen AM-7-6 before and after heat treatment at 1400 °C.

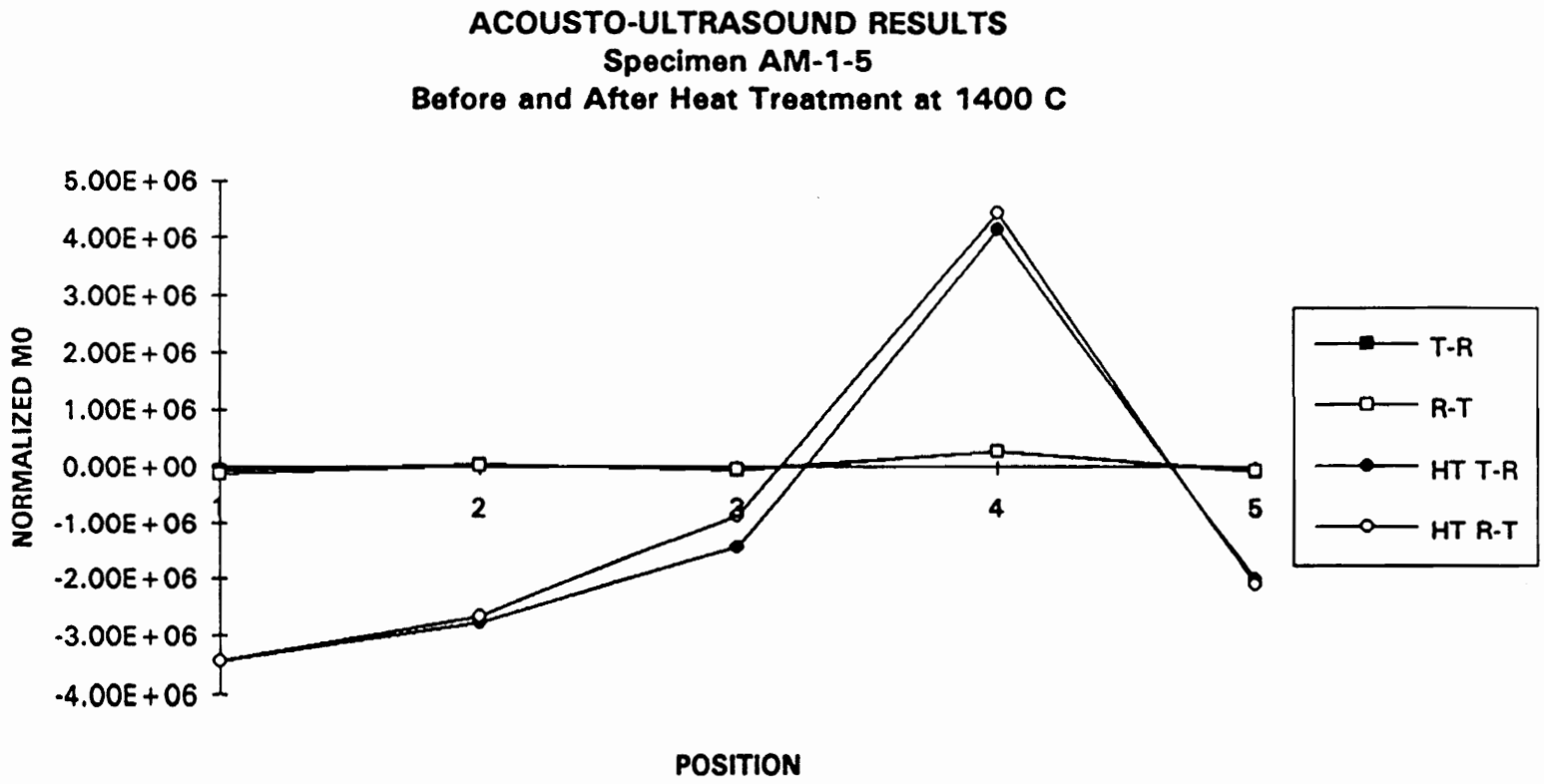

FIGURE 29: Normalized AU parameter M_0 vs. Longitudinal Position, specimen AM-1-5 before and after heat treatment at 1400 °C.

Radiographs

In their as-fabricated condition, the coated specimens exhibited greater X-ray absorption than the uncoated specimens. As seen in **Figures 30-37**, the images of the coated specimens are darker than the images of the uncoated specimens. (Reference specimen AM-7-2 which appears in all of the radiographs may be used as a standard for comparison.) This difference in contrast between the as-fabricated, coated and uncoated specimens agrees with the findings of the thermogravimetric analysis. The coated specimens were an average of 0.01" thicker than the uncoated specimens. Accordingly, the mass of the coated specimens was an average of 1.2 g greater than the mass of the uncoated specimens of equal length. Because of these gravimetric differences, the coated specimens attenuated more radiation than the uncoated specimens.

Positive prints from radiographs of the as-fabricated specimens are shown in **Figures 30-34**. In addition to the previously noted absorption difference, there is also a difference in the weave pattern of coated and uncoated specimens. The X-ray images of the coated specimens have a more uniform "checker-board" weave-appearance than the uncoated specimens.

In **Figures 32** and **34**, the images of specimens AM-2-1 and AM-8-1 have distinct patterns of high and low X-ray absorption. In **Figure 32**, the image of uncoated specimen AM-2-1 has circular regions (≈0.25" dia.) of light gray appearing at 1" intervals down its length. In **Figure 34**, the image of coated specimen AM-8-1 has several rows of these circular regions; the rows are 0.5" apart, with every other row staggered so that the circular regions create a checker-board pattern. These circular regions are a function of the fabrication process. During the fabrication process, the composite was sandwiched between two metal plates; these plates were riddled with regularly spaced 0.25" diameter holes. These same patterns appear in the C-scans of specimens AM-2-1 and

AM-8-1 which are included in the next section.

Positive prints from the radiographs of the heat-treated specimens are shown in **Figures 35-37**. Based on the X-ray images, there are no observable changes between the as-fabricated and heat-treated specimens. The areas of high and low X-ray absorption are the same before and after heat treatment. Even the X-ray images of the specimens heat-treated at the highest temperature (1400 °C) which are shown in **Figure 37**, appear the same before and after heat treatment.

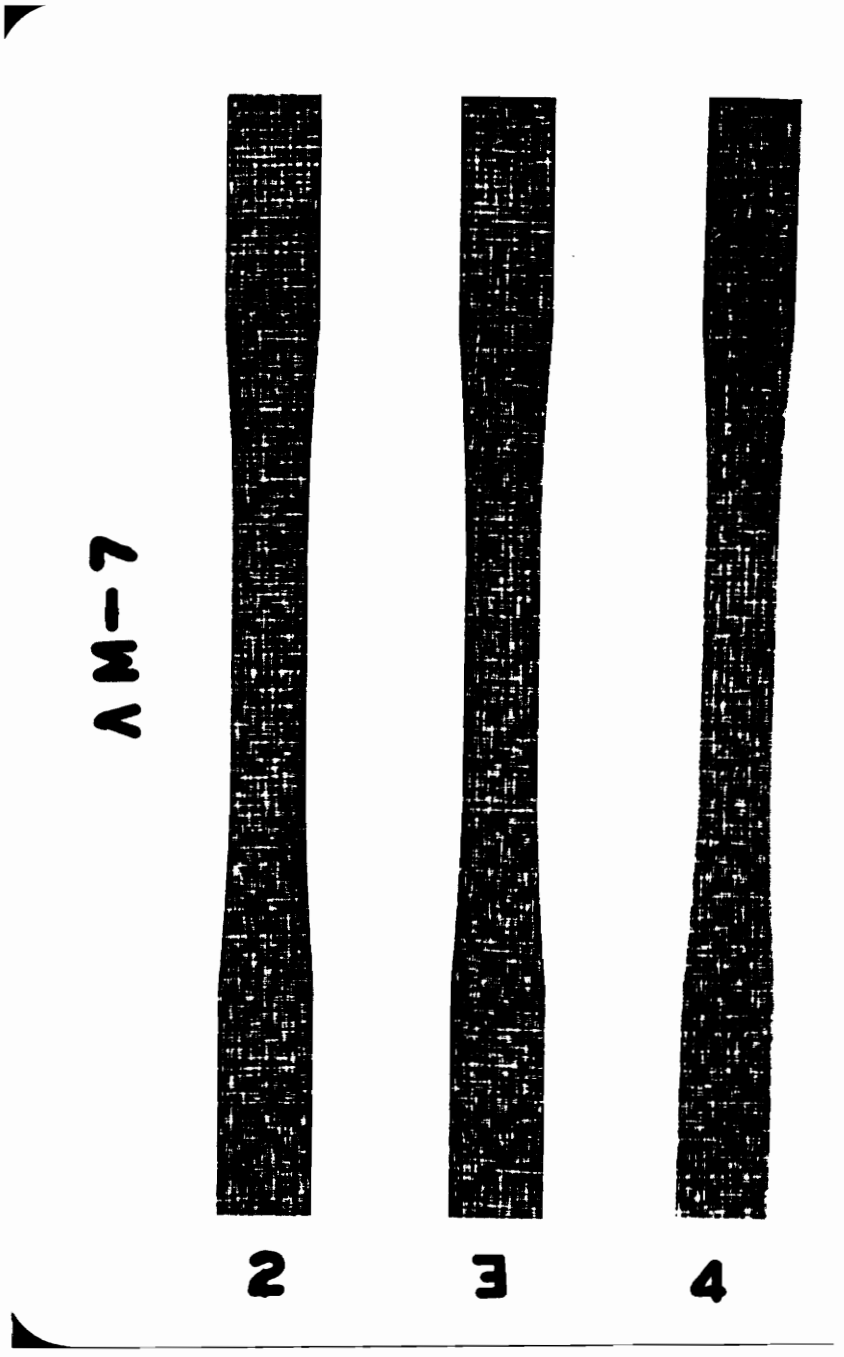

FIGURE 30: Positive print from radiograph of as-fabricated AM-7-2 (coated), AM-7-3 (coated), and AM-7-4 (coated).

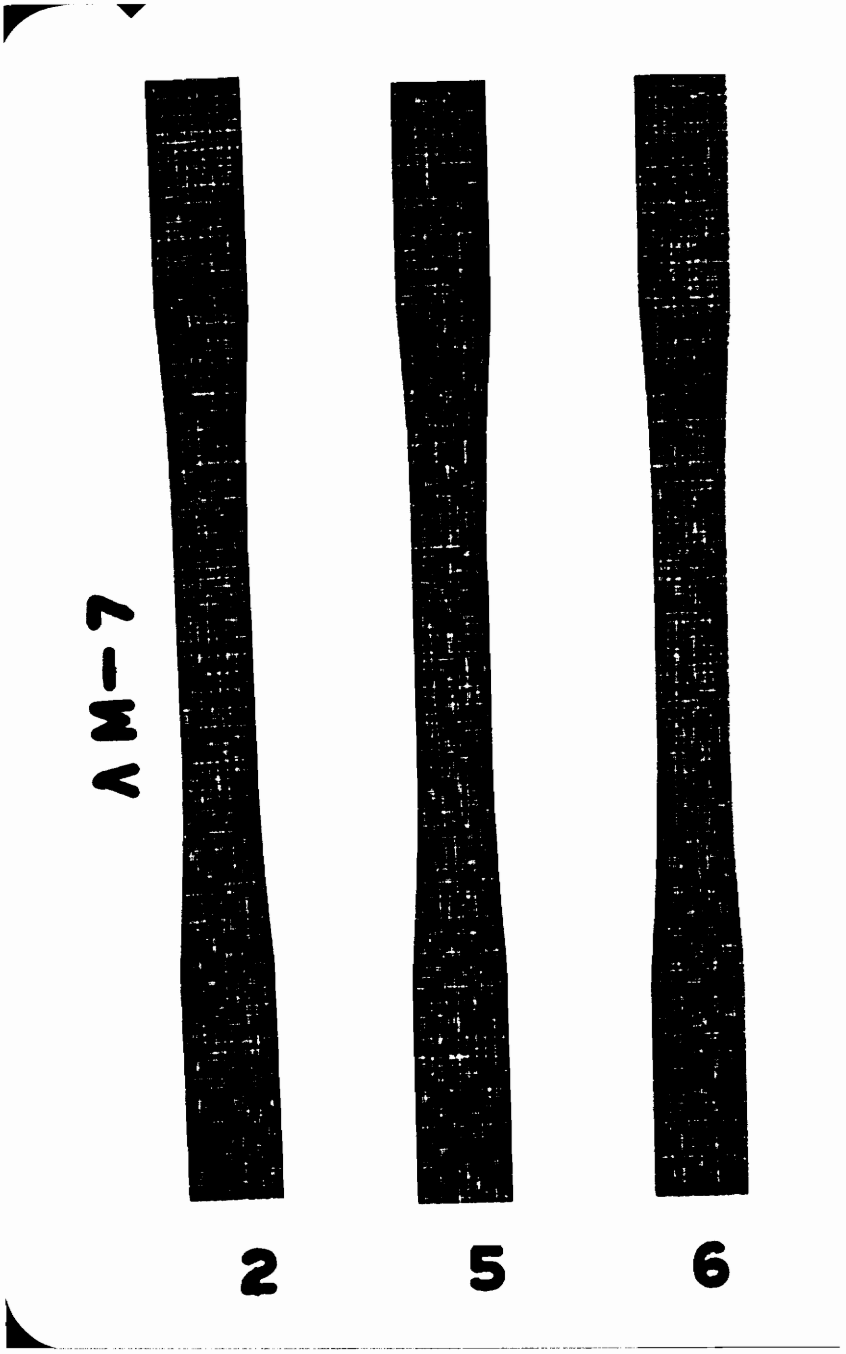

FIGURE 31: Positive print from radiograph of as-fabricated AM-7-2 (coated), AM-7-5 (coated), and AM-7-6 (coated).

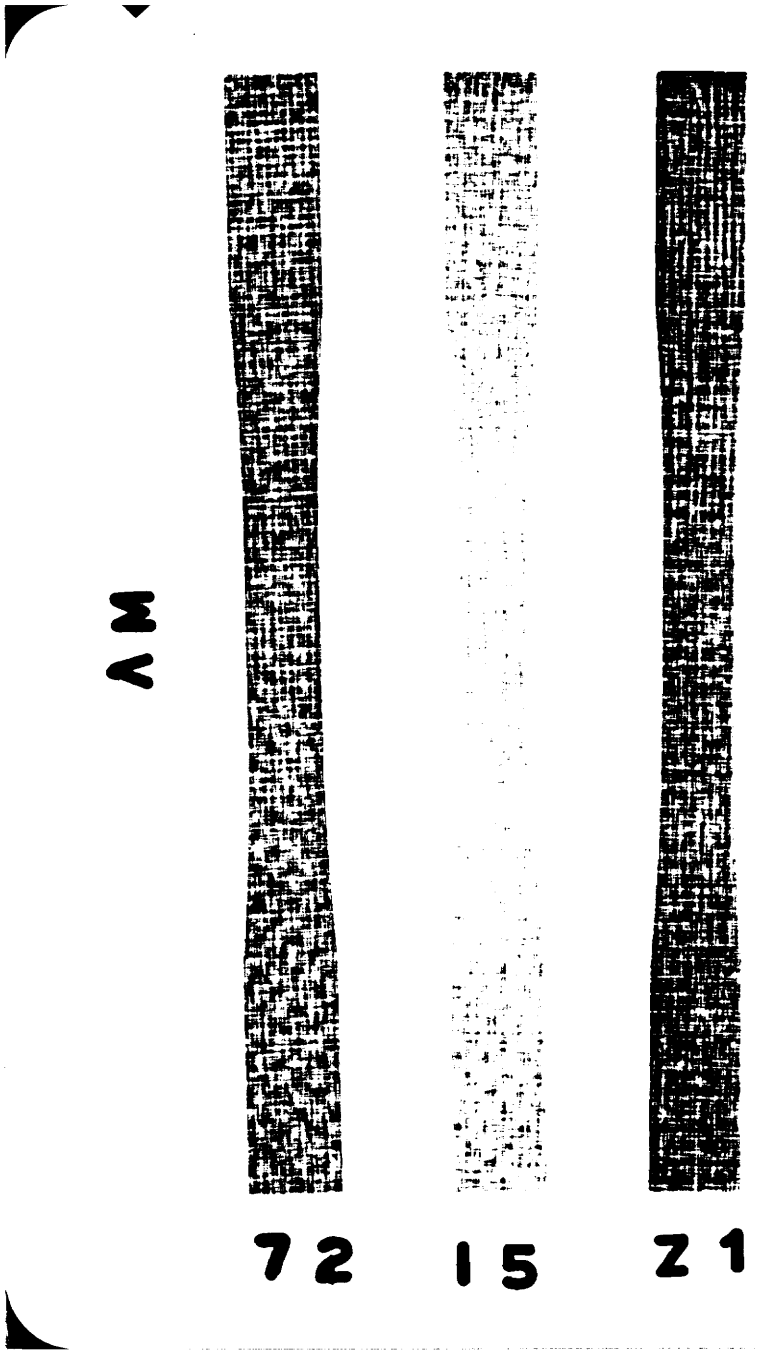

FIGURE 32: Positive print from radiograph of as-fabricated AM-7-2 (coated), AM-1-5 (uncoated), and AM-2-1 (uncoated).

FIGURE 33: Positive print from radiograph of as-fabricated AM-7-2 (coated), AM-1-6 (uncoated), and AM-1-7 (uncoated).

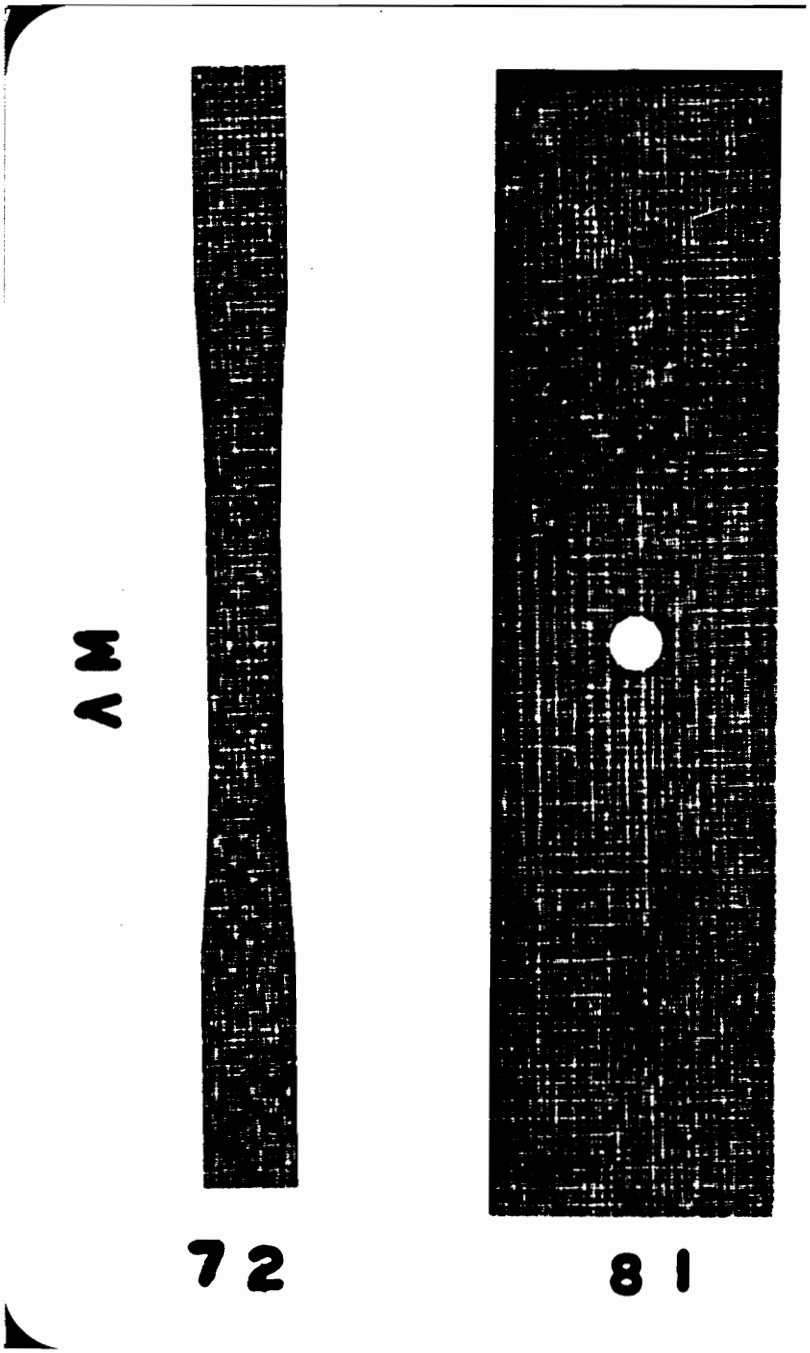

FIGURE 34: Positive print from radiograph of as-fabricated AM-7-2 (coated)and AM-8-1 (coated).

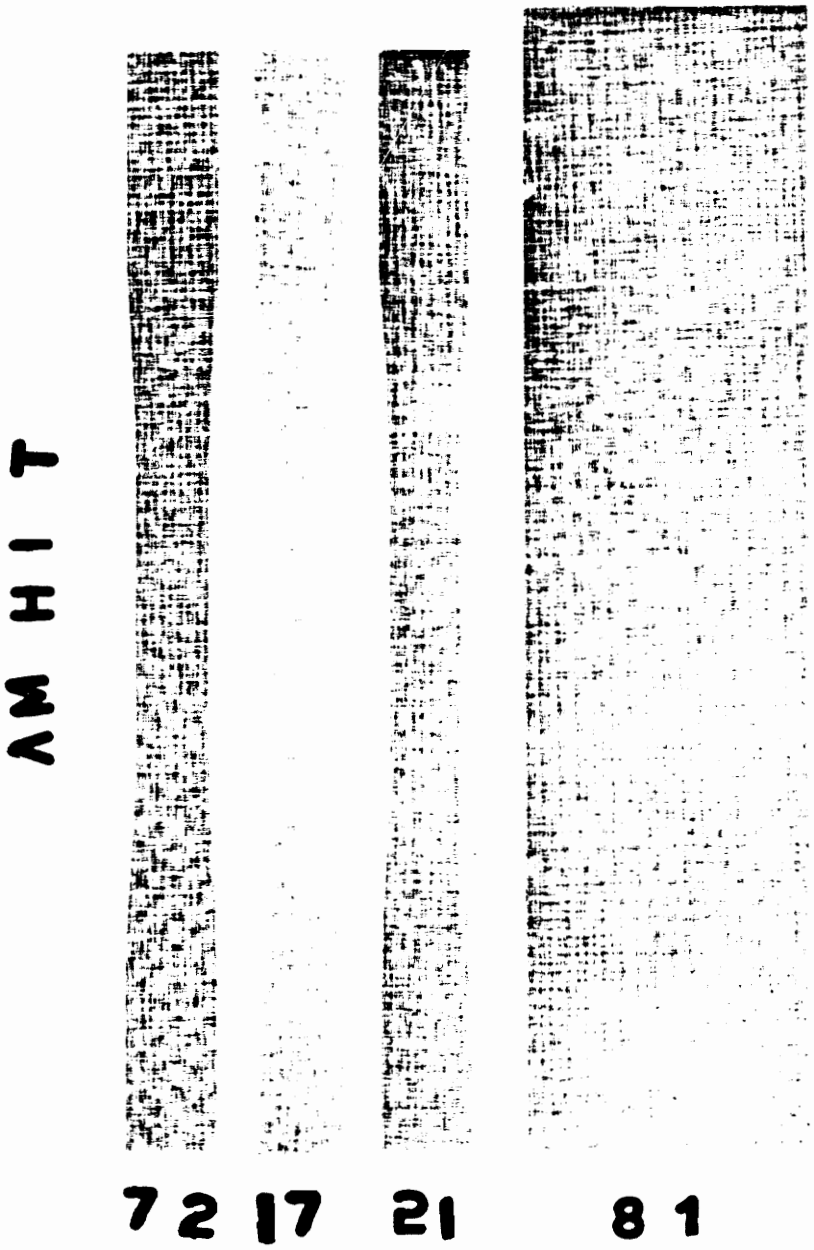

FIGURE 35: Positive print from radiograph of AM-7-2, AM-1-7, AM-2-1, and AM-8-1 after heat treatment at 1000 °C.

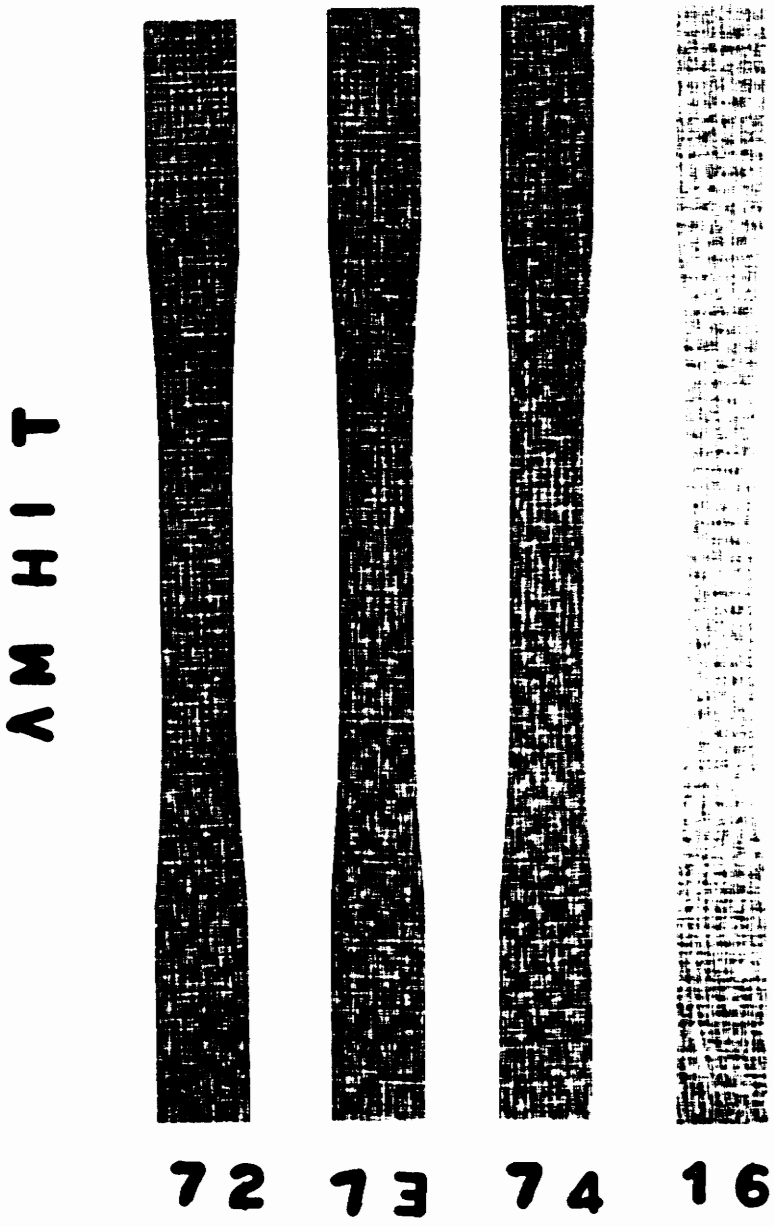

FIGURE 36: Positive print from radiograph of AM-7-2, AM-7-3, AM-7-4, and AM-1-6 after heat treatment at 1200 °C.

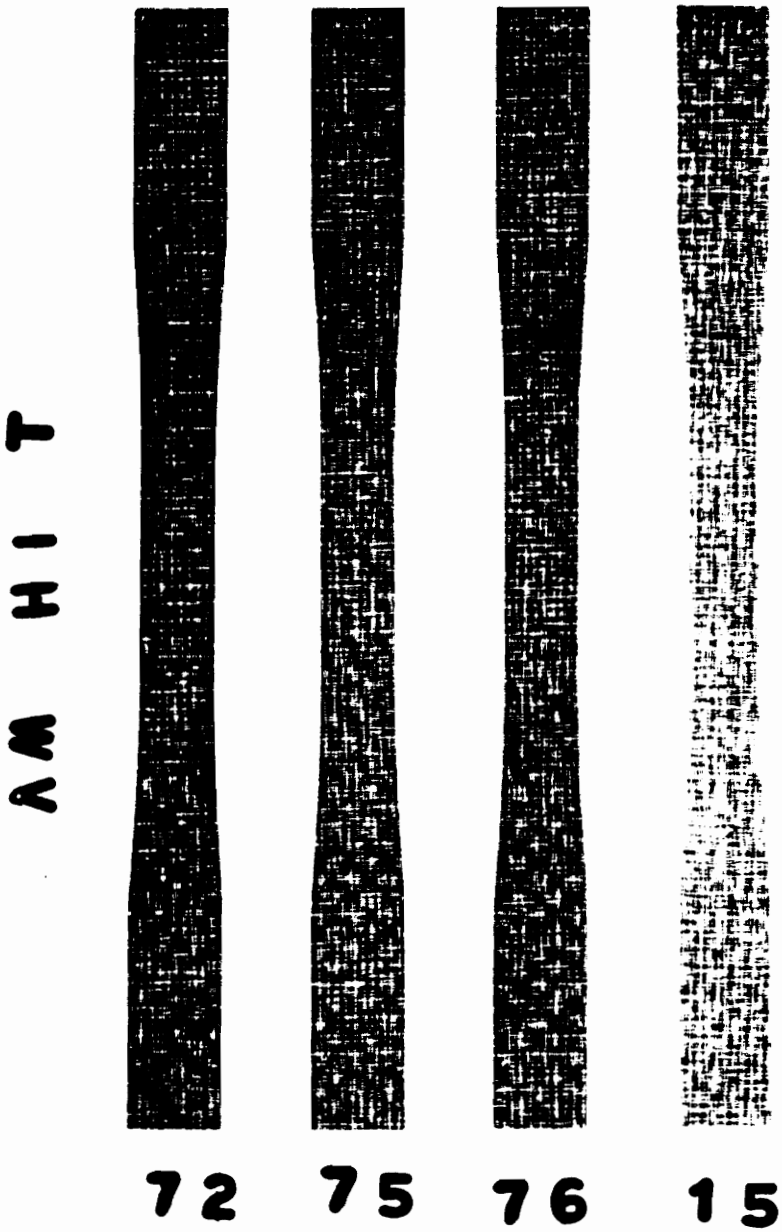

FIGURE 37: Positive print from radiograph of AM-7-2, AM-7-5, AM-7-6, and AM-1-5 after heat treatment at 1400 °C.

Results from Immersion Scan Ultrasonics

The C-scans of the as-fabricated and heat-treated specimens are shown in **Figures 38-43**. Reference specimen AM-7-2 appears in each C-scan (occupying the left-most position) and is to be used to compare and contrast results. It is important to note that the C-scans which are shown in **Figures 38-40** were made during the same 14-hour period. During this time, only the specimens were moved; the setup remained unchanged. The C-scans of the heat treated specimens, shown in **Figures 41-43**, also were made during a single 14-hour period, and again only the specimens were moved.

The C-scans of the as-fabricated specimens are shown in **Figures 38-40**. The coated specimens, AM-7-2, AM-7-3, AM-7-4, AM-7-5, AM-7-6, and AM-8-1, appear to transmit more ultrasonic energy than the uncoated specimens, AM-1-5, AM-1-6, AM-1-7, and AM-2-1. However, the thickest uncoated specimen, AM-2-1, appears to transmit more energy than the other three uncoated specimens. These results are contrary to expectation. As noted in the thermogravimetric analysis, the coated specimens are an average of 0.01" thicker than the uncoated specimens and have approximately the same density. Based on this fact, the coated specimens would be expected to attenuate, rather than transmit, more energy than the uncoated specimens.

The difference between the coated and uncoated specimens may be attributed to the characteristic surface properties of the two groups. The surface of the coated specimens may have minimized impedance mismatch and, thereby, increased the ultrasonic energy that was captured by the surface and transmitted to the bulk of the specimen. In contrast, the smooth and shiny surface finish of the uncoated specimens may have reflected and scattered more ultrasonic energy than the coated specimens. Consequently, the uncoated specimens transmitted less energy because less energy was

available for transmission. A similar phenomenon was previously reported in the discussion of the results from the SAM analysis.

The C-scans of the heat-treated specimens are shown in **Figures 41-43**. According to these results, all of the specimens experienced a change in their ability to transmit ultrasonic energy because of heat treatment. Uncoated specimen AM-1-7 transmits more ultrasonic energy after heat treatment at 1000 °C, while uncoated specimen AM-2-1 attenuates more energy. Overall, coated specimen AM-8-1 appears to transmit more ultrasonic energy after heat treatment. However, a few areas of high transmission prior to heat treatment (the right side and bottom left corner of AM-8-1) appear to transmit less energy after thermal exposure. After heat treatment at 1200 °C, coated specimens AM-7-3 and AM-7-4 attenuate more energy; uncoated specimen AM-1-6 transmits more energy. The same trends are seen in the coated and uncoated specimens after heat treament at 1400 °C. Coated specimens AM-7-5 and AM-7-6 attenuate more energy after heat treatment, while uncoated specimen AM-1-5 transmits more energy.

Based on the C-scan results, two general observations may be made: (1) the ability of coated specimens to attenuate ultrasonic energy increases with increased heat treatment temperature, and (2) the ability of uncoated specimens to attenuate ultrasonic energy decreases slightly with heat treatment. The explanation for these results are two-fold, involving degradation processes and the rate of silica formation.

As proceeding optical micrographs and tensile-test results will show, higher heat-treating temperatures correspond to more extensive degradation on the surface and within the bulk of a specimen. As the CMC degrades, its ability to transmit ultrasonic energy decreases. Oxidation of

the carbonaceous interphase leaves interstitial cavities which reduce energy transmission. The formation of silica around fibers scatters incident ultrasonic signals, further reducing energy transmission. These explanations support the increase in ultrasonic attenuation that was observed in the coated specimens. However, they do not support the slight decrease in ultrasonic attenuation that was observed in the uncoated specimens.

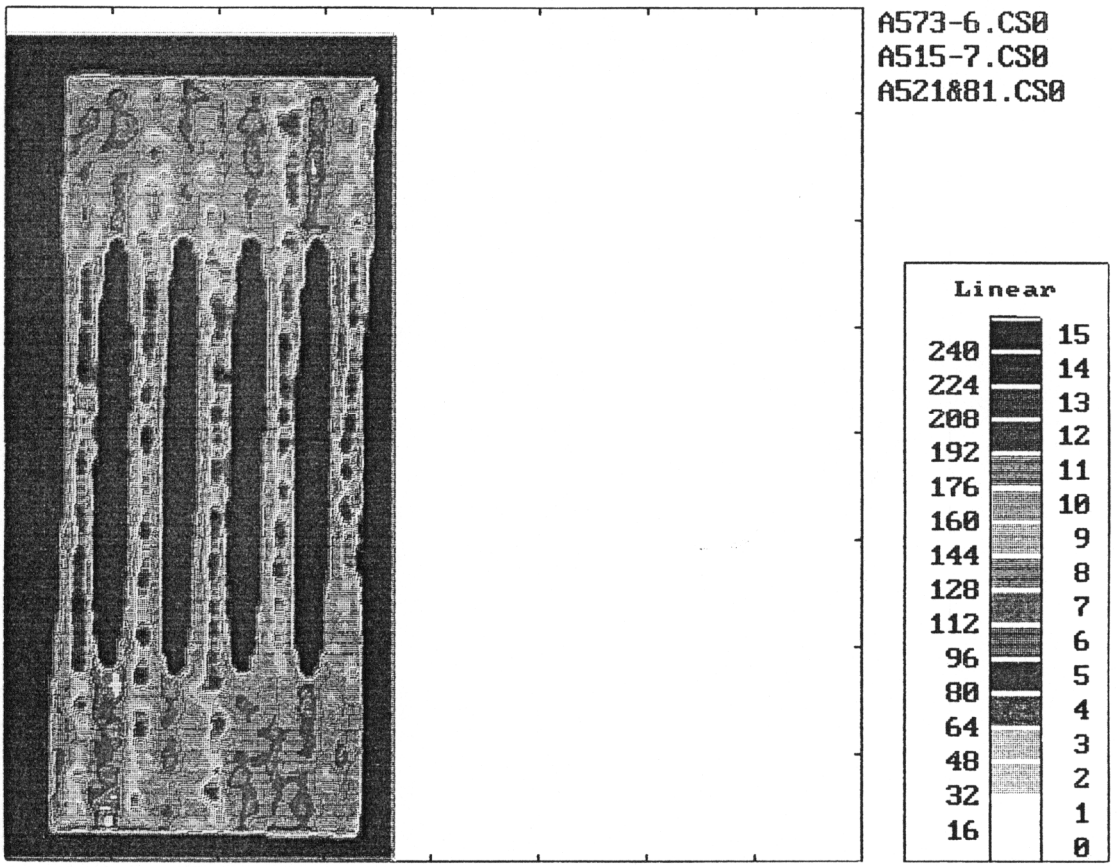

FIGURE 38: C-scan of (left to right) AM-7-2, AM-7-3, AM-7-4, AM-7-5, and AM-7-6 before heat treatment. *Color 0*: Low amplitude signal; *Color 15*: High amplitude signal.

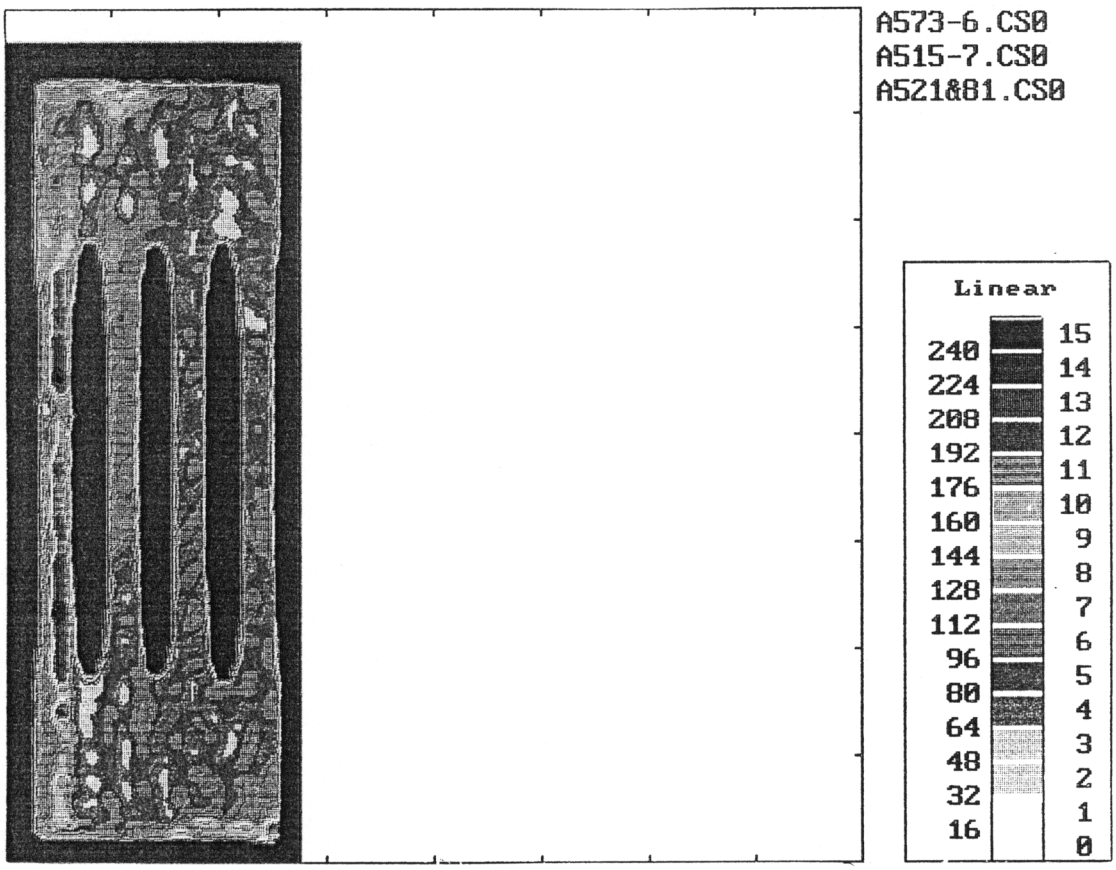

FIGURE 39: C-scan of (left to right) AM-7-2, AM-1-5, AM-1-6, and AM-1-7 before heat treatment. *Color 0*: Low amplitude signal; *Color 15*: High amplitude signal.

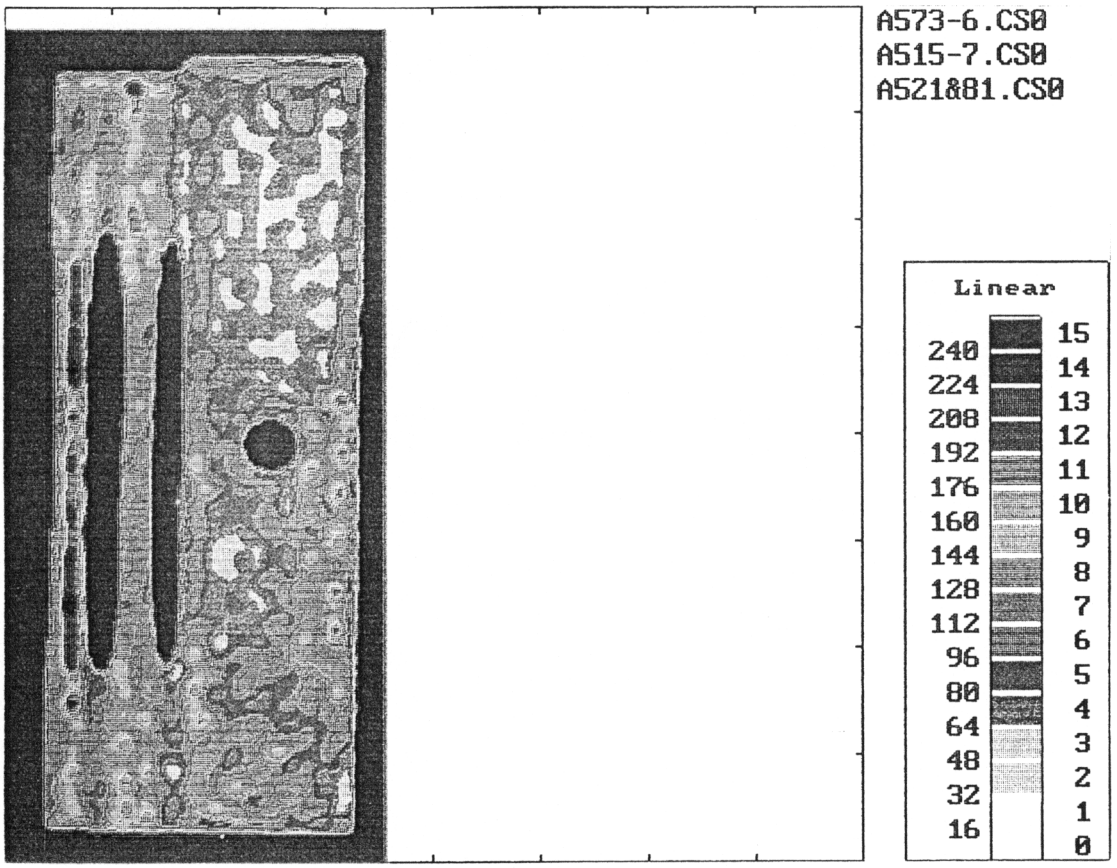

FIGURE 40: C-scan of (left to right) AM-7-2, AM-2-1, and AM-8-1 before heat treatment. *Color 0*: Low amplitude signal; *Color 15*: High amplitude signal.

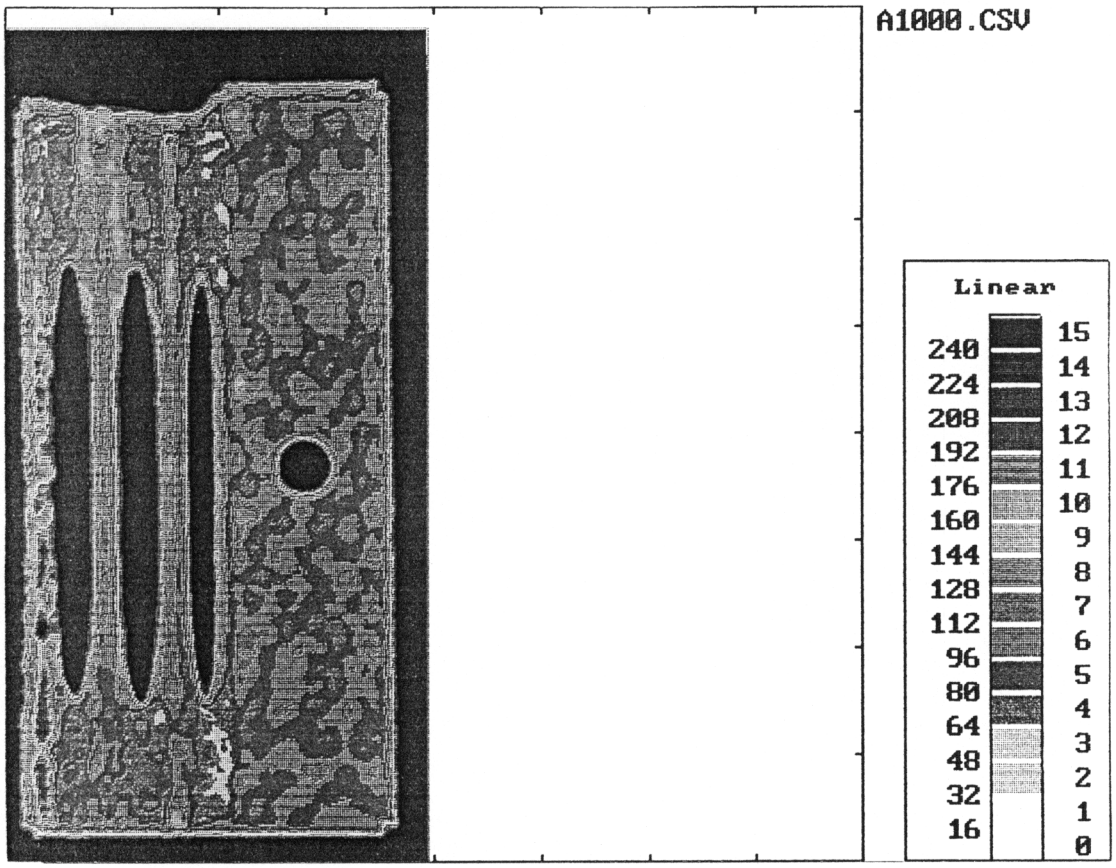

FIGURE 41: C-scan of (left to right) AM-7-2, AM-1-7, AM-2-1, and AM-8-1 after heat treatment at 1000 °C. *Color 0*: Low amplitude signal; *Color 15*: High amplitude signal.

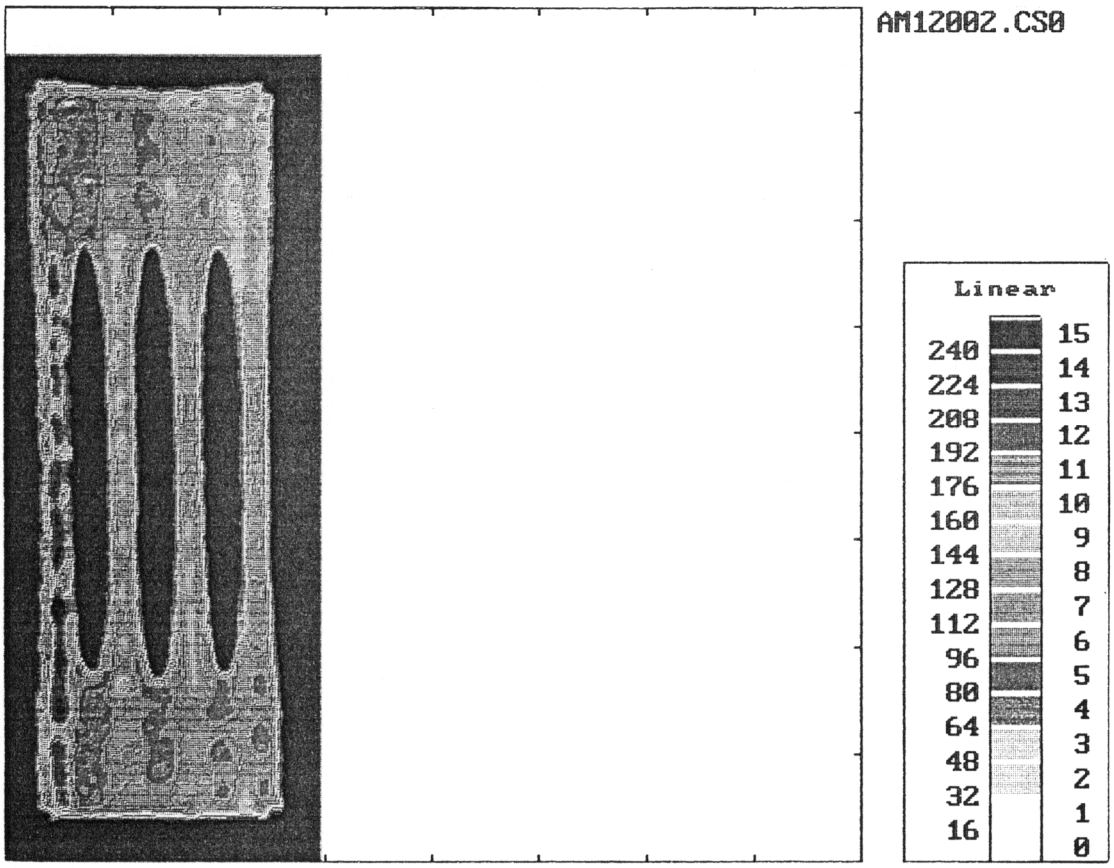

FIGURE 42: C-scan of (left to right) AM-7-2, AM-7-3, AM-7-4, and AM-1-6 after heat treatment at 1200 °C. *Color 0*: Low amplitude signal; *Color 15*: High amplitude signal.

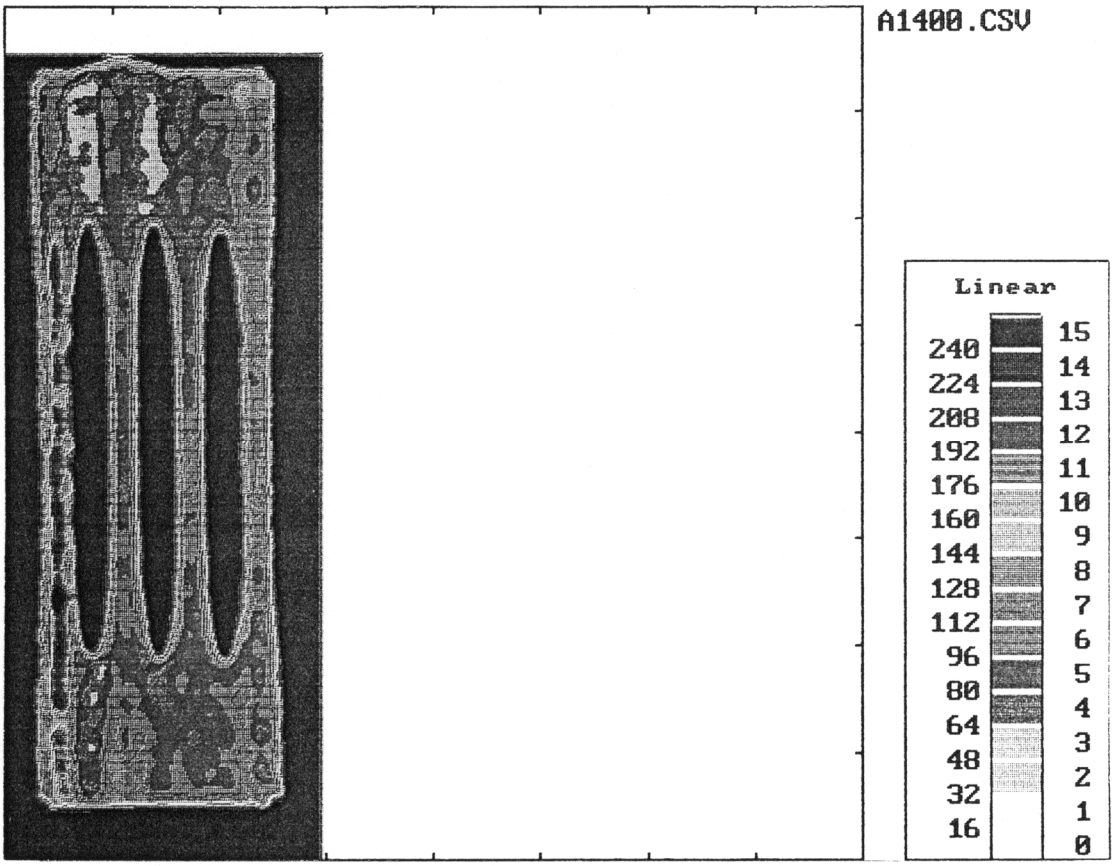

FIGURE 43: C-scan of (left to right) AM-7-2, AM-7-5, AM-7-6, and AM-1-5 after heat treatment at 1400 °C. *Color 0*: Low amplitude signal; *Color 15*: High amplitude signal.

Optical Micrographs

The optical micrographs shown in **Figures 47-50** represent slices taken from the end or "grip" section of the as-fabricated and heat-treated specimens. The optical micrographs show distinct differences among fiber diameters and fiber-spacing within the matrix. The fiber diameters generally vary between 7 and 20 μm, although there are a few fibers which are smaller and larger. Extensive porosity is also seen in all of the optical micrographs. In addition, triangular or diamond shaped voids, characteristic of the CVI process, appear in all of the micrographs.

The optical micrographs clearly illustrate the changes which take place at the fiber-matrix interface after the CMC's have been exposed to elevated temperatures. Optical micrographs of polished samples show that there are no surface discontinuites between the matrix and the surface of the fibers in the as-fabricated samples. **Figure 44** represents a typical as-fabricated sample. In contrast, crescent-shaped voids are apparent around the fibers' surface in the samples heat-treated at 1200 °C and 1400 °C (**Figures 47-50**).

Samples from two specimens heat-treated at 1000 °C, AM-8-1 (coated) and AM-2-1 (uncoated), are shown in **Figures 45** and **46**, respectively. In these optical micrographs, black rings appear around each fiber. These black rings are caused by the oxidation of the carbon interphase and separation of the fibers from the matrix. Trace scans from the electron microprobe analysis, discussed in the next section, will substantiate these claims. Few matrix cracks are visible.

Samples from two specimens heat-treated at 1200 °C, AM-7-3 (coated) and AM-1-6 (uncoated), are shown in **Figures 47** and **48**, respectively. Crescent-shaped rings appear around the fibers. Some of the fibers appear to have separated from one side of their hole while remaining attached to

the other side. In **Figure 47**, matrix cracks are visible; some of the matrix cracks follow the profile of the fibers.

Figures 49 and **50** are optical micrographs of two specimens heat-treated at 1400 °C, AM-7-6 (coated) and AM-1-5 (uncoated). Extensive matrix microcracking and irregular-shaped rings around some of the fibers are seen **Figure 49**. Other fibers appear to be in their as-fabricated condition. In **Figure 50**, there are large crescent-shaped voids around the fibers, while few matrix cracks are visible.

These results indicate that there are distinct difference among the specimens tested at 1000 °C, 1200 °C, and 1400 °C. The changes occurring at the carbonaceous interphase support the findings of the NDE tests preceding this section. They also support the room temperature mechanical tension tests which appear after this section.

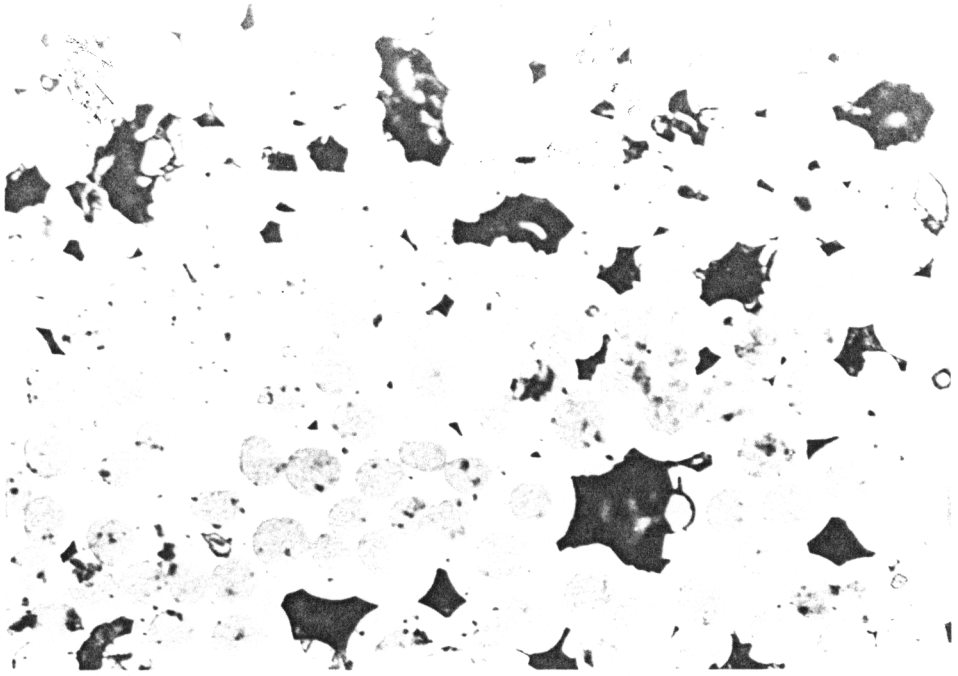

FIGURE 44: Optical micrograph of as-fabricated AM-2-1; 400X

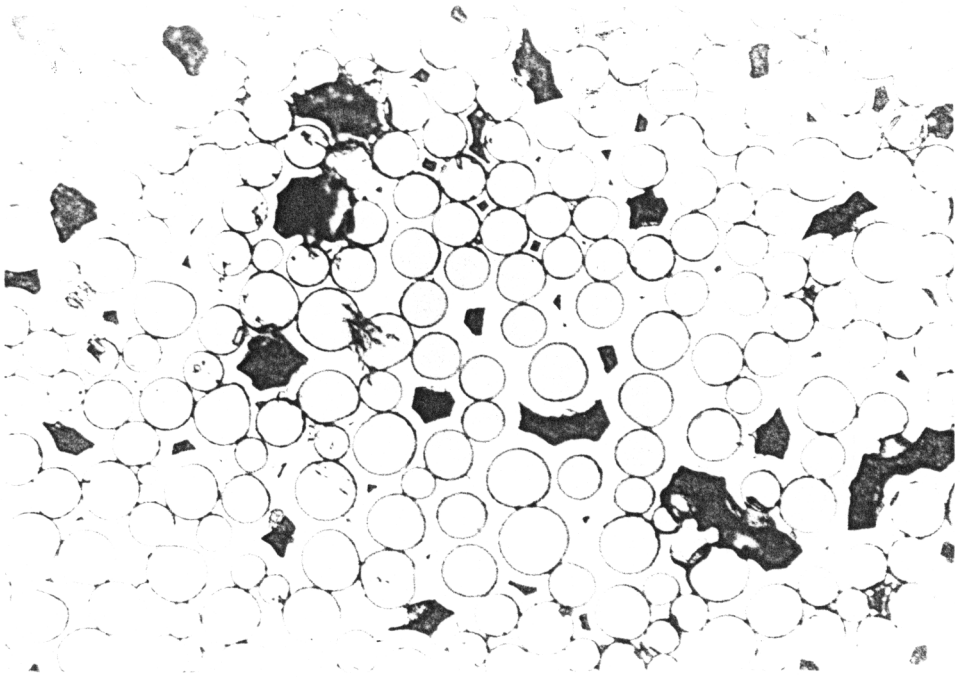

FIGURE 45: Optical micrograph of AM-8-1 after heat treatment at 1000 °C; 400X.

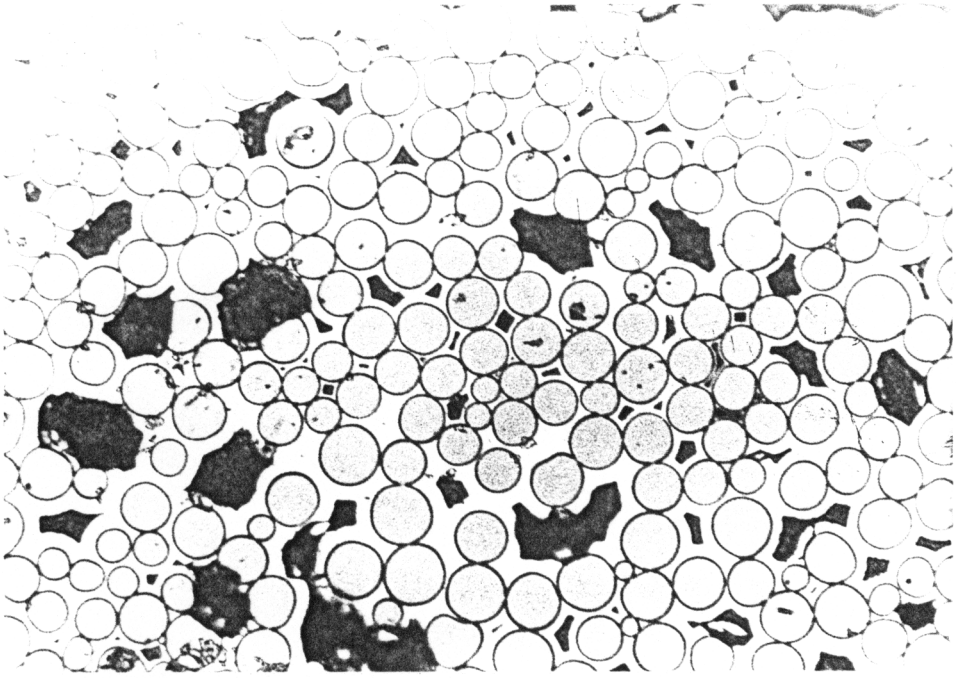

FIGURE 46: Optical micrograph of AM-2-1 after heat treatment at 1000 °C; 400X.

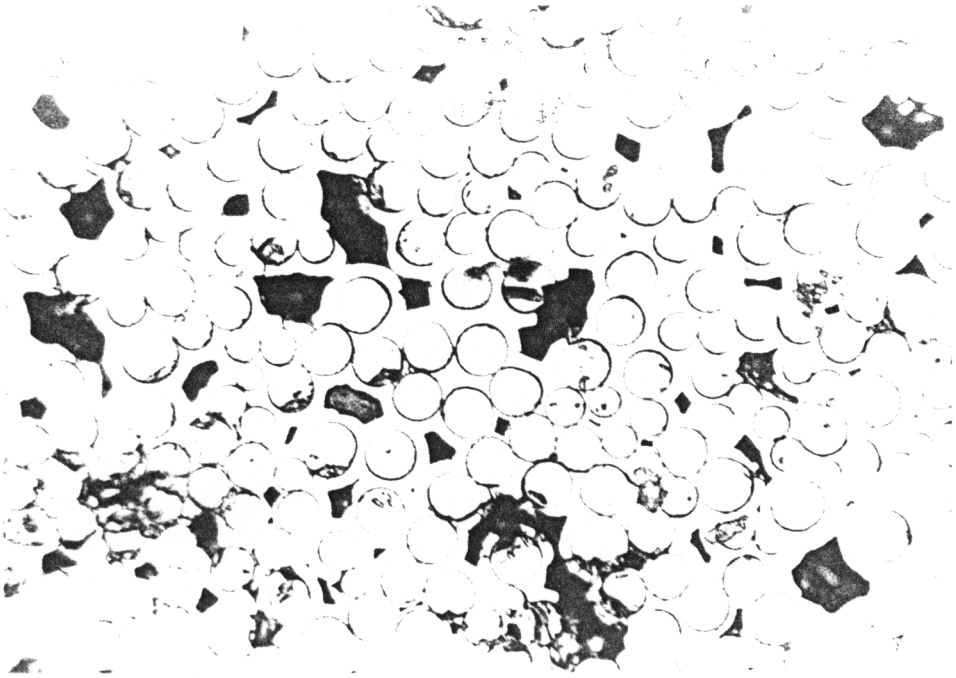

FIGURE 47: Optical micrograph of AM-7-3 after heat treatment at 1200 °C; 400X.

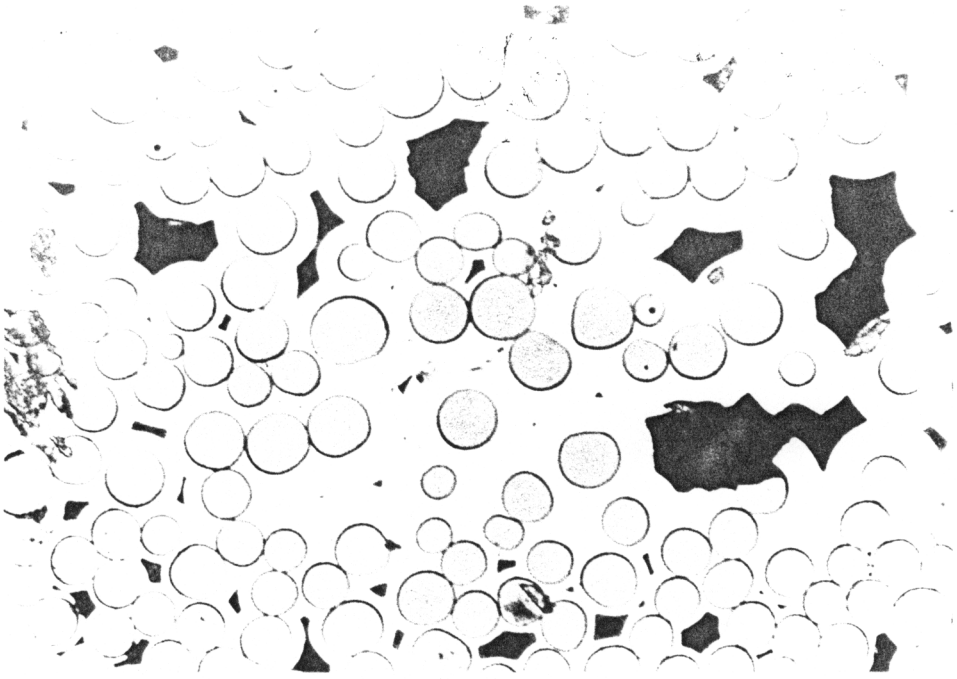

FIGURE 48: Optical micrograph of AM-1-6 after heat treatment at 1200 °C; 400X.

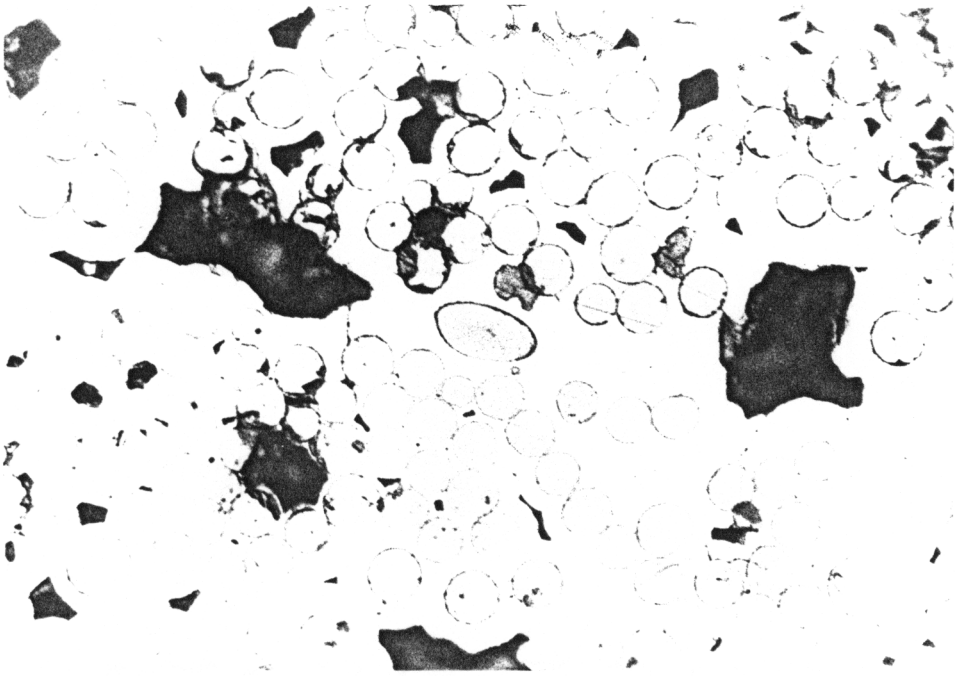

FIGURE 49: Optical micrograph of AM-7-6 after heat treatment at 1400 °C; 400X.

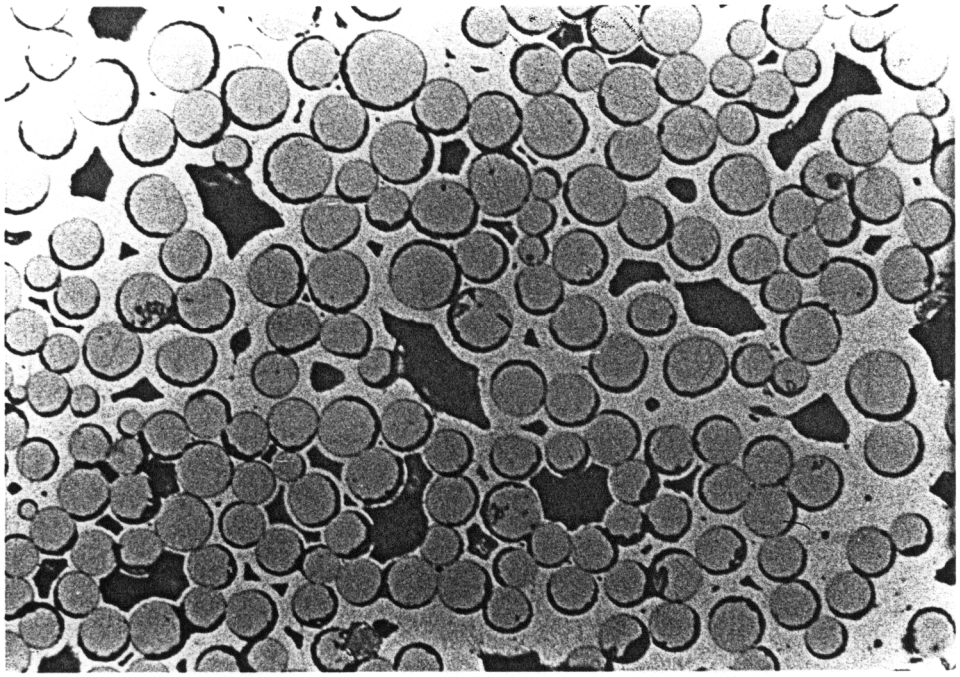

FIGURE 50: Optical micrograph of AM-1-5 after heat treatment at 1400 °C; 400X.

Electron Microprobe Results

Line or trace scans were made across the fiber diameters of two as-fabricated specimens, AM-7-2 (**Figure 51**) and AM-1-7 (**Figure 52**), and two specimens heat treated at 1400 °C, AM-7-6 (**Figure 53**) and AM-1-5 (**Figure 54**). The specimens were chosen to represent the coated and uncoated specimens, respectively. (The spot-size of the electron beam used to perform the scans was approximately 1μm in diameter.) Each of the four scans shown in **Figures 51-54** contain three lines representing the elemental composition (% atomic weight) along each point of the line scan. The blue line at the bottom of the chart represents the amount of oxygen present; the black line in the center of the chart represents the amount of carbon present; and the red line at the top of chart represents the amount of silicon present.

The elemental composition at any point along the X-axis of the scan may be determined by drawing a vertical line at that point; the Y-coordinates of the points on the oxygen, carbon, and silicon lines which are intersected by the vertical line represent the elemental composition. At any point the sum of three elements' weight percentages should total 100%. However, in these scans it is obvious that the total is slightly over 100%. There are two reasons for this discrepancy: (1) the true chemical composition of the Nicalon fibers in the investigated composite material was unknown; consequently, the standard that was used for the Nicalon fibers (see Chapter 3, "Test Strategy") may have been incorrect, and (2) before being analyzed, the specimens were placed in a vacuum chamber for 24 hours; this period of time may not have been adequate to purge the samples and eliminate the remnants of out-gassing.

Five regions are represented in each line scan. Moving from left to right the regions are as follows: (1) matrix to the left of the fiber, (2) left interphase, (3) fiber, (4) right interphase, and (5) matrix

to the right of the fiber. Referring to the trace scans of the two fabricated specimens (**Figures 51 and 52**), silicon is the main constituent of both the matrix and fibers, followed by carbon and lastly oxygen. More silicon is found in the matrix (≈ 72% a.w.) than in the fibers (≈ 57% a.w.). Almost no oxygen is present in the matrix, while approximately 10% a.w. is found in the fibers. The interphase region contains more carbon than either the matrix or the fibers.

The trace scans of the two specimens that were heat treated at 1400 °C are shown in **Figures 53 and 54**. The trace scan of heat-treated AM-7-6 is very similar to the scans from the as-fabricated specimens; however, there does appear to be a decrease in silicon in the interphase region of AM-7-6. The differences between the scan of heat-treated AM-1-5 and the trace scans of the two as-fabricated specimens are more pronounced. There is a clear decrease in carbon at the left and right interphase regions; the decrease at the right interphase is more severe. In this same region the silicon content has decreased, while the oxygen content has increased. These findings are consistent with CO and SiO evolution and SiO_2 formation which are known to occur at elevated temperatures.

In addition to the one-dimensional line scans, two-dimensional elemental maps are shown in Figures 55, 56, and 57. The elemental maps provide only qualitative results. Only the silicon, oxygen, and carbon maps for as-fabricated AM-1-7 are shown.

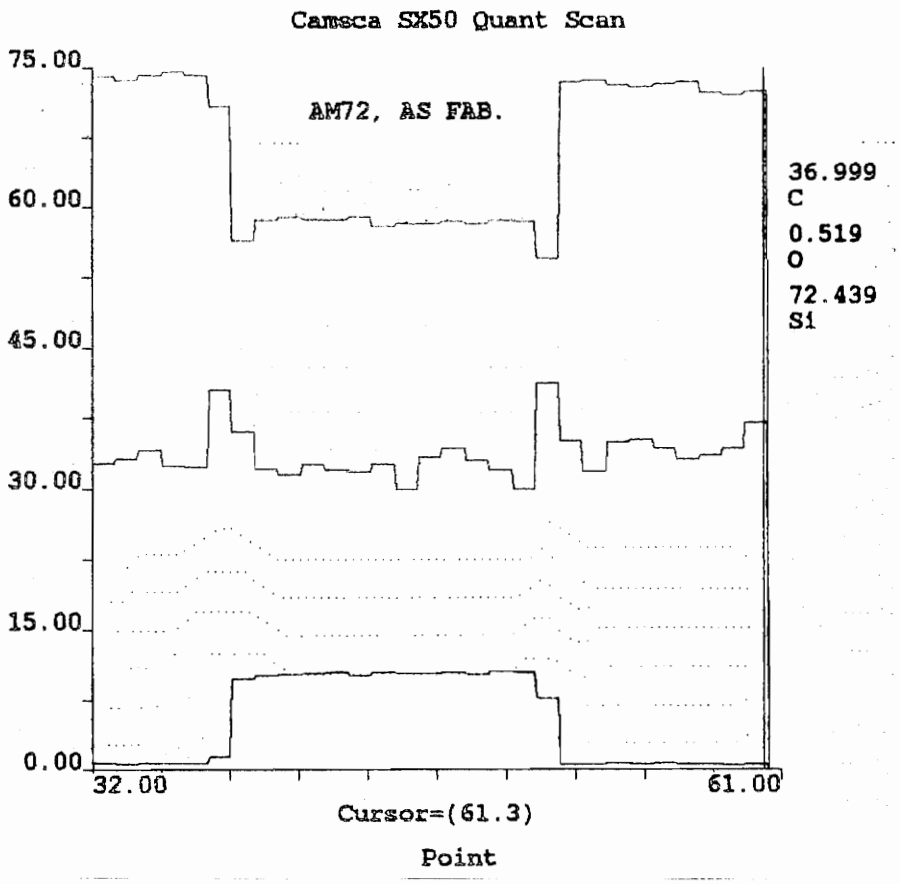

FIGURE 51: Trace scan of as-fabricated, coated AM-7-2. *X-axis*: Position (1μm step); *Y-axis*: Elemental Composition (% atomic weight).

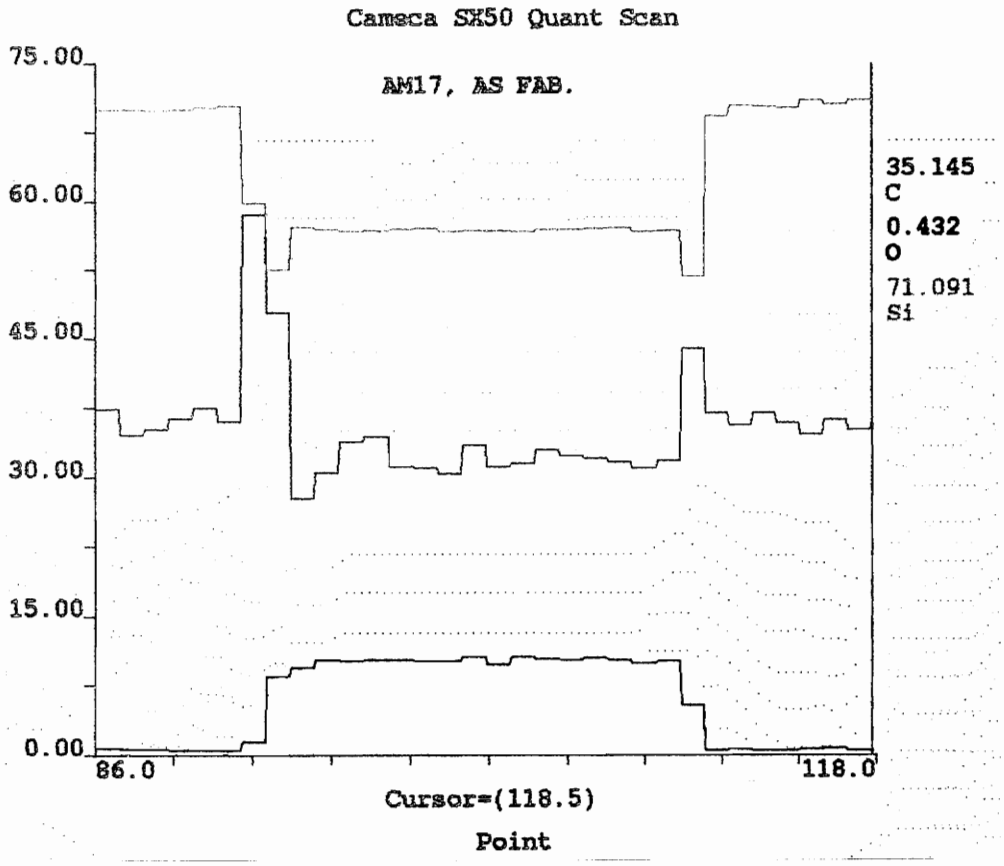

FIGURE 52: Trace scan of as-fabricated, uncoated AM-1-7. *X-axis*: Position (1μm step); *Y-axis*: Elemental Composition (% atomic weight).

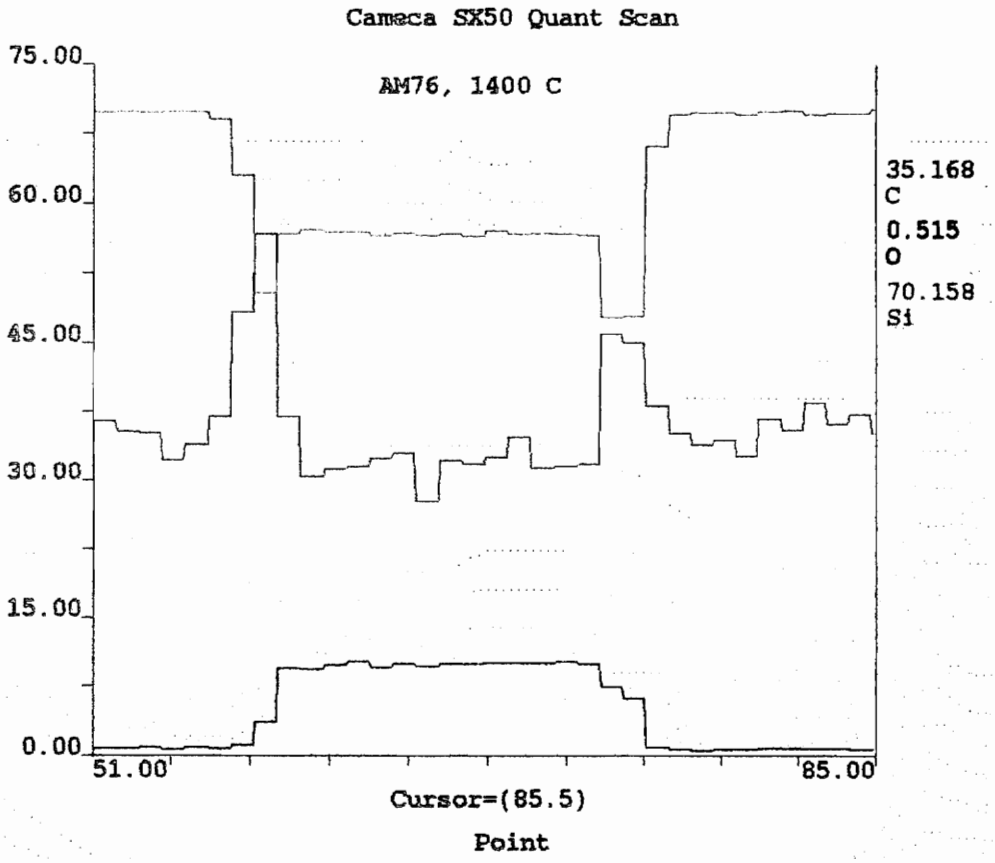

FIGURE 53: Trace scan of coated AM-7-6 after heat treatment at 1400 °C. *X-axis*: Position (1μm step); *Y-axis*: Elemental Composition (% atomic weight).

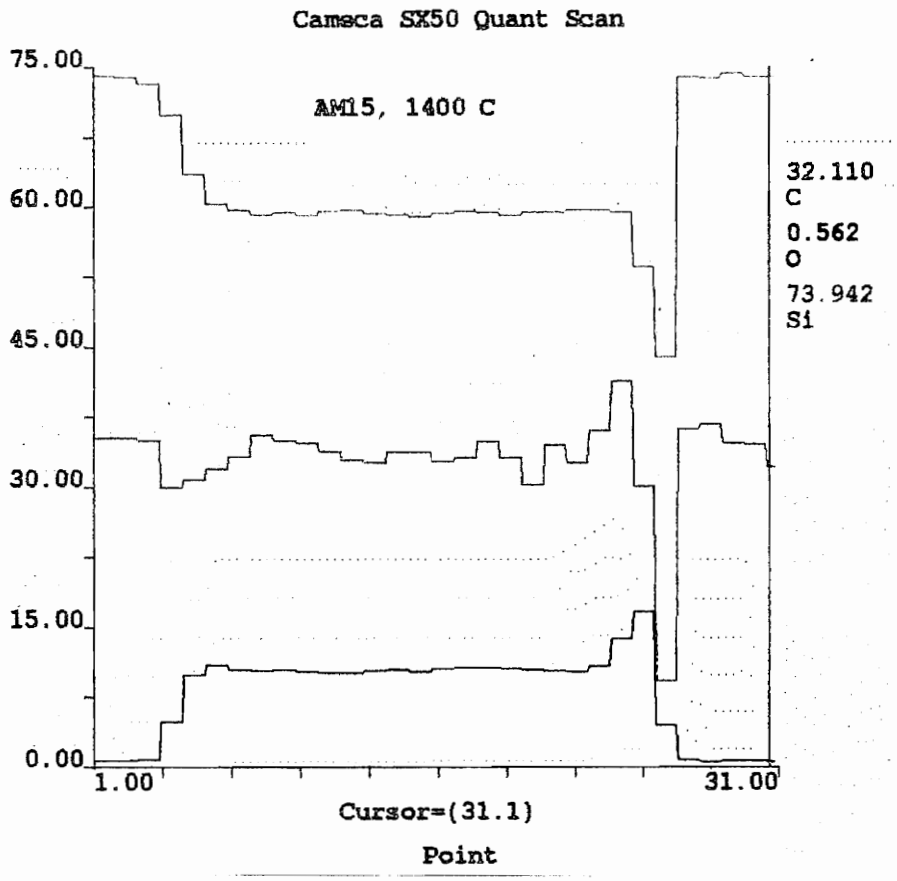

FIGURE 54: Trace scan of uncoated AM-1-5 after heat treatment at 1400 °C. *X-axis*: Position (1μm step); *Y-axis*: Elemental Composition (% atomic weight).

Increasing % atomic weight of carbon

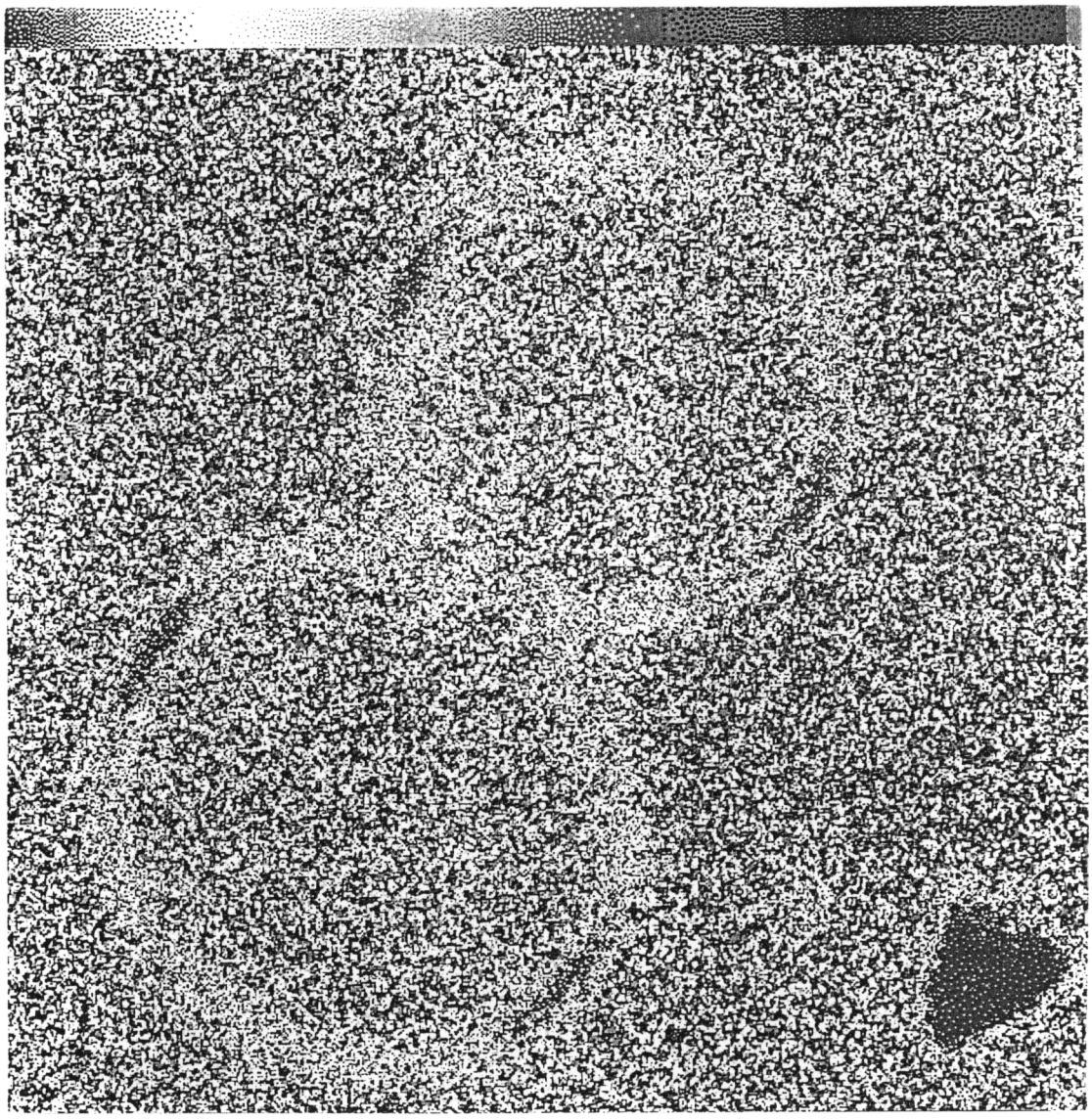

FIGURE 55: Carbon map of as-fabricated AM-1-7.

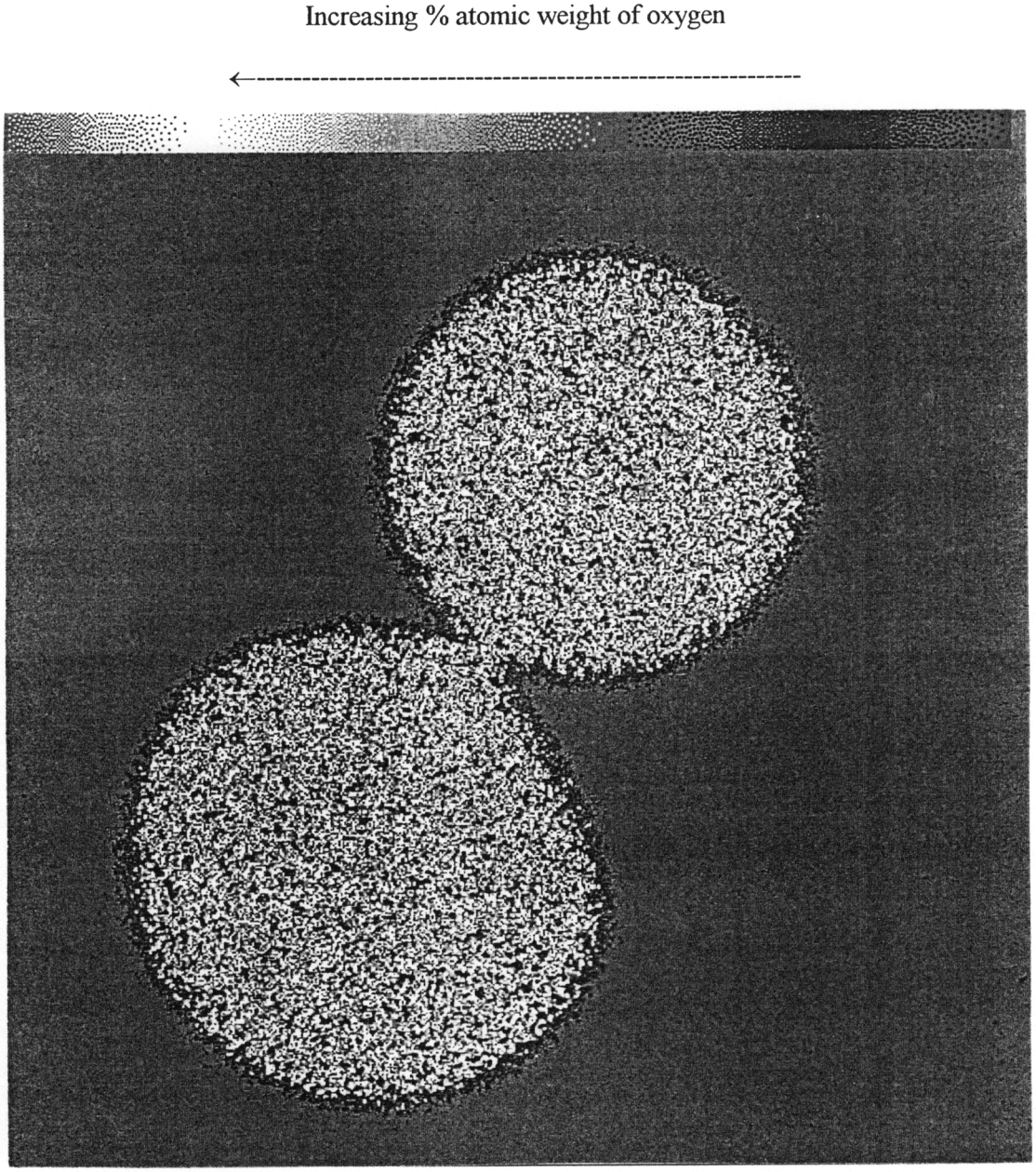

FIGURE 56: Oxygen map of as-fabricated AM-1-7.

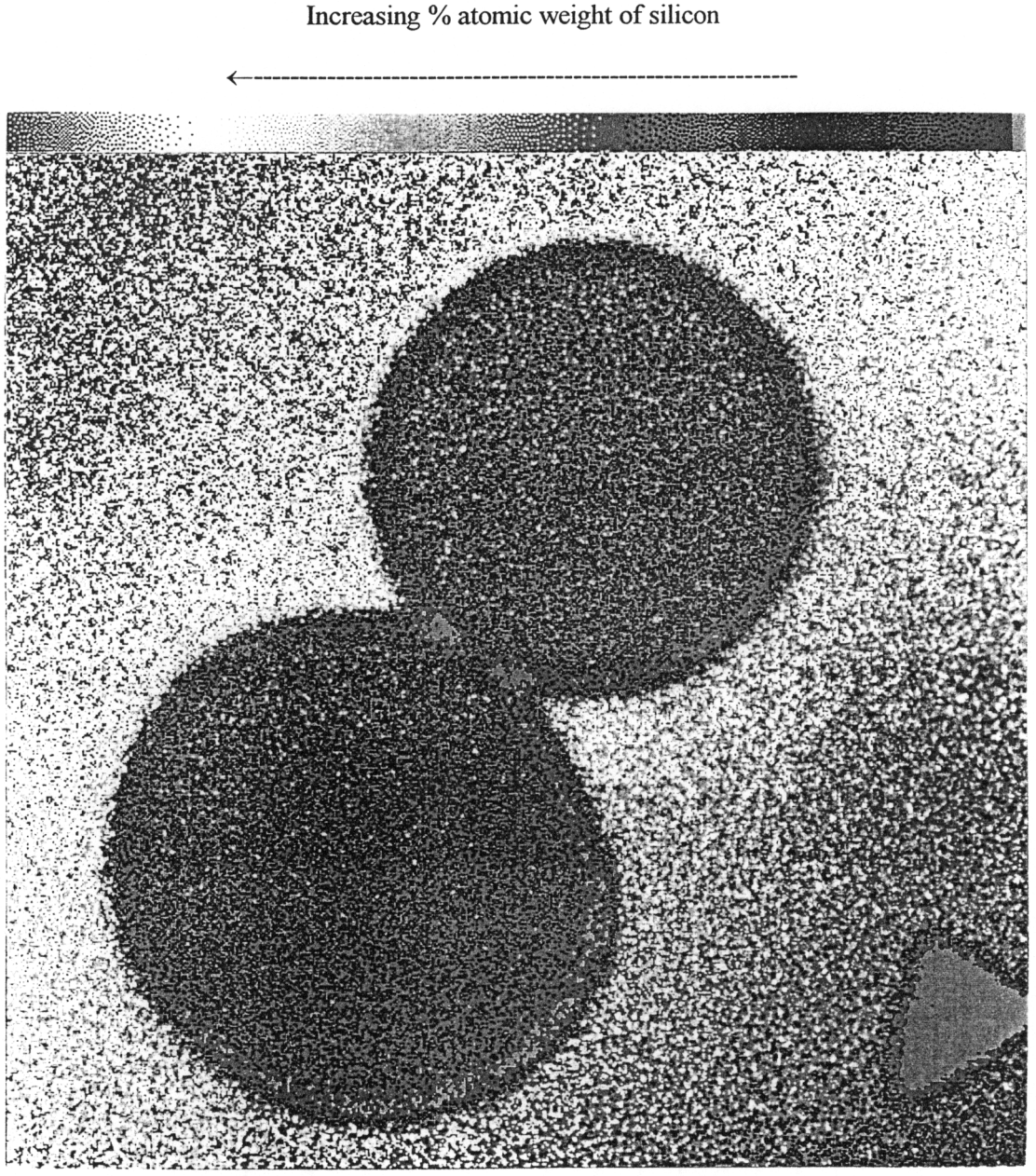

FIGURE 57: Silicon map of as-fabricated AM-1-7.

Backscatter Electron (BSE) Images from Electron Microprobe Analysis

The SEM capabilities of the electron microprobe analyzer were used to make four backscatter electron (BSE) images of as-fabricated and heat treated specimens. In **Figures 58** and **59**, as-fabricated specimens AM-7-2 and AM-1-7 are shown, respectively. Two specimens thermally exposed to 1400 °C, AM-7-6 and AM-1-5, are shown in **Figures 60** and **61**, respectively.

Although the BSE images are very similar in appearance to the optical micrographs, the nature of the contrast is due to chemical differences as opposed to optical differences. Accordingly, the BSE images directly show that the chemical composition of the matrix, interphase, and fibers are different and that they are subject to change after heat treatment. In **Figures 58-61**, the matrix is a light shade of gray, the fiber is a darker shade of gray, and the carbonaceous interphase is black. In **Figure 59**, there is another gradation of gray which appears as a "halo" around the fibers. This may be the result of a two-step CVI process or a change in reactant composition during the CVI process. In **Figures 60** and **61**, the distinct black rings that were present around the fibers in the as-fabricated samples appear to be fading. The fibers from AM-7-6 **(Figure 60)** have an irregular outline, consistent with oxidation of the carbon interphase. The fibers from AM-1-5 **(Figure 61)** are bounded on one side by a crescent-shaped void and appear to be ringed in white near this void. This white region may be a layer of silica or some other oxidation or reduction product.

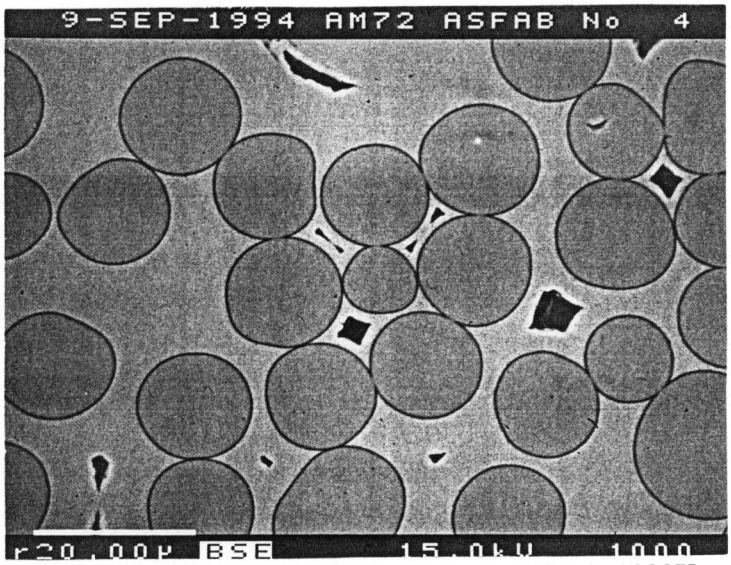

FIGURE 58: BSE image of as-fabricated AM-7-2; 1000X.
(Note: White scale in bottom left corner represents 20 μm.)

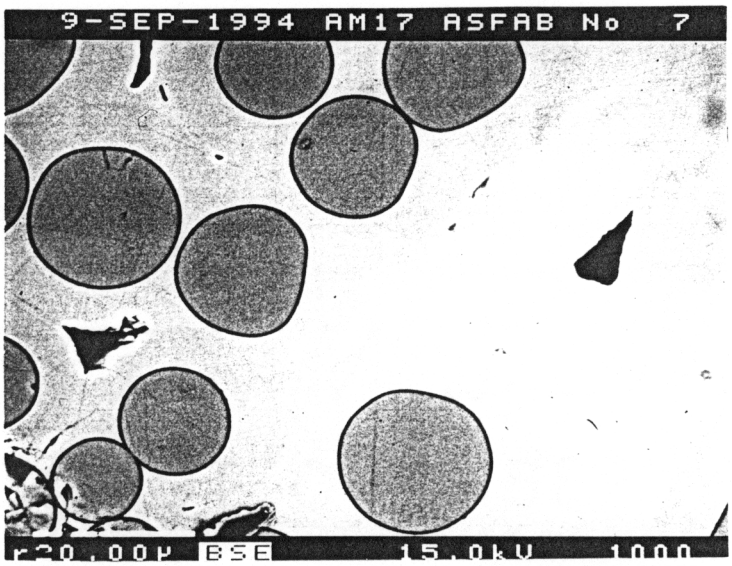

FIGURE 59: BSE image of as-fabricated AM-1-7; 1000X.
(Note: White scale in bottom left corner represents 20 μm.)

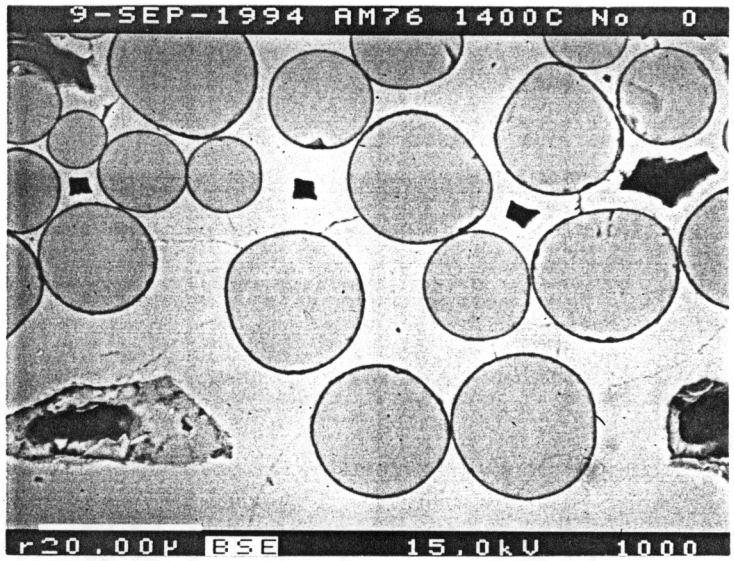

FIGURE 60: BSE image of AM-7-6 after heat treatment at 1400 °C; 1000X. (Note: White scale in bottom left corner represents 20 µm.)

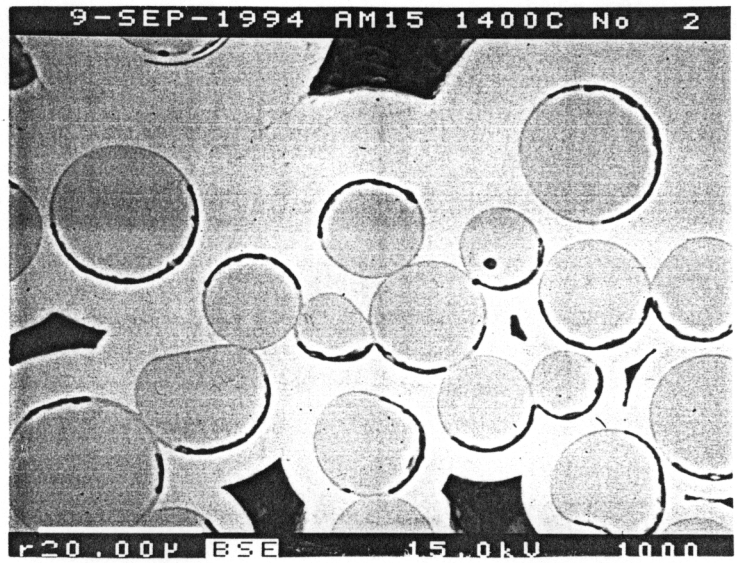

FIGURE 61: BSE image of AM-1-5 after heat treatment at 1400 °C; 1000X. (Note: White scale in bottom left corner represents 20 µm.)

Acoustic Emission Monitoring and Tensile Test Results

Loading histories with acoustic emission data are shown in **Figures 62-69**. (Note: Specimens AM-8-1 and AM-7-4 were not tested.) The curves may be divided into four regions: (1) Region I - strain increases linearly with load; acoustic activity gradually increases, (2) Transition - site of peak acoustic activity, (3) Region II - non-linear behavior; acoustic activity gradually decreases to a steady level, and (4) Rupture - often accompanied by a spike of acoustic activity.

The loading history and acoustic emission data for as-fabricated specimen AM-7-2 (coated) is shown in **Figure 62**. **Figure 62** represents a typical composite response to a room temperature tensile test [80]. Region I is linear with a smooth transition zone that joins a non-linear portion of the curve. The transition zone and non-linear portion of the curve are attributed to progressive microcracking of the matrix. Brittle failure occurs at a load of 1642 lbs. and a strain of 0.706 %. Region I is accompanied by acoustic activity which increases with load. This acoustic activity peaks at the transition zone, gradually decreases to a steady level, and then momentarily peaks at rupture.

The loading history and acoustic emission data for specimens heat-treated at 1000 °C, AM-1-7 (uncoated) and AM-2-1 (uncoated), are shown in **Figures 63** and **64**. Both of the load vs. strain curves consist of a fairly linear Region I and a non-linear region of rupture and fiber pull-out. Rupture is punctuated by a narrow peak of acoustic activity and is followed by a decline in acoustic emissions. Specimen AM-1-7 ruptures at a load of 444 lbs. and a strain of 0.117%; specimen AM-2-1 fails at a load of 244 lbs and a strain of 0.019%. Both specimens experienced brittle failures with limited fiber pull-out. The thinner specimen, AM-1-7, has an inclined fracture

surface typical of a plane stress fracture. The thicker specimen, AM-2-1, has a fracture surface typical of a mixed plane-stress, plane-strain failure.

The test results for specimens heat-treated at 1200 °C, AM-7-3 (coated) and AM-1-6 (uncoated), are shown in **Figures 65** and **66**. The load vs. strain curves for AM-7-3 and AM-1-6 more closely resemble the curve for as-fabricated specimen AM-7-2. They both have a linear Region I and non-linear Region II, followed by failure. However, unlike the brittle failure seen in the as-fabricated specimen, the heat-treated specimens have extensive fiber pull-out. At failure the load first drops rapidly and then declines gradually. Specimen AM-7-3 ruptures at a load of 752 lbs. and a strain of 0.344%; specimen AM-1-6 fails at a load of 422 lbs and a strain of 0.252%. (Because the acoustic emissions saturated the data acquisition system, a lapse in acoustic activity is seen in **Figure 65**; the signal attenuation was increased in later AE tests.)

The test results for specimens heat-treated at 1400 °C, AM-7-5 (coated), AM-7-6 (coated), and AM-1-5 (uncoated), are shown in **Figures 67-69**. The results are very similar to the results from the specimens heat-treated at 1200 °C. They all have a linear Region I and non-linear Region II, followed by failure. The transition from linear to non-linear behavior is accompanied by an increase in acoustic activity. In **Figures 67** and **69**, there is a spike of acoustic activity at matrix failure and the onset of fiber pull-out. Specimen AM-7-5 ruptures at a load of 666 lbs. and a strain of 0.535%; specimen AM-7-6 ruptures at a load of 636 lbs and a strain of 0.512%; specimen AM-1-5 ruptures at a load of 388 lbs. and a strain of 0.287%. All of the specimens heat-treated at 1400 °C experienced extensive fiber pull-out.

The tensile test results are summarized in **Table 4**. The specimens heat-treated at 1400 °C experienced the greatest loss of strength, according to the ultimate strength values for uncoated specimens AM-1-7, AM-1-6, and AM-1-5. Based on the ultimate strengths of these uncoated specimens, the ultimate strength of specimen AM-2-1 appears to be an anomalous result. The ultimate strength of coated specimen AM-7-3 after heat treatment at 1200 °C is more than 50% less than the ultimate strength of the coated as-fabricated specimen, AM-7-2. The ultimate strengths of the coated and uncoated specimens heat-treated at 1400 °C are approximately 10% less than the strengths of the corresponding specimens heat-treated at 1200 °C.

TABLE 4: Tensile Test Results

Specimen Identification	Heat Treatment 100 hrs.	Load at Failure lbs.	Ultimate Stress ksi (MPa)	Ultimate Strain %	Modulus msi
AM-7-2 (coated)	as-fabricated	1642	27.3 (188)	0.706	27.1
AM-1-7 (uncoated)	1000 C	444	7.82 (53.9)	0.117	16.0
AM-2-1 (uncoated)	1000 C	244	4.09 (28.2)	0.019	17.6
AM-7-3 (coated)	1200 C	752	12.8 (88.1)	0.344	26.0
AM-1-6 (uncoated)	1200 C	422	7.63 (52.3)	0.252	27.0
AM-7-5 (coated)	1400 C	666	11.3 (78.2)	0.535	21.0
AM-7-6 (coated)	1400 C	636	10.7 (73.9)	0.512	22.3
AM-1-5 (uncoated)	1400 C	388	7.00 (48.2)	0.287	13.3

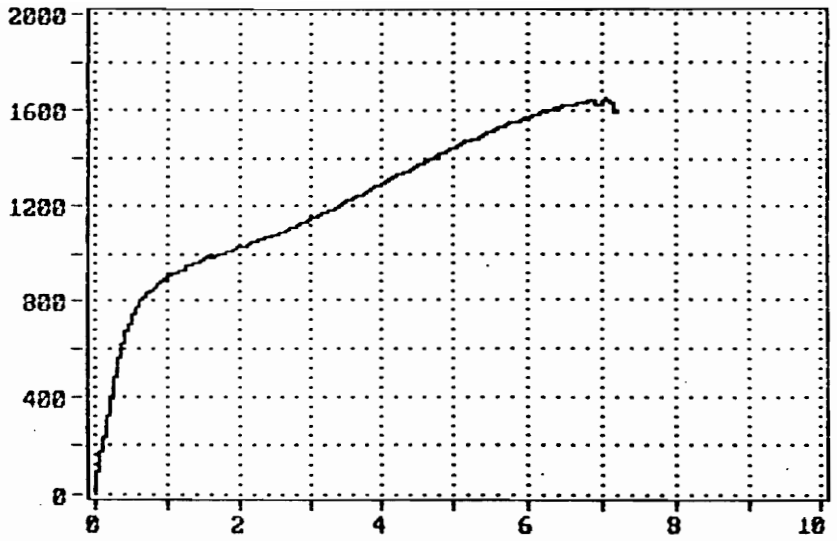

FIGURE 62a: As-fabricated AM-7-2 (coated): Load (lbs.) vs. Strain (% x 10).

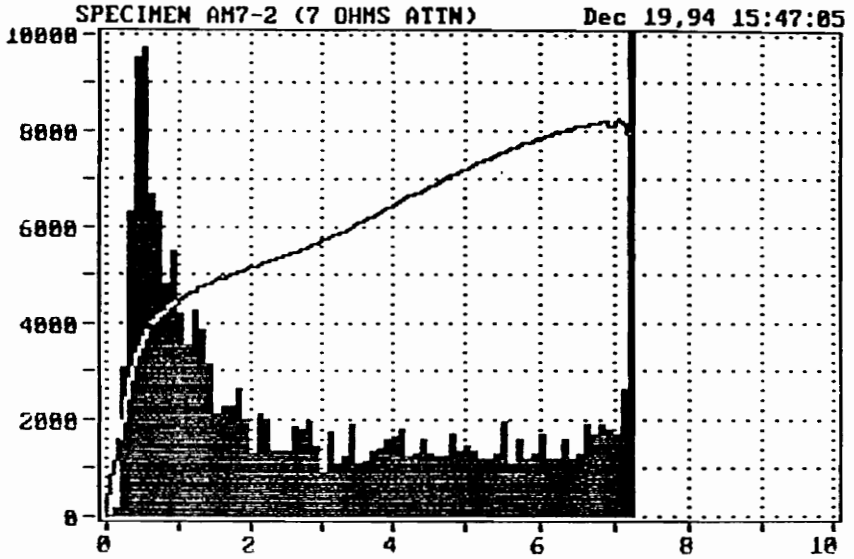

FIGURE 62b: Load and AE data for as-fabricated AM-7-2 (coated): Counts vs. Strain (% x 10).

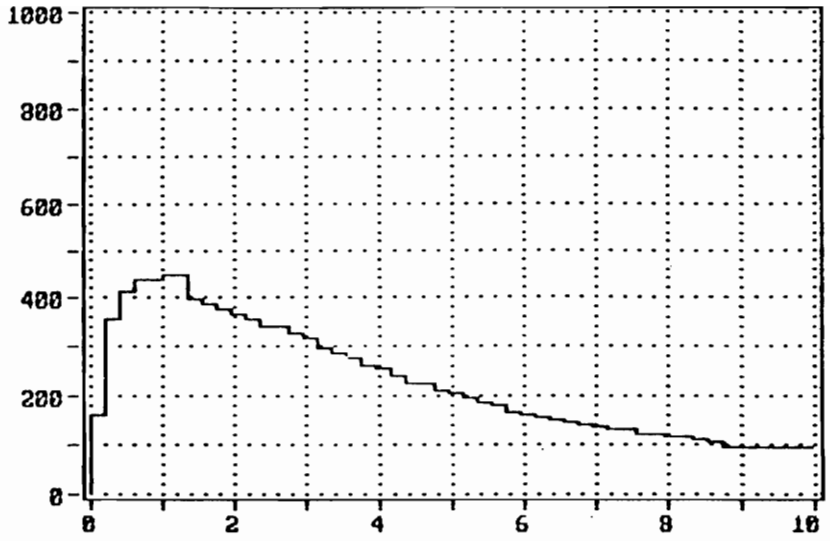

FIGURE 63a: AM-1-7 (uncoated) after heat treatment at 1000 °C: Load (lbs.) vs. Strain (% x 10).

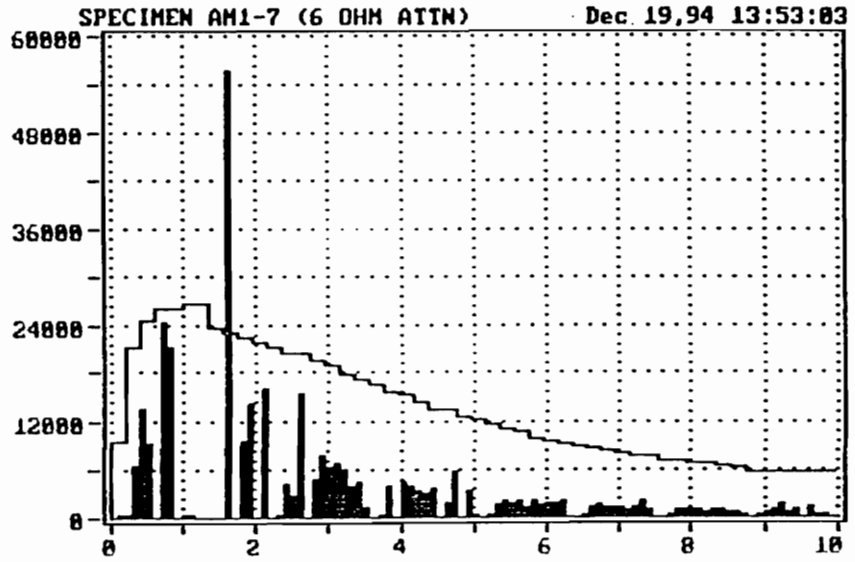

FIGURE 63b: Load and AE data for AM-1-7 (uncoated) after heat treatment at 1000 °C: Counts vs. Strain (% x 10).

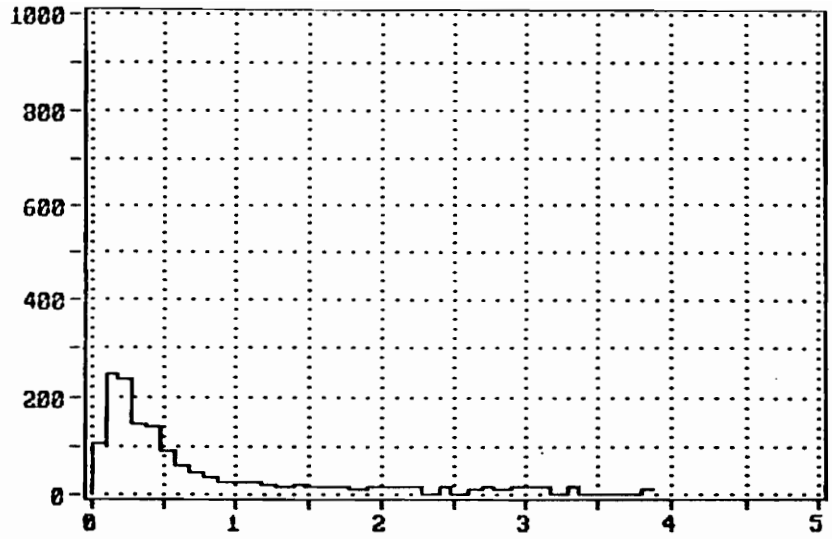

FIGURE 64a: AM-2-1 (uncoated) after heat treatment at 1000 °C: Load (lbs.) vs. Strain (% x 10).

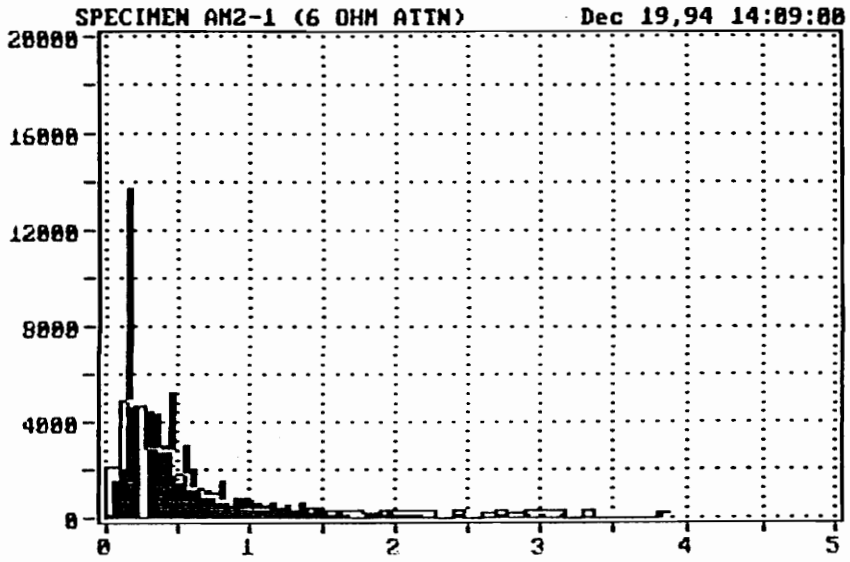

FIGURE 64b: Load and AE data for AM-2-1 (uncoated) after heat treatment at 1000 °C: Counts vs. Strain (% x 10).

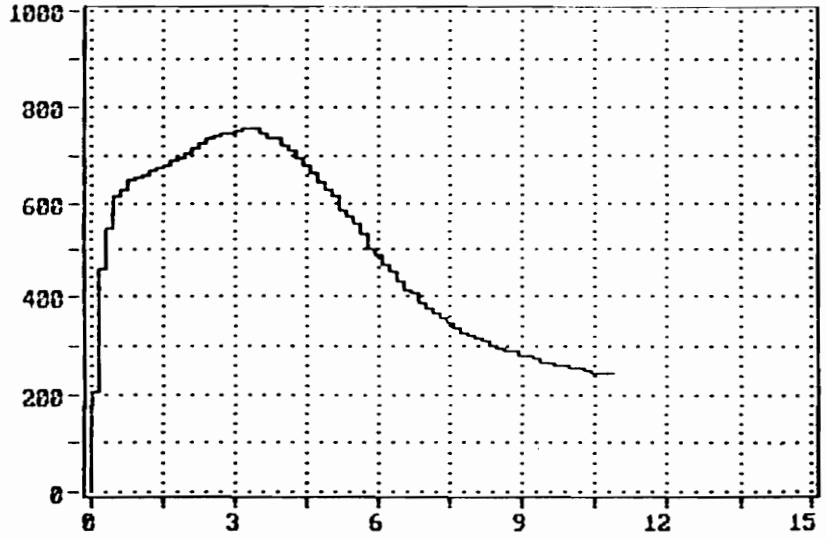

FIGURE 65a: AM-7-3 (coated) after heat treatment at 1200 °C: Load (lbs.) vs. Strain (% x 10).

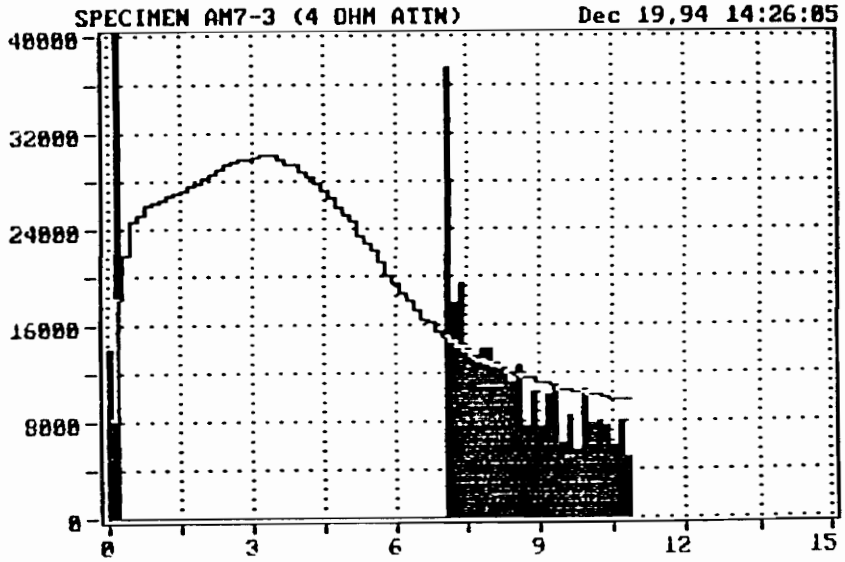

FIGURE 65b: Load and AE data for AM-7-3 (coated) after heat treatment at 1200 °C: Counts vs. Strain (% x 10).

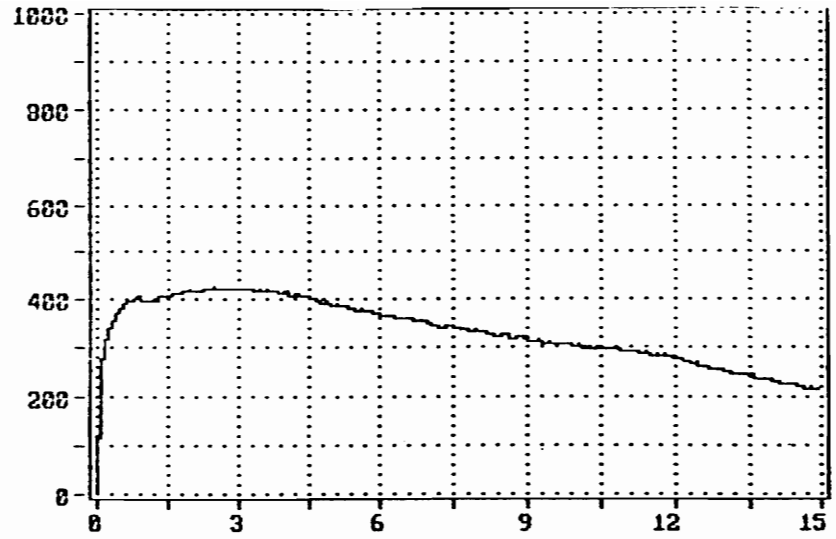

FIGURE 66a: AM-1-6 (uncoated) after heat treatment at 1200 °C: Load (lbs.) vs. Strain (% x 10).

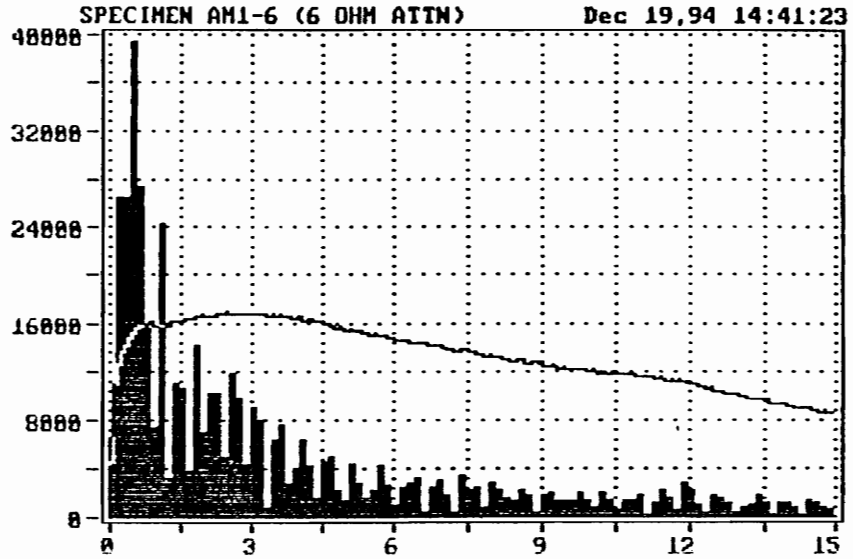

FIGURE 66b: Load and AE data for AM-1-6 (uncoated) after heat treatment at 1000 °C: Counts vs. Strain (% x 10).

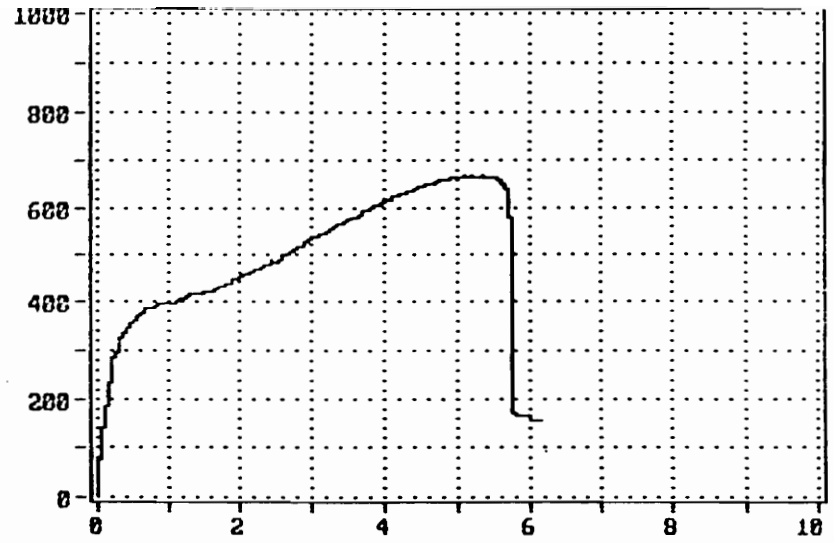

FIGURE 67a: AM-7-5 (coated) after heat treatment at 1400 °C: Load (lbs.) vs. Strain (% x 10).

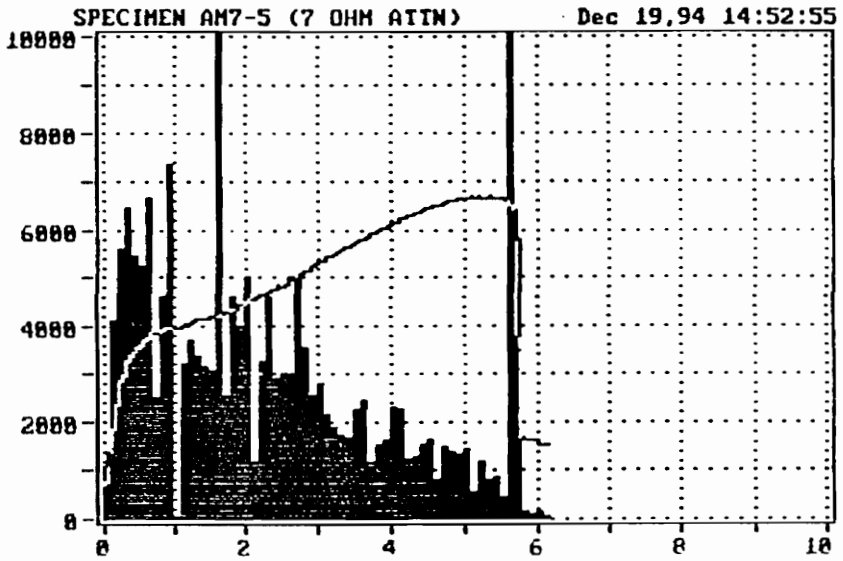

FIGURE 67b: Load and AE data for AM-7-5 (coated) after heat treatment at 1400 °C: Counts vs. Strain (% x 10).

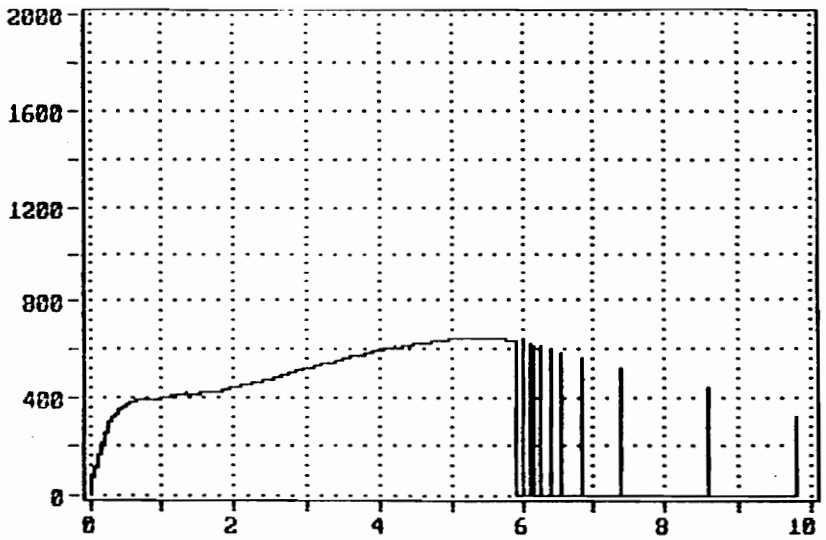

FIGURE 68a: AM-7-6 (coated) after heat treatment at 1400 °C: Load (lbs.) vs. Strain (% x 10).

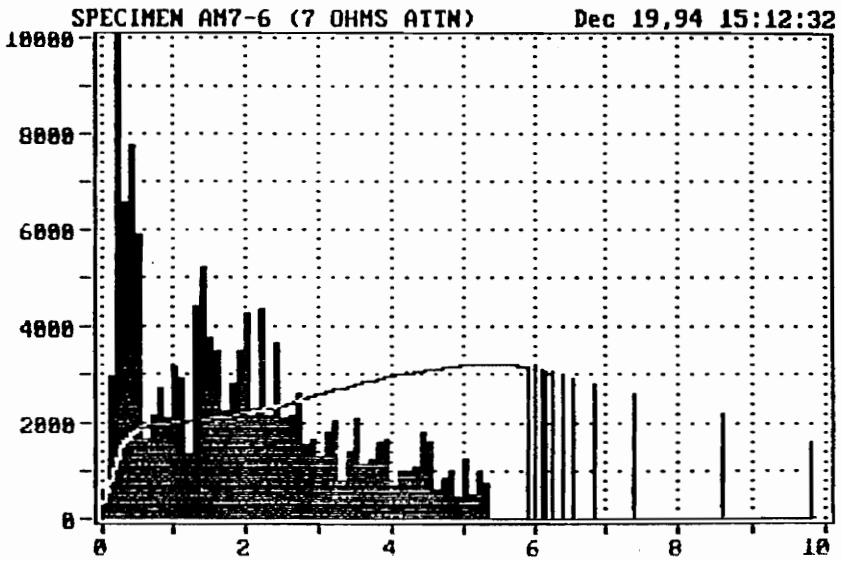

FIGURE 68b: Load and AE data for AM-7-6 (coated) after heat treatment at 1400 °C: Counts vs. Strain (% x 10).

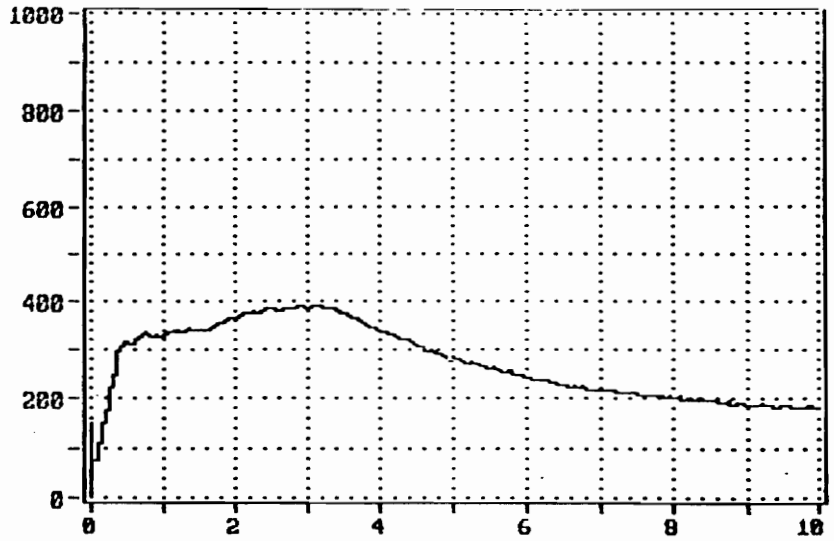

FIGURE 69a: AM-1-5 (uncoated) after heat treatment at 1400 °C: Load (lbs.) vs. Strain (% x 10).

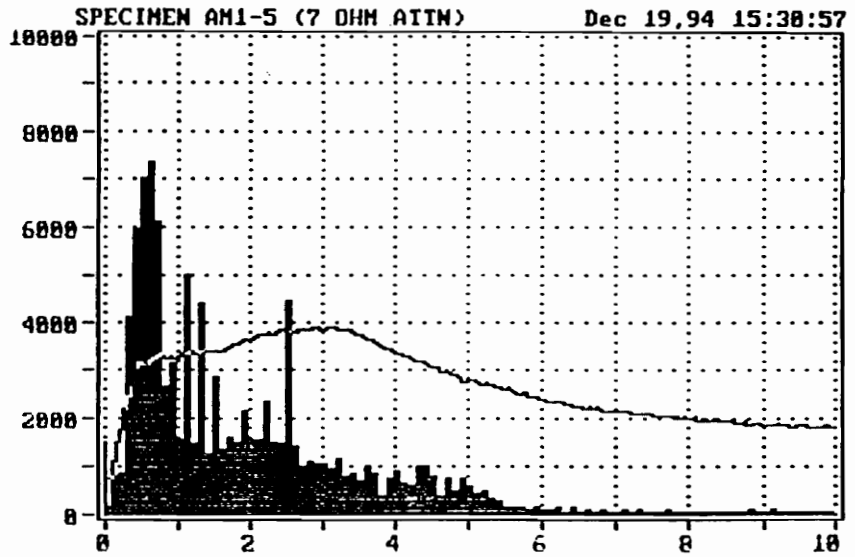

FIGURE 69b: Load and AE data for AM-1-5 (uncoated) after heat treatment at 1400 °C: Counts vs. Strain (% x 10).

7. CONCLUSIONS, EVALUATION OF ANALYTICAL METHODS, AND FUTURE WORK

The purpose of this investigation was to nondestructively characterize a high-temperature ceramic matrix composite (CMC) before and after exposure to 1000, 1200, and 1400 °C in oxidizing atmospheres of air. Concurrently, the specific nondestructive testing methods were evaluated for their effectiveness in detecting changes in the CMC. A 2-D Nicalon fiber-reinforced, chemical vapor infiltrated composite (manufactured by Amercom) was used as the model CMC for this investigation. Two groups of SiC/SiC specimens were studied. One group of specimens was coated with a CVD SiC seal coat; the other group was not coated.

NDT methods including acoustic microscopy, acousto-ultrasonics, film X-ray radiography, and immersion scan ultrasonics were used to characterize changes caused by thermal exposure. The electron microprobe was used to characterize chemical stability, while tensile tests performed at room-temperature provided strength data and a means for monitoring acoustic emission. Other supporting techniques included optical microscopy and scanning electron microscopy.

Conclusions

Visual Examination: All of the specimens exhibited changes in surface appearance. The coated specimens heat-treated at 1200 °C and 1400 °C exhibited greater changes than the corresponding uncoated specimens; these changes were attributed to the oxidation of the CVD SiC seal-coat. Both the coated and uncoated specimens heat-treated at 1000 °C had a pink iridescent surface finish attributed to the refraction of light by a thin layer of silica.

Thermogravimetric Analysis: The specimens also exhibited significant mass instability. All of the specimens except the two uncoated specimens heat treated at 1000 °C experienced a mass increase after heat treatment. These results were consistent with the findings of Huger *et al* [16] and Pluvinage *et al* [80]. The weight loss of the two uncoated specimens was attributed to the pyrolysis of the fiber sizing. Under the same ageing conditions, the mass of the coated specimens increased more than the mass of the uncoated specimens. These differences were also attributed to the pyrolysis phenomenon and the protection offered by the SiC seal-coat. Finally, mass was observed to increase with increased ageing temperature for both coated and uncoated specimens.

SAM Analysis: Based on the results of the SAM analysis, few differences were observed between the as-fabricated and heat-treated specimens. The surface images of the as-fabricated and heat-treated specimens were virtually unchanged; only one specimen experienced a localized surface change. The sub-surface images of the as-fabricated specimens had better contrast than the images of the heat-treated specimens; *i.e.*, the sub-surface of the as-fabricated specimens appeared to reflect more of the transmitted acoustic signals. However, as suggested by the amplitude of the signals reflected from the surface, more of the acoustic waves were reflected at the surface of the heat-treated specimens. Consequently, less acoustic energy was transmitted to the sub-surface, and less was available for reflection from the sub-surface. This increase in surface reflectivity was attributed to the oxidation of the SiC coating, matrix, and fibers; the formation of silica; and the increase in crystallinity of the Nicalon fibers.

AU Results: According to data from the acousto-ultrasonics analysis, significant differences were observed between the as-fabricated and heat-treated specimens. The results from paired difference-in-means tests indicated that thermal ageing, rather than random variations in AU measurements,

caused these differences. The coated and uncoated specimens exhibited different behaviors at the three ageing temperatures. The only coated specimen heat treated at 1000 °C attenuated acoustic signals more strongly after heat treatment. In contrast, the two uncoated specimens did not attenuate the acoustic signals as well after they had been heat treated. Both coated and uncoated specimens attenuated acoustic signals more strongly after they had been heat treated at 1200 °C. This observed increase in attenuation was attributed to microstructural changes that occurred in the matrix, interphase, and fibers. These changes increased the ability of the composite to scatter ultrasonic energy. AU results from the specimens heat treated at 1400 °C were inconclusive. One coated specimen attenuated less energy after heat treatment, while the remaining coated and uncoated specimens attenuated more or less energy depending on transducer position.

Radiographs: There were no observable changes between the X-ray images of the as-fabricated and heat-treated specimens. The areas of high and low X-ray absorption were the same before and after heat treatment. Variations in X-ray absorption were consistent with small variations in specimen thickness and density. Positive prints from the radiographs of the specimens illustrated differences in weave patterns and fiber distributions within the weave.

Results from Immersion Scan Ultrasonics: According to C-scans of the as-fabricated specimens, the coated specimens transmitted more ultrasonic energy than the uncoated specimens. Because the coated specimens were thicker (and equally dense) these results were contrary to expectation. After heat treatment, the coated specimens attenuated more energy, while three out of four uncoated specimens transmitted more energy. As optical micrographs and tensile tests showed, higher ageing temperatures corresponded to more extensive degradation on the surface and within the bulk of a specimen. As the CMC degraded, its ability to transmit ultrasonic energy decreased.

This explanation supported the increase in ultrasonic attenuation that was observed in the coated specimens, but did not support the decrease observed in the uncoated specimens.

Optical Micrographs: Optical micrographs from samples of the as-fabricated specimens showed distinct differences among fiber diameter and fiber-spacing within the matrix. The optical micrographs also illustrated the changes which took place at the fiber-matrix interface after the composite was exposed to elevated temperatures. Black or irregular-shaped rings, and crescent-shaped voids were observed around the fibers after heat treatment. Matrix cracks between fibers and around the fiber profiles were also observed in the micrographs.

Electron Microprobe Results: Results from the electron microprobe analysis showed that the elemental composition of the fiber-matrix interphase changed in response to thermal ageing. According to the trace scans of the as-fabricated specimens, silicon was the main constituent of both the matrix and fibers. More silicon was present in the matrix ($\approx$72 % a.w.) than in the fibers ($\approx$57 % a.w.). Almost no oxygen was present in the matrix, while approximately 10 % a.w. was found in the fibers. The interphase contained more carbon than either the matrix or the fibers. After heat treatment, the fiber-matrix interphase experienced a decrease in carbon and silicon and an increase in oxygen. These findings were consistent with CO and SiO evolution and SiO_2 formation which are known to occur at elevated temperatures. The elemental maps and BSE images substantiated trace scan findings as well as previously discussed optical micrograph findings.

AE Data and Tensile Test Results: According to the mechanical and AE behavior of the CMC specimens, the load vs. strain curves were divided into four regions: (1) Region I - strain increased

linearly with load; acoustic activity gradually increased, (2) Transition - site of peak acoustic activity, (3) Region II - non-linear behavior; acoustic activity gradually decreased to a steady level, and (4) Rupture - often accompanied by a spike of acoustic activity. Specimens heat treated at 1000 °C exhibited brittle failure and limited fiber pull-out, while those heat treated at 1200 °C and 1400 °C exhibited a more gradual decrease in strength and extensive fiber pull-out. After heat treatment, the uncoated specimens had consistently lower ultimate strengths than the coated specimens. As expected, the ultimate strengths of all of the specimens decreased with increased ageing temperature.

Evaluation of Analytical Methods

Scanning Acoustic Microscopy: The scanning acoustic microscope was relatively insensitive to changes in the CMC caused by thermal ageing. A 50 MHz lens was chosen for this study after trial investigations of the CMC specimens were performed using 30, 50, and 100 MHz lenses. Surface examinations revealed no differences between the as-fabricated and heat-treated specimens with the exception of a localized surface change (increased reflectivity) in one heat-treated specimen. In contrast, sub-surface examinations revealed that there were detectable differences in contrast between the images of the as-fabricated and thermally aged specimens. Sub-surface images of as-fabricated specimens had good contrast; whereas, sub-surface images of heat-treated specimens had poor contrast. Although the difference in image-contrast indicates that thermal exposure altered the density and elastic properties of the CMC, this result is subject to interpretation and cannot be qualified or quantified without performing additional nondestructive and destructive tests.

Acousto-Ultrasonics: The acousto-ultrasound technique was able to detect changes in the CMC caused by thermal ageing. The AU technique also was able to detect differences between refractory-coated and uncoated specimens, before and after heat treatment. The size parameter M_0 (zeroth moment), the area under the power spectral density curve, was the AU parameter used in this investigation to compare results; M_0 was measured at specific locations on the specimens. Based on the results of paired difference-in-means tests, the AU measurements from the as-fabricated and heat-treated specimens proved to be statistically different, indicating that thermal ageing could be detected by the AU technique. However, variations in the AU measurements from a "control" specimen indicated that the ambient conditions under which the tests were performed also were affecting the results. Additional investigations will be needed to determine the effects of ambient temperature and humidity on AU measurements and the coupling effectiveness of dry-coupled transducers, relative to testing ceramic matrix composites.

Film X-ray Radiography: X-ray radiography was insensitive to the thermally induced structural changes that occurred in the CMC. However, radiographs were effective in documenting macrostructural anomalies, fiber architecture, and variations in matrix distribution caused by the CVI process in the as-fabricated specimens. The optimal definition and contrast for a composite thickness of ≈0.125" was obtained with a kilovoltage setting of 45 kV and a 2-minute exposure time; Kodak Industrex M film was used. Dye penetrants were not used with X-ray radiography because it was feared that at high temperatures penetrants would act as catalysts or would themselves react with the CMC.

Immersion Scan Ultrasonics: The immersion-scan-ultrasound technique was able to detect changes in the heat-treated specimens. Through-transmission and pulse-echo methods proved to be

sensitive to changes in bulk and surface conditions, respectively. Both 5 MHz and 25 MHz transducers were used to make scans; the 5 MHz transducer produced the best scan quality, although it introduced greater edge distortion. During this investigation, it was found that C-scans could not be perfectly reproduced despite careful duplication of the test procedure. A "control" specimen was included in each scan to act as a scan standard and to facilitate the comparison of C-scan results.

Optical Microscopy: Optical microscopy was a simple technique to use, although it did require extensive sample preparation, including sample mounting and polishing. Optical micrographs were relatively easy to interpret and provided concrete physical evidence that thermally induced changes were occurring in the fiber-matrix interphase. Optical microscopy and electron microprobe analysis proved to be an effective combination of techniques for documenting the physical and chemical changes occurring in the interphase due to thermal ageing.

Electron Microprobe Analysis: The electron microprobe was successfully used to quantitatively determine the chemical composition at specified locations within the composite. Three different man-made crystals were used for X-ray analysis: (1) pseudo-crystal 1 (PC1), (2) lead stearate film (ODPB), and (3) thalium acid phthalate (TAP). The amount (percent atomic weight) and distribution of silicon, oxygen, and carbon within the matrix, interphase, and fibers were determined using this method. The quality of the sample preparation, particularly surface smoothness, and the exactness of the calibration standard (a specimen with known chemical composition) proved to be crucial to the success of the electron microprobe analysis. Two formats were used to display the results: trace scans (1-D scans) and elemental distribution maps (2-D scans).

Tensile Testing and Acoustic Emission Monitoring: Monotonic tensile tests were effectively used to obtain stress-strain curves and to determine ultimate strength and elastic moduli for the heat-treated specimens. During tensile testing, the acoustic emissions from the initiation and propagation of cracks within the matrix and the failure of fibers were monitored. A single (5/26" dia.) resonant sensor, with peak frequencies at 30 kHz and 500 kHz, was used to receive the stress waves and convert them to electrical signals; the total system gain was set at 50 dB and the threshold was set at 40 dB; signal attenuation was increased from 4 ohms to 6 ohms, and then to 7 ohms to prevent system saturation. Acoustic emission events (reported as AE counts) were found to correlate with stress-strain response. Sites of peak acoustic activity corresponded with the stresses and strains associated with matrix and fiber failure.

Future Work

In light of these results and observations, further investigations of Nicalon/SiC composites should concentrate on the chemical and structural changes that occur with thermal ageing. Chemical and structural analyses should be performed in conjunction with nondestructive tests to make the interpretation of NDT results easier and more accurate. In addition to the tests used in this investigation, other analytical methods such as Auger electron spectroscopy and X-ray diffraction may be used to study the chemical composition of the fibers, interphase, and matrix and the structural changes of Nicalon fibers.

A recognized limitation of many composite material investigations is the small number of specimens available for testing. This constraint often makes it impossible to statistically validate results. Future investigations of CMC material should involve a preliminary statistical review so that the number of specimens and tests required to statistically validate results are known prior to

testing. Even if these numbers cannot be satisfied, the investigators would be aware of the limitations of their findings.

Nicalon fibers, like many of the polymer-derived fibers, lose more than half of their RT tensile strength when thermally aged in air at temperatures around 1200° C [8]. This loss of tensile strength is associated with carbon monoxide evolution from the surface of the fibers and to the crystallization of SiC within the fibers. Coating, densifying, or purifying these fibers may improve their high-temperature characteristics by inhibiting or slowing down deleterious chemical reactions. As observed in this investigation, a CVD SiC seal-coat protects and enhances the performance of SiC/SiC composites. Future investigations should address the time and temperature effects which thermal ageing has on refractory coatings. Additional studies should concentrate on the effects that refractory coatings have on NDT results.

REFERENCES

1. "Standardized Testing of Advanced Composites," *Advanced Materials & Processes*, 139[2] 52 (1991).

2. E. D. Hondros and M. Merz, Materials Measurement: A European Perspective; p. 1 in *Harmonisation of Testing Practices for High Temperature Materials*. Elsevier Science Publishing Company, New York, 1992.

3. Robert M. Jones, *Mechanics of Composite Materials*. Hemisphere Publishing Corporation, New York, 1975.

4. David Belitskus, *Fiber and Whisker Reinforced Ceramics for Structural Applications*, Marcel Dekker, New York, 1993.

5. Frances I Hurwitz, "Ceramic Matrix Composites: Ceramic Fiber Reinforced"; p. 297 in *International Encyclopedia of Composites*, Vol. 1. Edited by Stuart M. Lee. VCH Publishers, New York, 1990.

6. Solomon Musikant, *What Every Engineer Should Know About Ceramics*. Marcel Dekker, New York, 1991.

7. L. J. Schioler and J. J. Stiglich, Jr, "Ceramic Matrix Composites: A Literature Review," *American Ceramic Society Bulletin*, 65[2] 289 (1986).

8. K. S. Mazdiyasni, *Fiber Reinforced Ceramic Composites: Materials, Processing, and technology*. Noyes Publications, Park Ridge, New Jersey, 1990.

9. Francis S. Galasso, *Advanced Fibers and Composites*. Gordon and Breach Science Publishers, New York, 1989.

10. William B. Hillig, "Prospects for Ultra-High-Temperature Ceramic Composites"; p. 697 in *Tailoring Multiphase and Composite Ceramics: Proceedings of the 21st University Conference on Ceramic Science* (Pennsylvania State University, University Park, PA, July 17-19, 1985). Edited by Richard E. Tressler, Gary L. Messing, Carlo G. Pantano, and Robert E. Newnham. Plenum Press, New York, 1986.

11. H. Wiedemeier and M. Singh, "Thermal Stability of Refractory Materials for High-Temperature Composite Applications," *Journal of Materials Science*, 26[9] 2421 (1991).

12. Tai-Il Mah, Madan G. Mendiratta, Allan P. Katz, and Khodabakhsh S Mazdiyasni, "Recent Developments in Fiber-Reinforced High Temperature Ceramic Composites", *American Ceramic Society Bulletin,* 66[2] 304 (1987).

13. Terence J. Clark, Richard M. Arons, James B. Stamatoff, and James Rabe, "Thermal Degradation of Nicalon SiC Fibers," *Ceramics Engineering and Science Proceedings*, 6[7-8] 576 (1985).

14. Douglas J. Pysher, Kenneth C. Goretta, Robert S. Hodder, Jr., and Richard E. Tressler, "Strengths of Ceramic Fibers at Elevated Temperatures," *Journal of the American Ceramic Society*, 72[2] 284 (1989).

15. Hyoun-Ee Kim and Arthur J. Moorehead, "Strength of Nicalon Silicon Carbide Fibers Exposed to High-Temperature Gaseous Environments", *Journal of the American Ceramics Society*, 74[3] 666 (1991).

16. M. Huger, S. Souchard, and C. Gault, "Oxidation of Nicalon SiC Fibres," *Journal of Materials Science Letters*, 12[6] 414 (1993).

17. Dileep Singh and Jitendra P Singh, "Effect of High-Temperature Loading on Mechanical Properties of Nicalon Fibers and Nicalon Fiber/SiC Matrix Composites"; p. 1153 in *Ceramic Engineering and Science Proceedings: Proceedings of the 17th Annual Conference on Composites and Advanced Ceramic Materials* (Cocoa Beach, FL, Jan. 10-15, 1993). Edited by John B. Wachtman. The American Ceramic Society, Westerville, OH, 1993.

18. Structural Materials: Materials in Action Series. Edited by George Weidmann and Peter Lewis, and Nick Reid. Butterworth Scientific, Boston, MA, 1990.

19. S. T. Buljan and V. K. Sarin, "Silicon Nitride-Based Composites," *Composites*, 18(2) 99 (1987). (Citing the PhD thesis of K.T. Faber, University of California, Berkeley, 1982).

20. James A. Crawford, Jr., "Weaving"; p. 648 in *International Encyclopedia of Composites*, Vol. 2. Edited by Stuart M. Lee. VCH Publishers, New York, 1990.

21. *Handbook of Composite Reinforcements*. Edited by Stuart M. Lee. VCH Publishers, New York, 1993.

22. Kent W. Buesking, "Effects of Weave Geometry on Properties of Nicalon Reinforced Ceramic Matrix Composites"; p. 705 in *The 17th Conference on Metal Matrix, Carbon, and Ceramic Matrix Composites: Proceedings of a Conference Sponsored by the National Aeronautics and Space Administration*, Part 2 (Cocoa Beach, FL, Jan. 10-15, 1993). Edited by John D. Buckley. NASA Conference Publication 3235.

23. Jonas M. Neumeister, Stefan Jansson, and Frederick A. Leckie, "The Effect of Fiber Architecture on the Mechanical Properities of a Carbon/Carbon Fiber Composite," Santa Barbara, California: Dept. of Mechanical and Environmental Engineering, University of California, 1994. (To be published)

24. J.-M. Yang, W. Lin, C. J. Shih, W. Kai, S. M. Jeng, and C. V. Burkland, "Mechanical Behaviour of Chemical Vapour Infiltration-Processed Two- and Three-Dimensional Nicalon/SiC Composites," *Journal of Materials Science*, 26[11] 2954 (1991).

25. W. J. Lackey, "Ceramic Matrix Composites CVI: Chemical Vapor Infiltration," p. 318 in *International Encyclopedia of Composites*, Vol. 1. Edited by Stuart M. Lee. VCH Publishers, New York, 1990.

26. David P. Stinton, A. J. Caputo, and Richard A. Lowden, "Synthesis of Fiber-Reinforced SiC Composites by Chemical Vapor Infiltration," *American Ceramic Society Bulletin*, 65[2] 347 (1986).

27. Pierre J. Lamicq, Gerald A. Bernhart, Martine M. Dauchier, and Jean G. Mace, "SiC/SiC Composite Ceramics," *American Ceramic Society Bulletin*, 65[2] 336 (1986).

28. G. Gauthier, G. Bessenay, and Y. Honnorat, "CMC Evaluation for Use in Military Aircraft Engines"; p. 970 in *Fourth International Symposium on Ceramic Materials and Components for Engines* (Goteberg, Sweden, June 10-12, 1991). Edited by R. Carlsson, T. Johansson, and L. Kahlman. Elsevier Science Publishing Co., New York, 1991.

29. Alex Vary, "Nondestructive Evaluation: Session Overview"; p. 63 in *Lewis Structures Technology - 1988*, Vol. 3. Proceedings of an exposition and symposium of structures technology developed under the auspices of NASA Lewis Research Center's Structures Division (Cleveland, OH, May 24-25, 1988). NASA, Scientific and Technical Branch, NASA Conference Publication 3003.

30. Alex Vary, "NDE Standards for High Temperature Materials"; in *Symposium on Nondestructive Testing Standards II: New Opportunities for Increased World Trade through Accepted Standards for NDT and Quality* (Gaithersbury, MD, April 9-11, 1991). NASA Technical Memorandum 103761.

31. Laurel M. Sheppard, "Evolution of NDE Continues for Ceramics," *American Ceramic Society Bulletin*, 70[8] 1265 (1991).

32. W. A. Ellingson, R. A. Roberts, J. L. Ackerman, B. D. Sawicka, S. Gronemyer, and R. J. Kriz, "Recent Developments in Nondestructive Evaluation for Structural Ceramics"; p. 267 in *International Advances in Nondestructive Testing*, Vol. 13. Edited by W. J. McGonnagle. Gordon and Breach, New York, 1988.

33. D. B. Marshall, "NDE of Fiber and Whisker-Reinforced Ceramics"; p. 60 in *Progress in Quantitative NDE*. Plenum Press, New York, 1986.

34. J. W. McCauley, "Materials Testing in the 21st Century"; p. 1 in *Conference Proceedings, Nondestructive Testing of High-Performace Ceramics*. Edited by A. Vary and J. Synder. The American Ceramic Society, Westerville, Ohio, 1987.

35. D. Proulx, C. Roy, and D. G. Zimcik, "Assessment of the State of the Art of Non-Destructive Evaluation of Advanced Composite Materials," *Canadian Aeronautics and Space Journal*, 3[4] 325 (1985).

36. Alex Vary, and Stanley J.Klima, "NDE of Ceramics and Ceramic Composites," *NASA Technical Memorandum 104520*. NASA, July (1991).

37. H.-A. Crostack and H.-D. Steffens, "Aspects of Non-Destructive Testing of High Temperature Materials"; p. 217 in *Behavior of Joints in High Temperature Materials: Proceedings of the European Symposium* (Petten (N. H.), The Netherlands). Edited by T. G. Gooch, R. Hurst, H. Kroeckel, and M. Merz. Applied Science Publishers, New York, 1982.

38. Andrew Briggs, *An Introduction to Scanning Acoustic Microscopy: Royal Microscopical Society, Microscopy Handbooks* (12). Oxford University Press, New York, 1985.

39. D. G. P. Fatkin, C. B. Scruby, and G. A. D. Briggs, "Acoustic Microscopy of Low Ductility Materials," *Journal of Material Science*, 24[1] 23 (1989).

40. Abdullah Atalar, "Increasing the Sensitivity of the Scanning Acoustic Microscope to Anistropy"; p. 791 in *IEEE Ultrasonics Symposium*. IEEE, New York, 1987.

41. Abdullah Atalar, "Improvement of Anisotropy Sensitivity in the Scanning Acoustic Microscope," *IEEE Transactions on Ultrasonics, Ferroelectrics, and Frequency Control*, 36[2] 264 (1989).

42. Alex Vary and Stanley J. Klima, "Application of Scanning Acoustic Microscopy to Advanced Structural Materials"; p. 77 in *Characterization of Advanced Materials*. Edited by William Altergott and Edmund Henneke. Plenum Press, New York, 1990.

43. C. W. Lawrence, C. B. Scruby, G. A. D. Briggs, and A. Dunhill, "Crack Detection in Silicon Nitride by Acoustic Microscopy," *NDT International*, 23[1] 3 (1990).

44. Shamachary Sathish, William T. Yost, John H. Cantrell, Edward R. Generazio, Ramakrishna T. Bhatt, and Jeffrey I. Eldridge, "Acoustic Microscopic Characterization of Fiber/Matrix Interface of SiC Fiber Reinforced Reaction Bonded Si_3N_4 Matrix Composites"; p. 599 in *The 17th Conference on Metal Matrix, Carbon, and Ceramic Matrix Composites: Proceedings of a Conference Sponsored by the National Aeronautics and Space Administration*, Part 2 (Cocoa Beach, FL, Jan. 10-15, 1993). Edited by John D. Buckley. NASA Conference Publication 3235.

45. Shamachary Sathish, William T. Yost, John H. Cantrell, Edward R. Generazio, Rebecca A. MacKay, and Karen M. B. Taminger, "Scanning Acoustic Microscopy of SCS-6 SiC Fibers in Titanium Matrices"; p. 643 in *The 17th Conference on Metal Matrix, Carbon, and Ceramic Matrix Composites: Proceedings of a Conference Sponsored by the National Aeronautics and Space Administration*, Part 2 (Cocoa Beach, FL, Jan. 10-15, 1993). Edited by John D. Buckley. NASA Conference Publication 3235.

46. Harold E Kautz, "Nondestructive Evaluation by Acousto-Ultrasonics"; p. 67 in *Lewis Structures Technology - 1988*, Vol. 3. Proceedings of an exposition and symposium of structures technology developed under the auspices of NASA Lewis Research Center's Structures Division (Cleveland, OH, May 24-25, 1988). NASA, Scientific and Technical Branch, NASA Conference Publication 3003.

47. John C Duke, Jr., "Acousto-Ultrasonics"; Chapter 13 in *Nondestructive Testing Techniques*. Edited by Don E. Bray and Don McBride. John Wiley and Sons, New York, 1992.

48. Edmund G. Henneke, II and John C. Duke, Jr, "Analytical Ultrasonics for Evaluation of Composite Materials Response. Part II: Generation and Detection"; p. 153 in *Analytical Ultrasonics in Materials Research and Testing*. Proceedings of a conference sponsored by NASA (Cleveland, OH, Nov. 13-14, 1984). NASA Conference Publication 2383.

49. Mahesh C. Bhardwaj, "Fundamental Developments in Ultrasonics for Advanced NDC"; p. 472 in *Proceedings of the Joint Conference on Nondestructive Testing of High-Performance Ceramics* (Boston, MA, August 25-27, 1987). The American Ceramic Society, Westerville, OH, 1987.

50. Robert E. Green, "Ultrasonic Nondestructive Materials Characterization"; p. 1 in *Analytical Ultrasonics in Materials Research and Testing*. Proceedings of a conference sponsored by NASA (Cleveland, OH, Nov. 13-14, 1984). NASA Conference Publication 2383.

51. Edmund G. Henneke, II and John C. Duke, Jr, "Analytical Ultrasonics for Evaluation of Composite Materials Response. Part I: Physical Interpretation"; p. 141 in *Analytical Ultrasonics in Materials Research and Testing*. Proceedings of a conference sponsored by NASA (Cleveland, OH, Nov. 13-14, 1984). NASA Conference Publication 2383.

52. Stanley J. Klima and George Y. Baaklini, "Ultrasonic Characterization of Structural Ceramics"; p. 117 in *Analytical Ultrasonics in Materials Research and Testing*. Proceedings of a conference sponsored by NASA (Cleveland, OH, Nov. 13-14, 1984). NASA Conference Publication 2383.

53. John H. Hemann and George Y. Baaklini, "Effect of Stress on Ultrasonic Pulses in Fiber Reinforced Composites"; p. 181 in *Analytical Ultrasonics in Materials Research and Testing*. Proceedings of a conference sponsored by NASA (Cleveland, OH, Nov. 13-14, 1984). NASA Conference Publication 2383.

54. *Nondestructive Testing Handbook: Radiography and RadiationTesting*, Vol 3. 2nd ed. Edited by Lawrence E. Bryant and Paul McIntire. American Society for Nondestructive Testing, U. S., 1985.

55. K. E. Amin, T. Derkacs, and S. Matay, "Detectability of Seeded Defects in HIP'ed Si_3N_4 Using Both Ultrasonics and Radiography"; p. 1063 in *Proceedings of the Third International Symposium, Ceramic Materials and Components for Engines* (Las Vegas, Nevada, Nov. 27-30, 1988). The American Ceramics Society, 1989.

56. A. Notea, Y. Tzabari, K. Rudich, and D. G. Brandon, "X-Ray Density Mapping and Materials Characterization for a Ceramic Precombustion Chamber"; p.1085 *Proceedings of the Third International Symposium, Ceramic Materials and Components for Engines* (Las Vegas, Nevada, Nov. 27-30, 1988). The American Ceramics Society, 1989.

57. Russell D. Jamison, "Stereo X-Ray Radiography of Composite Materials"; p. 1 in *Characterization of Advanced Materials*. Edited by William Altergott and Edmund Henneke. Plenum Press, New York, 1990.

58. *Nondestructive Testing Techniques*. Edited by Don E. Bray and Don McBride. John Wiley and Sons, New York, 1992.

59. Wolfgang Sachse and Kwang Yul Kim, "New Developments for the Ultrasonic Characterization of Materials"; p. 73 in *Nondestructive Characterization of Materials*. Proceedings of the 3rd International Symposium (Saarbrucken, FRG, Oct. 3-6, 1988). Edited by P. Holler, V. Hauk, G. Dobmann, C. O. Ruud, and R. E. Green. Springer-Verlag, New York, 1989.

60. J. B. Walter, L. A. Lott, and Paul M. Gammell, "Ultrasonic Characterization of Porosity in Advanced SiC Ceramic Composites"; p. 156 in *Proceedings of the Joint Conference on Nondestructive Testing of High-Performance Ceramics* (Boston, MA, August 25-27, 1987). The American Ceramic Society, Westerville, OH, 1987.

61. Mohamed A. Mahmoud, "Ultrasonic Flaw Detection in Ceramics"; p. 198 in *Proceedings of the Joint Conference on Nondestructive Testing of High-Performance Ceramics* (Boston, MA, August 25-27, 1987). The American Ceramic Society, Westerville, OH, 1987.

62. "Optical methods in composites"; in *Proceedings of the SEM Fall Conference on Experimental Mechanics* (Keystone, CO, Nov. 2-5, 1986).

63. B. A. Bender, D. Lewis, III, W. S. Coblenz, and R. W. Rice, "Electron Microscopy of Ceramic Matrix Composites - Comparison with Processing and Behavior", *Ceramics Engineering and Science Proceedings*, 5[7-8] 513 (1984).

64. Y. Maniette and A. Oberlin, "TEM Characterization of Some Crude or Air Heat-Treated SiC Nicalon Fibres," *Journal of Materials Science*, 24 3361 (1989).

65. Eric Lifshin, "Electron Microprobe Analysis"; p. 115 in *Concise Encyclopedia of Materials Characterization*. Edited by Robert W. Cahn, Frs., Eric Lifshin, and Michael B. Bever. Pergamon Press, New York, 1993.

66. John A. Chandler, "X-Ray Microanalysis in the Electron Microscope"; in *Practical Methods in Electron Microscopy*. Edited by Audrey M.Glauert. North-Holland Publishing Company, New York, 1977.

67. J. I. Goldstein, et al, *Scanning Electron Microscopy and X-Ray Microanalysis: A Text for Biologists, Materials Scientists, and Geologists*. Plenum Press, New York, 1992.

68. K. F. J. Heinrich, *Electron Beam X-Ray Microanalysis*. Van Nostrand Reinhold, New York, 1981.

69. N. Frety and M. Boussuge, "Relationship Between High-Temperature Development of Fibre-Matrix Interfaces and the Mechanical Behaviour of SiC-SiC Composites," *Composites Science and Technology*, 37 177 (1990).

70. Shin Steven Lee, *Damage Analysis and Mechanical Response of As-Received and Heat-Treated Nicalon/CAS-II Glass-Ceramic Matrix Composites*. Blacksburg, Virginia: Virginia Polytechnic Institute and State University; 180 p., Dissertation (1993).

71. *Nondestructive Testing Techniques*. Edited by Don E. Bray and Don McBride. John Wiley and Sons, New York, 1992.

72. M. Arrington, "Acoustic Emission: A Review"; p. 429 in *Non-Destructive Testing: Proceedings of the 12th World Conference on Non-Destructive Testing* (Amsterdam, The Netherlands, April 23-28, 1989). Elsevier Science Publishing Company, New York, 1989.

73. R. Pyrz, "Inelastic Modelling of Acoustic Emission Signature in Composite Materials"; p. 667 in *Developments in the Science and Technology of Composite Materials: Fourth European Conference on Composite Materials* (Stuttgart, F.R.G, Sept. 25-28, 1990). Edited by J. Fuller, G. Gruninger, K. Schulte, A. R. Bunsell, and A. Massiah. Elsevier Science Publishing Company, New York, 1990.

74. J. Block, "Real-Time Inspection of Carbon Fiber Composite Structures Under Thermal and Mechanical Load by Acoustic Emission"; p. 697 in *Developments in the Science and Technology of Composite Materials: Fourth European Conference on Composite Materials* (Stuttgart, F.R.G, Sept. 25-28, 1990). Edited by J. Fuller, G. Gruninger, K. Schulte, A. R. Bunsell, and A. Massiah. Elsevier Science Publishing Company, New York, 1990.

75. J. G. Bakuckas, Jr., W. H. Prosser, and W. S. Johnson, p. 607 in *The 17th Conference on Metal Matrix, Carbon, and Ceramic Matrix Composites*, Part 2. Proceedings of a conference sponsored by the National Aeronautics and Space Administration (1993 Cocoa Beach, FL, Jan. 10-15, 1993). Edited by John D. Buckley. NASA, Langley Research Center. NASA Conference Publication 3235.

76. J. J. Mecholsky, "Evaluation of Mechanical Property Testing Methods for Ceramic Matrix Composites," *American Ceramic Society Bulletin*, 65[2] 315 (1986).

77. Donald F. Baxter, Jr., "Tensile Testing at Extreme Temperatures," *Advanced Materials & Processes*, 139[2] 22 (1991).

78. Hugo Ferguson, "Physical Simulation Makes Inroads in Advanced Materials Testing," *Advanced Materials & Processes*, 143[4] 33 (1993).

79. Martin L Bartlett, Cheryl R.Blanchard, David L. Davidson, and Andrew Nagy, "Testing Advanced Materials at High Temperatures," *Advanced Materials & Processes*, 142[5] 18 (1992).

80. P. Pluvinage, L. Filipuzzi, L., and G. Camus, "Mechanical Behavior and Oxidation Resistance of a Unidirectional SiC/SiC Fibrous Composite"; p. 937 in *Ceramic Transactions. Advanced Composite Materials: Processing, Microstructures, Bulk and Interfacial Properties, Characterization Methods, and Applications*, Vol. 19. Edited by Michael D Sacks. The American Ceramic Society, Westerville, Ohio, 1991.

81. *McGraw-Hill Concise Encyclopedia of Science & Technology*, 2nd. ed. Edited by Sybil P. Parker. McGraw-Hill Publishing Co., New York, 1989.

82. Paul P. Grosskopf, *Mechanical Behavior of a Ceramic Matrix Composite Material.* Blacksburg, Virginia: Virginia Polytechnic Institute and State University; 142 p., Thesis (1990).

83. Edward R. Generazio, "Ultrasonic Verification of Microstructural Changes Due to Heat Treatment"; p. 207 in *Analytical Ultrasonics in Materials Research and Testing*. Proceedings of a conference sponsored by NASA (Cleveland, OH, Nov. 13-14, 1984). NASA Conference Publication 2383.

APPENDIX A

ASTM Standards

Advanced Ceramics

C 1145 (15.01) Standard Terminology of Advanced Ceramics
C 1161 (15.01) Standard Test Method for Flexural Strength of Advanced Ceramics at Ambient Temperature
C 1175 (15.01) Standard Guide to Test Methods and Standards for Nondestructive Testing of Advanced Ceramics
C 1198 (15.01) Standard Test Method for Dynamic Young's Modulus, Shear Modulus, and Poisson's Ratio for Advanced Ceramics by Sonic Resonance
C 1211 (15.01) Standard Test Method for Flexural Strength of Advanced Ceramics at Elevated Temperatures
C 1212 (15.01) Standard Practice for Fabricating Ceramic Reference Specimens Containing Seeded Voids
C 1239 (15.01) Standard Practice for Reporting Uniaxial Strength Data and Estimating Weibull Distribution Parameters for Advanced Ceramics
E 1435 (11.03) Standard Practice for Handling Densified Articles of Aluminum Oxide Reinforced with Silicon Carbide Whiskers
E 1436 (11.03) Standard Practice for Handling Densified Articles of Silicon Nitride Reinforced with Silicon Carbide Whiskers
E 1437 (11.03) Standard Practice for Handling Silicon Carbide Whiskers

Tension (Tensile) Properties/Tests

C 565 (15.01) Carbon/Graphite Mechanical Materials (with Grain Size < 0.79 mm (1/32 in.))

Tension (Tensile) Properties/Tests - Aerospace Materials

C 297 (15.03) Tensile Strength of Flat Sandwich Constructions in Flatwise Plane
D 2585 (15.03) Preparation/Tension Testing of Filament-Wound Pressure Vessels
D 3379 (15.03) Tensile Strength/Young's Modulus for High-Modulus Single-Filament Materials
D 3544 (15.03) Reporting Test Methods/Results on High Modulus Fibers
D 4018 (15.03) Tensile Properties - Continuous Filament Carbon/Graphite Fiber Tows
F 521 (15.03) Transparent Laminates - Bond Integrity

Tension (Tensile)Properties/Tests - Composites

D 3039 (15.03) Tensile Properties - Resin Matrix Composites
D 3479 (15.03) Tension-Tension Fatigue of Oriented Fiber Resin Matrix Composites
D 3552 (15.03) Tensile Properites of Fiber-Reinforced Metal Matrix Composites
D 4762 (15.03) Automotive/Industrial Composite Materials - Selection of Test Methods
E 1434 (15.03) High-Modulus Fiber-Reinforced Composite Materials - Development of Standard Data Records for Computerization of Mechanical Test Data

Nondestructive Testing

Volume 3.03

APPENDIX B

I. Resolution of Scanning Acoustic Microscope

The theoretical resolution of a scanning acoustic microscope as defined by G. S. Kino* is

$$w = 0.51\lambda/\text{N.A.}$$

where w is the separation for resolving, λ is the wavelength of the acoustic signal in the coupling fluid, and N.A. is the numerical aperture of the lens. Since true numerical apertures do not exist outside of theory, the above equation provides only a good approximation of the resolution. However, the above relationship does suggest ways for improving the resolution. According to the equation the resolution of an acoustic microscope is proportional to the wavelength. Since the wavelength and frequency are related according to

$$\lambda = v/f$$

where v is the velocity of sound in the fluid, and f is the frequency of the acoustic waves in the fluid, the resolution is also inversely proportional to the frequency. Thus, the resolution may be improved by making the wavelength smaller or by increasing the frequency.

II. Trial Investigations

- Speed of sound in Nicalon/SiC composite, $v \approx 8310$ m/s
  (Estimate based on pulse-echo and through-transmission measurements made using 5 MHz liquid-couplant transducers, pulser, and oscilloscope; Nicalon/SiC specimen tested was 0.131 inches thick.)

- Speed of sound in water (at 298 °K), $v = 1495$ m/s

30 MHz lens $\Rightarrow$ Wavelength of acoustic waves in water, 49.83 μm
50 MHz lens $\Rightarrow$ Wavelength of acoustic waves in water, 29.90 μm
100 MHz lens $\Rightarrow$ Wavelength of acoustic waves in water, 14.95 μm

* Kino, Gordon S. Acoustic waves: devices, imaging and analog signal processing. Englewood Cliffs, New Jersey: Prentice Hall; 1987.

III. Lens Used in this Investigation

$2a_o$, lens aperture diameter
q, focal length
θ_o, semi-angle subtended at the focus by the circumference of the lens aperture

50 MHz lens: $2a_o$= 0.25 in. = 6.35 mm
q_o (according to Olympus) = 12 mm
q_p (according to Panametrics) = 0.5 in. = 12.7 mm
$2\theta_o = 28°$

- Refractive index for acoustic waves passing from sapphire to water, n = 0.134

- Speed of sound in water (at 298 °K), v = 1495 m/s
- Speed (longitudinal) of sound in sapphire (c-axis), v_l = 11,150 m/s
- Ratio of wave velocities, n = 1495/11,150

Resolution Approximation

Numerical aperture, N.A.:
N.A. = $\sin\theta_o = a_o/q$

N.A. = sin(28/2) = 0.242
N.A. = a_o/q_o = (6.35/2)/12 = 0.265
N.A. = a_o/q_p = (6.35/2)/12.7 = 0.250
N.A., nominal = (0.242 + 0.265 + 0.250)/3 = 0.252

$\lambda = v/f$ = (1495 m/s)/(50 x 10^6 s^{-1}) = 29.9 μm

$w = 0.51\lambda/\text{N.A.}$ = (0.51)(29.9 μm)/0.252 = 60.5 μm (for surface features)

Note: The separation for resolving sub-surface features in a material will be larger than the value obtained above. To determine the sub-surface resolution, the wavelength (λ) of acoustic waves in the material must be known. Since the speed of acoustic waves is much larger in a solid material than in water for the same frequency, the corresponding wavelength will also be larger and, in turn, the separation for resolving will be greater.

APPENDIX C

AU Results
Area Under Power Spectral Density Curve (M0)
Trial measurements from reference specimen AM-7-2, position 3

TRIAL MEASUREMENTS (1)

M0			
2.9769E+06	1.20E+10	High(1)	3.1110E+06
2.9241E+06	3.22E+09	Low(1)	2.4822E+06
2.9048E+06	1.40E+09	Avg(1)	2.8674E+06
3.1110E+06	5.93E+10	Std. Dev.	8.1187E+04
2.9223E+06	3.01E+09	Variance	6.5914E+09
2.7324E+06	1.82E+10		
2.7626E+06	1.10E+10		
2.9159E+06	2.35E+09		
2.9419E+06	5.55E+09		
2.4822E+06	1.48E+11		

TRIAL MEASUREMENTS (2)

M0			
4.1889E+05	1.99E+07	High(2)	4.4463E+05
4.2959E+05	2.30E+08	Low(2)	3.6990E+05
4.2497E+05	1.11E+08	Avg(2)	4.1443E+05
4.4463E+05	9.12E+08	Std. Dev.	1.0066E+04
4.1397E+05	2.08E+05	Variance	1.0131E+08
4.2630E+05	1.41E+08		
4.0325E+05	1.25E+08		
4.2703E+05	1.59E+08		
3.8577E+05	8.21E+08		
3.6990E+05	1.98E+09		

TRIAL MEASUREMENTS (3)

M0			
2.3831E+05	3.44E+08	High(3)	2.9857E+05
2.3913E+05	3.14E+08	Low(3)	2.3088E+05
2.4942E+05	5.54E+07	Avg(3)	2.5686E+05
2.4936E+05	5.64E+07	Std. Dev	2.5023E+03
2.3088E+05	6.75E+08	Variance	6.2613E+06
2.8218E+05	6.41E+08		
2.9857E+05	1.74E+09		
2.6345E+05	4.34E+07		
2.6007E+05	1.03E+07		
2.5726E+05	1.55E+05		

TRIAL MEASUREMENTS (4) - 6/6/94

M0			
2.9928E+05	1.72E+07	High(4)	3.2103E+05
2.8878E+05	4.04E+07	Low(4)	2.7078E+05
2.7712E+05	3.24E+08	Avg(4)	2.9513E+05
2.9593E+05	6.44E+05	Std. Dev	2.6750E+02
2.9309E+05	4.16E+06	Variance	7.1556E+04
2.7078E+05	5.93E+08		
3.2103E+05	6.71E+08		
2.9319E+05	3.74E+06		
3.1050E+05	2.36E+08		
3.0159E+05	4.17E+07		

AM-7-3

POSITION	1	2	3	4	5
T-R	7.3925E+04	4.5004E+05	6.1061E+05	4.1386E+05	4.9522E+05
R-T	2.3653E+05	4.3358E+05	7.1702E+05	4.9995E+05	5.6355E+05
T-R	1.6619E+05	4.6888E+05	6.3628E+05	5.0625E+05	6.5571E+05
R-T	1.9814E+05	5.9215E+05	9.2341E+05	5.8619E+05	5.5508E+05
Avg. T-R	1.2006E+05	4.5946E+05	6.2345E+05	4.6006E+05	5.7546E+05
Avg. R-T	2.1733E+05	5.1286E+05	8.2021E+05	5.4307E+05	5.5931E+05

AM-7-4

POSITION	1	2	3	4	5
T-R	5.0502E+05	6.5460E+05	6.2052E+05	8.6380E+05	3.7593E+05
R-T	1.5111E+05	5.6413E+05	4.6451E+05	7.7904E+05	3.2513E+05
T-R	1.7343E+05	5.0188E+05	4.2654E+05	7.7252E+05	2.9777E+05
R-T	1.2387E+05	4.2393E+05	3.5868E+05	7.2423E+05	3.5835E+05
Avg. T-R	3.3922E+05	5.7824E+05	5.2353E+05	8.1816E+05	3.3685E+05
Avg. R-T	1.3749E+05	4.9403E+05	4.1160E+05	7.5163E+05	3.4174E+05

AM-7-5

POSITION	1	2	3	4	5
T-R	4.9307E+05	5.3124E+05	4.7341E+05	5.7343E+05	1.9979E+05
R-T	3.3539E+05	4.4733E+05	4.2245E+05	5.2383E+05	1.9631E+05
T-R	2.2365E+05	3.6407E+05	2.9825E+05	4.6493E+05	2.1724E+05
R-T	3.0930E+05	4.6220E+05	3.5152E+05	4.5174E+05	2.5230E+05
Avg. T-R	3.5836E+05	4.4765E+05	3.8583E+05	5.1918E+05	2.0852E+05
Avg. R-T	3.2234E+05	4.5477E+05	3.8698E+05	4.8778E+05	2.2431E+05

TRIAL MEASUREMENTS (5) - 6/8/94

M0			
4.5351E+05	1.05E+09	High(5)	6.0192E+05
4.3503E+05	2.60E+09	Low(5)	4.3072E+05
4.4524E+05	1.66E+09	Avg(5)	4.8597E+05
5.2518E+05	1.54E+09	Std. Dev	1.3068E+04
4.4844E+05	1.41E+09	Variance	1.7077E+08
5.1893E+05	1.09E+09		
4.3072E+05	3.05E+09		
4.3298E+05	2.81E+09		
5.6776E+05	6.69E+09		
6.0192E+05	1.34E+10		

AM-1-5

POSITION	1	2	3	4	5
T-R	5.1552E+05	5.8858E+05	4.6665E+05	7.7838E+05	3.7584E+05
R-T	3.3358E+05	4.9601E+05	3.9291E+05	6.2046E+05	4.7755E+05
T-R	3.3075E+05	4.8528E+05	3.8794E+05	7.6370E+05	4.2182E+05
R-T	3.6481E+05	5.2404E+05	4.8053E+05	9.1486E+05	3.8074E+05
Avg. T-R	4.2313E+05	5.3693E+05	4.2729E+05	7.7104E+05	3.9883E+05
Avg. R-T	3.4919E+05	5.1003E+05	4.3672E+05	7.6766E+05	4.2915E+05

AM-7-6

POSITION	1	2	3	4	5
T-R	3.9823E+05	5.3347E+05	5.7672E+05	5.1647E+05	2.3074E+05
R-T	2.5430E+05	3.4402E+05	4.3781E+05	2.9584E+05	1.6769E+05
T-R	1.3990E+05	3.0687E+05	3.2831E+05	3.2837E+05	1.2956E+05
R-T	1.6876E+05	3.2008E+05	3.6420E+05	4.8306E+05	2.0124E+05
Avg. T-R	2.6906E+05	4.2017E+05	4.5251E+05	4.2242E+05	1.8015E+05
Avg. R-T	2.1153E+05	3.3205E+05	4.0101E+05	3.8945E+05	1.8446E+05

TRIAL MEASUREMENTS (6) - 6/9/94

M0			
2.7671E+05	2.62E+09	High(6)	2.7671E+05
1.9284E+05	1.07E+09	Low(6)	1.6944E+05
2.5612E+05	9.39E+08	Avg(6)	2.2548E+05
2.3765E+05	1.48E+08	Std. Dev	4.0573E+03
2.4195E+05	2.71E+08	Variance	1.6462E+07
2.4283E+05	3.01E+08		
2.4195E+05	2.71E+08		
2.1156E+05	1.94E+08		
1.8376E+05	1.74E+09		
1.6944E+05	3.14E+09		

AM-1-6

POSITION	1	2	3	4	5
T-R	3.0477E+05	5.5394E+05	5.0136E+05	5.0498E+05	4.9654E+05
R-T	2.9687E+05	6.2234E+05	4.5378E+05	5.4703E+05	5.8290E+05
T-R	2.4794E+05	3.9706E+05	3.0202E+05	3.4264E+05	3.4467E+05
R-T	2.6659E+05	5.8266E+05	4.1881E+05	4.4666E+05	5.8941E+05
Avg. T-R	2.7635E+05	4.7550E+05	4.0169E+05	4.2381E+05	4.2061E+05
Avg. R-T	2.8173E+05	6.0250E+05	4.3629E+05	4.9684E+05	5.8615E+05

TRIAL MEASUREMENTS (7) - 6/10/94

M0			
3.5268E+05	2.84E+09	High(7)	4.4190E+05
3.5046E+05	3.08E+09	Low(7)	3.5046E+05
4.4190E+05	1.29E+09	Avg(7)	4.0595E+05
4.1056E+05	2.13E+07	Std. Dev	1.5370E+03
3.9983E+05	3.75E+07	Variance	2.3625E+06
4.2771E+05	4.73E+08		
4.3224E+05	6.91E+08		
4.2593E+05	3.99E+08		
4.2518E+05	3.70E+08		
3.9300E+05	1.68E+08		

AM-1-7

POSITION	1	2	3	4	5
T-R	4.1328E+05	6.5979E+05	6.7644E+05	4.3621E+05	2.6850E+05
R-T	1.8555E+05	4.1166E+05	4.3461E+05	3.7879E+05	3.7411E+05
T-R	1.8236E+05	4.7017E+05	4.6233E+05	3.5999E+05	5.1193E+05
R-T	1.6106E+05	4.9904E+05	6.4702E+05	2.9953E+05	4.2810E+05
Avg. T-R	2.9782E+05	5.6498E+05	5.6938E+05	3.9810E+05	3.9021E+05
Avg. R-T	1.7331E+05	4.5535E+05	5.4082E+05	3.3916E+05	4.0111E+05

AM-2-1

POSITION	1	2	3	4	5
T-R	5.5931E+05	5.8501E+05	9.0050E+05	9.8986E+05	5.0999E+05
R-T	3.3264E+05	3.6706E+05	6.9685E+05	9.6484E+05	6.4843E+05
T-R	3.3507E+05	3.1629E+05	5.2695E+05	6.2300E+05	4.8832E+05
R-T	3.4798E+05	3.9572E+05	5.5634E+05	7.1040E+05	4.4084E+05
Avg. T-R	4.4719E+05	4.5065E+05	7.1373E+05	8.0643E+05	4.9915E+05
Avg. R-T	3.4031E+05	3.8139E+05	6.2659E+05	8.3762E+05	5.4464E+05

TRIAL MEASUREMENTS (8) - 6/13/94

M0			
1.5023E+06	1.66E+09	High(8)	1.7174E+06
1.4126E+06	2.40E+09	Low(8)	1.1312E+06
1.7144E+06	6.40E+10	Avg(8)	1.4615E+06
1.4503E+06	1.27E+08	Std. Dev	3.7517E+03
1.7174E+06	6.55E+10	Variance	1.4075E+07
1.4023E+06	3.51E+09		
1.5811E+06	1.43E+10		
1.3027E+06	2.52E+10		
1.4009E+06	3.67E+09		
1.1312E+06	1.09E+11		

AM-8-1

POSITION	1	2	3	4	5
	2.3196E+05	1.5820E+04	1.8563E+05	3.2059E+05	5.5694E+05
	1.8076E+05	2.2490E+04	2.3273E+05	3.2500E+05	4.4980E+05
	2.0636E+05	1.9155E+04	2.0918E+05	3.2279E+05	5.0337E+05
Average	2.0636E+05	1.9155E+04	2.0918E+05	3.2279E+05	5.0337E+05

POSITION	6	7	8	9	10
	6.3558E+05	1.1306E+05	9.8435E+04	9.0631E+04	1.9247E+05
	7.8312E+05	9.4994E+04	8.1593E+04	5.9048E+04	1.8810E+05
	7.0935E+05	1.0403E+05	9.0014E+04	7.4840E+04	1.9028E+05
Average	7.0935E+05	1.0403E+05	9.0014E+04	7.4840E+04	1.9028E+05

POSITION	11	12	13	14	15
	6.6615E+04	1.8971E+04	1.3158E+05	9.6385E+04	9.1953E+04
	6.4922E+04	2.0799E+04	1.5147E+05	9.2854E+04	8.4786E+04
	6.5768E+04	1.9885E+04	1.4152E+05	9.4619E+04	8.8369E+04
Average	6.5768E+04	1.9885E+04	1.4152E+05	9.4619E+04	8.8369E+04

POSITION	16
	9.7643E+04
	1.0747E+05
	1.0256E+05
Average	1.0256E+05

TRIAL MEASUREMENTS (9) - 9/28/94

M0			
1.6360E+06	5.51E+06	High(9)	1.7174E+06
1.6260E+06	5.89E+07	Low(9)	1.1312E+06
1.6288E+06	2.36E+07	Avg(9)	1.6336E+06
1.6718E+06	1.46E+09	Std. Dev	1.2739E+04
1.9588E+06	1.06E+11	Variance	1.6228E+08
1.3044E+06	1.08E+11		
1.3705E+06	6.92E+10		
1.3912E+06	5.87E+10		
1.9494E+06	9.97E+10		
1.7993E+06	2.75E+10		

HEAT TREATED AM-7-4

POSITION	1	2	3	4	5
T-R	2.8556E+05	3.9995E+05	8.8763E+05	1.0204E+06	9.4598E+05
R-T	2.4166E+05	4.7425E+05	1.1489E+06	1.2042E+06	1.0356E+06
T-R	2.1945E+05	3.9091E+05	9.8620E+05	1.1099E+06	6.7580E+05
R-T	2.2339E+05	4.4589E+05	1.0984E+06	1.0706E+06	8.4718E+05
Avg. T-R	2.5250E+05	3.9543E+05	9.3692E+05	1.0652E+06	8.1089E+05
Avg. R-T	2.3252E+05	4.6007E+05	1.1236E+06	1.1374E+06	9.4138E+05

TRIAL MEASUREMENTS (10) - 10/05/94

MO			
4.3165E+06	5.47E+10	High(10)	1.7174E+06
4.1678E+06	7.27E+09	Low(10)	1.1312E+06
3.8135E+06	7.24E+10	Avg(10)	4.0826E+06
3.4496E+06	4.01E+11	Std. Dev	2.1097E+05
3.9702E+06	1.26E+10	Variance	4.4509E+10
4.3265E+06	5.95E+10		
4.2991E+06	4.69E+10		
4.3476E+06	7.02E+10		
4.4885E+06	1.65E+11		
3.6462E+06	1.90E+11		

HEAT TREATED AM-7-3

POSITION	1	2	3	4	5
T-R	1.5953E+06	2.6875E+06	2.6956E+06	2.5446E+06	3.0879E+06
R-T	1.6502E+06	2.3218E+06	2.9726E+06	2.9618E+06	4.5872E+06
T-R	1.4414E+06	2.2914E+06	2.3204E+06	2.3261E+06	4.6368E+06
R-T	1.5515E+06	2.0924E+06	2.1446E+06	2.3397E+06	3.2565E+06
Avg. T-R	1.5184E+06	2.4895E+06	2.5080E+06	2.4354E+06	3.8624E+06
Avg. R-T	1.6009E+06	2.2071E+06	2.5586E+06	2.6507E+06	3.9218E+06

HEAT TREATED AM-7-5

POSITION	1	2	3	4	5
T-R	2.6121E+06	4.1765E+06	2.9808E+06	5.6101E+06	4.7121E+06
R-T	3.6893E+06	4.6869E+06	2.6720E+06	4.7204E+06	6.1467E+06
T-R	3.3008E+06	4.6461E+06	2.4816E+06	5.2160E+06	5.9487E+06
R-T	3.0658E+06	5.0149E+06	2.9388E+06	6.6151E+06	4.8490E+06
Avg. T-R	2.9564E+06	4.4113E+06	2.7312E+06	5.4130E+06	5.3304E+06
Avg. R-T	3.3776E+06	4.8509E+06	2.8054E+06	5.6677E+06	5.4978E+06

HEAT TREATED AM-7-6

POSITION	1	2	3	4	5
T-R	4.9666E+06	1.1465E+07	5.3576E+06	5.3115E+06	4.0086E+06
R-T	8.6953E+06	1.3746E+07	5.0315E+06	6.2260E+06	3.5210E+06
T-R	6.2776E+06	1.2699E+07	5.5761E+06	5.1166E+06	4.6996E+06
R-T	7.1203E+06	1.3056E+07	4.5464E+06	5.7528E+06	3.8041E+06
Avg. T-R	5.6221E+06	1.2082E+07	5.4669E+06	5.2141E+06	4.3541E+06
Avg. R-T	7.9078E+06	1.3401E+07	4.7890E+06	5.9894E+06	3.6625E+06

HEAT TREATED AM-1-5

POSITION	1	2	3	4	5
T-R	6.8939E+05	1.5901E+06	2.6782E+06	7.9710E+06	1.8464E+06
R-T	6.5544E+05	1.5965E+06	3.4600E+06	8.3243E+06	2.0307E+06
T-R	5.7777E+05	1.0212E+06	2.5699E+06	8.4735E+06	2.2407E+06
R-T	6.3781E+05	1.2632E+06	2.9542E+06	8.7032E+06	1.9064E+06
Avg. T-R	6.3358E+05	1.3057E+06	2.6240E+06	8.2223E+06	2.0435E+06
Avg. R-T	6.4662E+05	1.4299E+06	3.2071E+06	8.5138E+06	1.9685E+06

TRIAL MEASUREMENTS (11) - 10/17/94

M0			
3.4161E+06	1.49E+10	High(11)	1.7174E+06
3.3302E+06	1.30E+09	Low(11)	1.1312E+06
3.0508E+06	5.92E+10	Avg(11)	3.2942E+06
3.3046E+06	1.10E+08	Std. Dev	3.4890E+03
3.4649E+06	2.91E+10	Variance	1.2173E+07
3.4781E+06	3.38E+10		
3.2287E+06	4.28E+09		
3.2783E+06	2.50E+08		
3.2104E+06	7.02E+09		
3.1795E+06	1.32E+10		

HEAT TREATED AM-1-6

POSITION	1	2	3	4	5
T-R	1.7632E+06	3.3287E+06	1.2265E+06	1.0002E+06	1.9430E+06
R-T	1.2713E+06	3.8352E+06	1.2311E+06	1.1834E+06	1.4163E+06
T-R	1.0651E+06	2.9809E+06	1.2841E+06	1.2006E+06	1.2277E+06
R-T	8.5810E+05	2.2034E+06	1.1459E+06	1.1389E+06	7.0101E+05
Avg. T-R	1.4141E+06	3.1548E+06	1.2553E+06	1.1004E+06	1.5853E+06
Avg. R-T	1.0647E+06	3.0193E+06	1.1885E+06	1.1611E+06	1.0586E+06

HEAT TREATED AM-1-7

POSITION	1	2	3	4	5
T-R	2.5384E+06	1.0065E+07	5.9937E+06	1.0353E+07	1.5439E+06
R-T	2.4429E+06	7.7589E+06	6.1118E+06	1.1018E+07	1.4900E+06
T-R	2.2061E+06	9.2968E+06	5.8653E+06	9.0580E+06	1.7920E+06
R-T	2.3813E+06	8.0085E+06	5.2362E+06	9.6435E+06	1.8086E+06
Avg. T-R	2.3722E+06	9.6808E+06	5.9295E+06	9.7056E+06	1.6679E+06
Avg. R-T	2.4121E+06	7.8837E+06	5.6740E+06	1.0331E+07	1.6493E+06

HEAT TREATED AM-2-1

POSITION	1	2	3	4	5
T-R	1.9168E+06	3.5005E+06	8.3739E+06	7.5695E+06	2.2543E+06
R-T	1.9146E+06	3.5625E+06	8.4789E+06	7.3390E+06	2.4343E+06
T-R	1.8891E+06	3.1742E+06	8.1923E+06	6.7541E+06	2.6832E+06
R-T	1.8858E+06	3.4816E+06	9.1174E+06	7.4664E+06	2.2700E+06
Avg. T-R	1.9030E+06	3.3373E+06	8.2831E+06	7.1618E+06	2.4688E+06
Avg. R-T	1.9002E+06	3.5220E+06	8.7981E+06	7.4027E+06	2.3521E+06

TRIAL MEASUREMENTS (12) - 10/18/94

M0			
4.1025E+06	6.67E+10	High(12)	1.7174E+06
4.1218E+06	7.71E+10	Low(12)	1.1312E+06
3.7860E+06	3.38E+09	Avg(12)	3.8441E+06
3.9081E+06	4.10E+09	Std. Dev	2.1339E+04
3.7159E+06	1.64E+10	Variance	4.5535E+08
3.6871E+06	2.46E+10		
3.9284E+06	7.11E+09		
3.7428E+06	1.03E+10		
3.7336E+06	1.22E+10		
3.7150E+06	1.67E+10		

HEAT TREATED AM-8-1

POSITION	1	2	3	4	5
	8.0620E+05	1.0348E+05	1.5648E+06	1.0039E+06	2.8910E+06
	6.2239E+05	1.3803E+05	2.0108E+06	1.0260E+06	2.7201E+06
	7.1429E+05	1.2075E+05	1.7878E+06	1.0149E+06	2.8055E+06
Average	7.1429E+05	1.2075E+05	1.7878E+06	1.0149E+06	2.8055E+06

POSITION	6	7	8	9	10
	3.1614E+06	3.6496E+05	5.6338E+05	7.1870E+05	5.4986E+05
	2.2917E+06	4.8727E+05	5.9996E+05	7.7875E+05	6.9438E+05
	2.7266E+06	4.2612E+05	5.8167E+05	7.4873E+05	6.2212E+05
Average	2.7266E+06	4.2612E+05	5.8167E+05	7.4873E+05	6.2212E+05

POSITION	11	12	13	14	15
	3.2403E+05	8.6954E+04	6.1266E+05	9.5812E+05	5.7998E+05
	2.8629E+05	1.1638E+05	8.5190E+05	1.2162E+06	6.9958E+05
	3.0516E+05	1.0167E+05	7.3228E+05	1.0871E+06	6.3978E+05
Average	3.0516E+05	1.0167E+05	7.3228E+05	1.0871E+06	6.3978E+05

POSITION	16
	5.1813E+05
	4.4040E+05
	4.7927E+05
Average	4.7927E+05

Paired T-Test for Specimens Heat Treated at 1000 C: AM-1-7, AM-2-1, and AM-8-1

Number of pairs, n = 36
5% significance level
Hypothesized difference between normalized means = 0

The following averages (from AM-7-2, position 3) are used to normalize data:
Avg(7): 4.06E+05
Avg(8): 1.46E+06
Avg(11): 3.29E+06
Avg(12): 1.63E+06

Specimen	As-Fab.	Norm.(A)	Heat Tr.	Norm.(B)	A-B	di-d	(di-d)^2
AM-1-7	1.73E+05	-2.33E+05	2.41E+06	-8.82E+05	6.49E+05	1.93E+06	3.72E+12
	4.55E+05	4.94E+04	7.88E+06	4.59E+06	-4.54E+06	-3.26E+06	1.06E+13
	5.41E+05	1.35E+05	5.67E+06	2.38E+06	-2.24E+06	-9.65E+05	9.31E+11
	3.39E+05	-6.68E+04	1.03E+07	7.04E+06	-7.10E+06	-5.82E+06	3.39E+13
	4.01E+05	-4.84E+03	1.65E+06	-1.64E+06	1.64E+06	2.92E+06	8.53E+12
	2.98E+05	-1.08E+05	2.37E+06	-9.22E+05	8.14E+05	2.09E+06	4.39E+12
	5.65E+05	1.59E+05	9.68E+06	6.39E+06	-6.23E+06	-4.95E+06	2.45E+13
	5.69E+05	1.63E+05	5.93E+06	2.64E+06	-2.47E+06	-1.19E+06	1.42E+12
	3.98E+05	-7.85E+03	9.71E+06	6.41E+06	-6.42E+06	-5.14E+06	2.64E+13
	3.90E+05	-1.57E+04	1.67E+06	-1.63E+06	1.61E+06	2.89E+06	8.36E+12
AM-2-1	3.40E+05	-6.56E+04	1.90E+06	-1.39E+06	1.33E+06	2.61E+06	6.80E+12
	3.81E+05	-2.46E+04	3.52E+06	2.28E+05	-2.52E+05	1.03E+06	1.06E+12
	6.27E+05	2.21E+05	8.80E+06	5.50E+06	-5.28E+06	-4.00E+06	1.60E+13
	8.38E+05	4.32E+05	7.40E+06	4.11E+06	-3.68E+06	-2.40E+06	5.74E+12
	5.45E+05	1.39E+05	2.35E+06	-9.42E+05	1.08E+06	2.36E+06	5.57E+12
	4.47E+05	4.12E+04	1.90E+06	-1.39E+06	1.43E+06	2.71E+06	7.36E+12
	4.51E+05	4.47E+04	3.34E+06	4.32E+04	1.55E+03	1.28E+06	1.64E+12
	7.14E+05	3.08E+05	8.28E+06	4.99E+06	-4.68E+06	-3.40E+06	1.16E+13
	8.06E+05	4.00E+05	7.16E+06	3.87E+06	-3.47E+06	-2.19E+06	4.78E+12
	4.99E+05	9.32E+04	2.47E+06	-8.25E+05	9.19E+05	2.20E+06	4.84E+12
AM-8-1	2.06E+05	-1.26E+06	7.14E+05	-9.19E+05	-3.36E+05	9.44E+05	8.92E+11
	1.92E+04	-1.44E+06	1.21E+05	-1.51E+06	7.05E+04	1.35E+06	1.82E+12
	2.09E+05	-1.25E+06	1.79E+06	1.54E+05	-1.41E+06	-1.26E+05	1.59E+10
	3.23E+05	-1.14E+06	1.01E+06	-6.19E+05	-5.20E+05	7.60E+05	5.78E+11
	5.03E+05	-9.58E+05	2.81E+06	1.17E+06	-2.13E+06	-8.50E+05	7.22E+11
	7.09E+05	-7.52E+05	2.73E+06	1.09E+06	-1.85E+06	-5.65E+05	3.19E+11
	1.04E+05	-1.36E+06	4.26E+05	-1.21E+06	-1.50E+05	1.13E+06	1.28E+12
	9.00E+04	-1.37E+06	5.82E+05	-1.05E+06	-3.20E+05	9.61E+05	9.23E+11
	7.48E+04	-1.39E+06	7.49E+05	-8.85E+05	-5.02E+05	7.79E+05	6.06E+11
	1.90E+05	-1.27E+06	6.22E+05	-1.01E+06	-2.60E+05	1.02E+06	1.04E+12
	6.58E+04	-1.40E+06	3.05E+05	-1.33E+06	-6.73E+04	1.21E+06	1.47E+12
	1.99E+04	-1.44E+06	1.02E+05	-1.53E+06	9.03E+04	1.37E+06	1.88E+12
	1.42E+05	-1.32E+06	7.32E+05	-9.01E+05	-4.19E+05	8.62E+05	7.42E+11
	9.46E+04	-1.37E+06	1.09E+06	-5.46E+05	-8.20E+05	4.60E+05	2.11E+11
	8.84E+04	-1.37E+06	6.40E+05	-9.94E+05	-3.79E+05	9.01E+05	8.12E+11
	1.03E+05	-1.36E+06	4.79E+05	-1.15E+06	-2.05E+05	1.08E+06	1.16E+12
					-1.28E+06		2.41E+06
							4.01E+05
							8.15E+05

Mean difference: -1.28E+06
Critical values : +/- 8.15E+05
As-fabricated and heat treated specimens do not have the same sample means.

Paired T-Test for Specimens Heat Treated at 1200 C: AM-7-3, AM-7-4, and AM-1-6

Number of pairs, n = 30
5% significance level
Hypothesized difference between normalized means = 0

The following averages (from AM-7-2, position 3) are used to normalize data:

Avg(4):	2.95E+05
Avg(6):	2.25E+05
Avg(10):	4.08E+06
Avg(9):	1.63E+06
Avg(11):	3.29E+06

Specimen	As-Fab.	Norm.(A)	Heat Tr.	Norm.(B)	A-B	di-d	(di-d)^2
AM-7-3	1.20E+05	-1.75E+05	1.52E+06	-2.56E+06	2.39E+06	8.27E+05	6.84E+11
	4.59E+05	1.64E+05	2.49E+06	-1.59E+06	1.76E+06	1.95E+05	3.82E+10
	6.23E+05	3.28E+05	2.51E+06	-1.57E+06	1.90E+06	3.41E+05	1.16E+11
	4.60E+05	1.65E+05	2.44E+06	-1.65E+06	1.81E+06	2.50E+05	6.26E+10
	5.75E+05	2.80E+05	3.86E+06	-2.20E+05	5.01E+05	-1.06E+06	1.13E+12
	2.17E+05	-7.78E+04	1.60E+06	-2.48E+06	2.40E+06	8.42E+05	7.09E+11
	5.13E+05	2.18E+05	2.21E+06	-1.88E+06	2.09E+06	5.31E+05	2.82E+11
	8.20E+05	5.25E+05	2.56E+06	-1.52E+06	2.05E+06	4.87E+05	2.37E+11
	5.43E+05	2.48E+05	2.65E+06	-1.43E+06	1.68E+06	1.18E+05	1.39E+10
	5.59E+05	2.64E+05	3.92E+06	-1.61E+05	4.25E+05	-1.14E+06	1.29E+12
AM-7-4	3.39E+05	4.41E+04	2.53E+05	-1.38E+06	1.43E+06	-1.37E+05	1.87E+10
	5.78E+05	2.83E+05	3.95E+05	-1.24E+06	1.52E+06	-4.07E+04	1.66E+09
	5.24E+05	2.28E+05	9.37E+05	-6.97E+05	9.25E+05	-6.37E+05	4.06E+11
	8.18E+05	5.23E+05	1.07E+06	-5.68E+05	1.09E+06	-4.71E+05	2.21E+11
	3.37E+05	4.17E+04	8.11E+05	-8.23E+05	8.64E+05	-6.98E+05	4.87E+11
	1.37E+05	-1.58E+05	2.33E+05	-1.40E+06	1.24E+06	-3.19E+05	1.01E+11
	4.94E+05	1.99E+05	4.60E+05	-1.17E+06	1.37E+06	-1.90E+05	3.59E+10
	4.12E+05	1.16E+05	1.12E+06	-5.10E+05	6.26E+05	-9.36E+05	8.75E+11
	7.52E+05	4.57E+05	1.14E+06	-4.96E+05	9.53E+05	-6.09E+05	3.71E+11
	3.42E+05	4.66E+04	9.41E+05	-6.92E+05	7.39E+05	-8.23E+05	6.78E+11
AM-1-6	2.76E+05	5.09E+04	1.41E+06	-1.88E+06	1.93E+06	3.69E+05	1.36E+11
	4.75E+05	2.50E+05	3.15E+06	-1.39E+05	3.89E+05	-1.17E+06	1.38E+12
	4.02E+05	1.76E+05	1.26E+06	-2.04E+06	2.22E+06	6.53E+05	4.26E+11
	4.24E+05	1.98E+05	1.10E+06	-2.19E+06	2.39E+06	8.30E+05	6.89E+11
	4.21E+05	1.95E+05	1.59E+06	-1.71E+06	1.90E+06	3.42E+05	1.17E+11
	2.82E+05	5.62E+04	1.06E+06	-2.23E+06	2.29E+06	7.24E+05	5.24E+11
	6.03E+05	3.77E+05	3.02E+06	-2.75E+05	6.52E+05	-9.10E+05	8.28E+11
	4.36E+05	2.11E+05	1.19E+06	-2.11E+06	2.32E+06	7.54E+05	5.69E+11
	4.97E+05	2.71E+05	1.16E+06	-2.13E+06	2.40E+06	8.42E+05	7.10E+11
	5.86E+05	3.61E+05	1.06E+06	-2.24E+06	2.60E+06	1.03E+06	1.07E+12
					1.56E+06		7.00E+05
							1.28E+05
							2.61E+05

Mean difference:	1.56E+06
Critical values : +/-	2.61E+05

As-fabricated and heat treated specimens do not have the same sample means.

Paired T-Test for Specimens Heat Treated at 1400 C: AM-7-5, AM-7-6, and AM-1-5

Number of pairs, n = 30
5% significance level
Hypothesized difference between normalized means = 0

The following averages (from AM-7-2, position 3) are used to normalize data:
Avg(4): 2.95E+05
Avg(5): 4.86E+05
Avg(10): 4.08E+06

Specimen	As-Fab.	Norm.(A)	Heat Tr.	Norm.(B)	A-B (di)	di-d	(di-d)^2
AM-7-5	3.22E+05	2.72E+04	3.38E+06	-7.05E+05	7.32E+05	1.41E+06	1.98E+12
	4.55E+05	1.60E+05	4.85E+06	7.68E+05	-6.09E+05	6.50E+04	4.23E+09
	3.87E+05	9.19E+04	2.81E+06	-1.28E+06	1.37E+06	2.04E+06	4.17E+12
	4.88E+05	1.93E+05	5.67E+06	1.59E+06	-1.39E+06	-7.19E+05	5.17E+11
	2.24E+05	-7.08E+04	5.50E+06	1.42E+06	-1.49E+06	-8.12E+05	6.60E+11
	3.58E+05	6.32E+04	2.96E+06	-1.13E+06	1.19E+06	1.86E+06	3.47E+12
	4.48E+05	1.53E+05	4.41E+06	3.29E+05	-1.76E+05	4.98E+05	2.48E+11
	3.86E+05	9.07E+04	2.73E+06	-1.35E+06	1.44E+06	2.12E+06	4.48E+12
	5.19E+05	2.24E+05	5.41E+06	1.33E+06	-1.11E+06	-4.33E+05	1.87E+11
	2.09E+05	-8.66E+04	5.33E+06	1.25E+06	-1.33E+06	-6.61E+05	4.37E+11
Am-7-6	2.12E+05	-2.74E+05	7.91E+06	3.83E+06	-4.10E+06	-3.43E+06	1.17E+13
	3.32E+05	-1.54E+05	1.34E+07	9.32E+06	-9.47E+06	-8.80E+06	7.74E+13
	4.01E+05	-8.50E+04	4.79E+06	7.06E+05	-7.91E+05	-1.18E+05	1.38E+10
	3.89E+05	-9.65E+04	5.99E+06	1.91E+06	-2.00E+06	-1.33E+06	1.77E+12
	1.84E+05	-3.02E+05	3.66E+06	-4.20E+05	1.19E+05	7.92E+05	6.28E+11
	2.69E+05	-2.17E+05	5.62E+06	1.54E+06	-1.76E+06	-1.08E+06	1.17E+12
	4.20E+05	-6.58E+04	1.21E+07	8.00E+06	-8.07E+06	-7.39E+06	5.46E+13
	4.53E+05	-3.35E+04	5.47E+06	1.38E+06	-1.42E+06	-7.44E+05	5.54E+11
	4.22E+05	-6.36E+04	5.21E+06	1.13E+06	-1.20E+06	-5.21E+05	2.72E+11
	1.80E+05	-3.06E+05	4.35E+06	2.72E+05	-5.77E+05	9.63E+04	9.28E+09
AM-1-5	3.49E+05	-1.37E+05	6.47E+05	-3.44E+06	3.30E+06	3.97E+06	1.58E+13
	5.10E+05	2.41E+04	1.43E+06	-2.65E+06	2.68E+06	3.35E+06	1.12E+13
	4.37E+05	-4.93E+04	3.21E+06	-8.75E+05	8.26E+05	1.50E+06	2.25E+12
	7.68E+05	2.82E+05	8.51E+06	4.43E+06	-4.15E+06	-3.48E+06	1.21E+13
	4.29E+05	-5.68E+04	1.97E+06	-2.11E+06	2.06E+06	2.73E+06	7.46E+12
	4.23E+05	-6.28E+04	6.34E+05	-3.45E+06	3.39E+06	4.06E+06	1.65E+13
	5.37E+05	5.10E+04	1.31E+06	-2.78E+06	2.83E+06	3.50E+06	1.23E+13
	4.27E+05	-5.87E+04	2.62E+06	-1.46E+06	1.40E+06	2.07E+06	4.30E+12
	7.71E+05	2.85E+05	8.22E+06	4.14E+06	-3.85E+06	-3.18E+06	1.01E+13
	3.99E+05	-8.71E+04	2.04E+06	-2.04E+06	1.95E+06	2.63E+06	6.89E+12
					-6.74E+05		3.01E+06
							5.50E+05
							1.12E+06

Mean difference (d): -6.74E+05
Critical values: +/- 1.12E+06
As-fabricated and heat treated specimens have the same sample means.

APPENDIX D

Polishing SiC/SiC CMC's for Electron Microprobe Analysis and Optical Microscopy

Sample Preparation:

(1) Use warm water and dishwashing detergent to degrease sample
(2) Rinse sample thoroughly with distilled water
(3) Rinse sample with acetone
(4) Rinse sample with isopropyl alcohol
(5) Dry sample in furnace at ≈ 300 °F or in dehydrator

To avoid contaminating samples after they have been cleaned, handle samples with surgical gloves or tweezers.

Mounting Sample:

(1) Use aluminum ring-forms (0.75-1.25" diameter) and 2-part epoxy
(2) Spread release agent on clean glass surface and inside Al ring-form
(3) Lay ring-form on glass surface and place sample inside ring-form (plastic anchors may be used to position sample)
(4) Stir epoxy hardener and resin mixture slowly to minimize introducing bubbles into epoxy
(5) Pour epoxy into ring-form, covering sample; reposition sample if necessary
(6) Allow epoxy to cure

Polishing Procedure:

(1) Remove epoxy-mounted sample from ring-form
(2) Set the velocity of the polishing wheel at ≈ 80 RPM.
    When polishing, contrarotate the sample with respect to the SiC paper.
    Use the following grits of SiC paper in the order given - a small stream of water should be directed onto the paper to cool the sample during polishing, and flush debris from the abrasive surface:
    A. 180 grit
    B. 240 grit
    C. 320 grit
    D. 400 grit
    E. 600 grit
(3) Set the velocity of the polishing wheel at ≈ 120 RPM.
    When polishing, contrarotate the sample with respect to the cloth.
    Ultrasonically clean the sample between different grades of paste.
    Use the following grits of diamond paste, in the order given, on separate TEXMET cloths - spray the diamond paste with paste extender for every new application of paste:
    A. 6 μm diamond paste
    B. 3 μm diamond paste
    C. 1 μm diamond paste

(4) Clean polished sample in ultrasonic cleaner (≤ 10 min.)
(5) Rinse with distilled water and isopropyl alcohol

Reference:

Chanat, Stephanie. FRCMCs, A Sample Preparation Challenge. American Ceramic Society Bulletin. 1994; 73(4): 73-77.

VITA

The author was born on October 25, 1966 in Lexington, Virginia. She was raised in Lexington and Charlottesville, Virginia. In 1985, she graduated from Lexington High School and entered the School of Engineering and Applied Science at the University of Virginia (UVA). She received her Bachelor of Science Degree in Mechanical Engineering in June of 1989 from UVA and in July of the same year began work at AMP Incorporated in Winston-Salem, North Carolina. Three years later, in 1992, she was granted an educational leave-of-absence so that she could pursue a Master of Science Degree in Engineering Science and Mechanics from the Virginia Polytechnic Institute and State University. Upon completion of this degree, Dawn will seek employment in the South Eastern United States and pursue graduate studies part-time.